Macroscopic Tissue Growth, Expansion, and Collision: Biophysical Insights Toward Tissue Sheet Engineering Strategies

Matthew A. Heinrich

A Dissertation
Presented to the Faculty
of Princeton University
in Candidacy for the Degree
of Doctor of Philosophy

Recommended for Acceptance by
the Department of
Mechanical and Aerospace Engineering

Advisers: Daniel J. Cohen and Andrej Košmrlj

September 2021

Abstract

As an organism develops and maintains homeostasis, many thousands of cells must act in concert within and between tissues. How these collective cellular behaviors are coordinated has been a question of interest for over a century, with importance to developmental, regenerative, and pathological processes.

In the last decade, in vitro studies of tissues have brought breakthroughs showing how forces, stresses, traveling waves, and other physical processes provide a basis for biological processes within a tissue like cell migration and proliferation. However, these studies most commonly involve much smaller length scales and shorter time scales than the physiological processes they represent. Additionally, biophysical studies of epithelial tissues rarely examine the interactions between tissues that occur when these systems come into contact. Together, we lack knowledge on how epithelial tissues coordinate biophysical processes across larger length scales, over longer timescales, and during higher-level interactions.

We address this first by studying millimeter-scale tissue expansion at high resolution over several days. We find that the tissue edge starkly decouples from the tissue bulk, producing size and memory effects in patterns of cell migration and proliferation. We also find the first example of millimeter-scale coordinated vortices in unconfined cohesive tissue and explore this process with an active polar fluid model. We finally investigate how cell migration, cell density, and cell proliferation all evolve concomitantly.

We then probe higher-level tissue-tissue interactions by studying the collisions between expanding tissues. We find that these tissues change shape as they collide, which we predict according to the dynamics of single tissue expansion. We then find that genetically identical tissues displace one another due to cell density gradients at their collision boundaries and use the dynamics of this process to extract mechanical properties from the colliding tissues. Finally, we harness the dynamics of

tissue expansion and collision to design arrays that self-assemble into centimeter-scale tessellations.

Overall, we find that macroscale epithelial tissues support large and long-lasting coordinated behaviors, which we harness to engineer tissue as a living material.

Acknowledgments

Thank you to Frank Fisher and Manu Mannoor, who together asked me, "Why not do your PhD, then?"

Thank you to Andrej Košmrlj, who academically adopted me midway through a tumultuous first year. I would not have made it out of that year (let alone the rest) without your patient mentorship and instruction. Your breadth and depth of knowledge across biology and physics will always astound me, but your compassion for the confused student (surely not me) combined with your ability to make the complex accessible seem to be some of your greatest strengths.

Thank you to Andrej's group, especially Mo, Siddhartha, Sijie, and Sheng who journeyed with me to physics conferences and always enjoyed arguing about where to go for dinner. Sheng, I'm so glad we had that chat during my second year when you encouraged me to consider doing my own experiments and adding Daniel Cohen as a co-adviser.

Thank you to Daniel Cohen, who came to Princeton not a moment too soon. Your relentless energy and science storytelling pizzazz make you an inspirational PI, but the way you care for your students is what makes you a great one. I'm so proud to have been in the lab that worked relentlessly on COVID projects, and I will never forget the months of meetings with you and the hospital as we tried to figure out how to fend off the apocalypse with PPE.

Thank you to the Cohen lab super old guard of Julie and Tom, who made me a better person. Tom, your wise proverb of "Our data will still be there, but the opportunity to help may not," has impacted how I think about priorities, and Julie, your consistent concern for the vulnerable and invisible challenged my comfortable worldview.

Gawoon, Gawoon.

Thank you to Sam Otto, without whom I would not have survived the gauntlet of MAE first-year math courses.

Thank you to Ricard Alert, who was more than generous with his time as my tutor before general exams and as an incredible collaborator thereafter. It was always a joy to bounce ideas off of you and stand corrected. We will yet battle it out in table tennis.

Speaking of tennis, thank you to Steve Wu, Jon Labella, and Chris Rosensteel, who journeyed to the Princeton courts to play countless groundstroke games when I couldn't look at my computer screen a minute longer.

Thanks to Chris, Thomas, Dan, Tom, Bolton, Avi, and Tosin who were faithful friends through the ups and the downs. You guys made my time in Princeton some of the best years of my life.

Thanks to my parents-in-law, Chuck and Darlene. Your home was always a safe haven for me to recover from sickness, move past a failure, type up sections of my dissertation, and even get married.

Thanks to my parents and sister Lauren, who were always ready for a visit or a call. You guys loved me so well through the setbacks and celebrated so well after the victories. You were the family I needed and more.

Thanks to my loving wife, my "spark." The first few Princeton years were hard, but God was faithful. Our married year here was a gift we will treasure forever.

This dissertation carries T#3416 in the records of the Department of Mechanical and Aerospace Engineering.

To my wife, the strongest and sweetest person I know.

Do not despise these small beginnings, for the LORD rejoices to see the work begin.

Zechariah 4:10

Contents

List of Figures

Chapter 1

Introduction

1.1 Introductory remarks from the author

As an engineer of mechanics and materials, I could not help but marvel when I encountered epithelial tissue for the first time. Thanks to the coordinated behavior of its constituent cells, this "living material"[1] can flow like fluid under its own forcing [2], undergo extreme stretch [3], actively change its mechanical properties [4], and sense and self-heal imperfections [5], just to name a few of its more astounding abilities. As we explore the coordination of tens of thousands of cells within evolving tissues, I hope the reader gains in understanding of and wonder for this rich, biological system.

1.2 Historical background

Marie François Xavier Bichat, considered by many to be the father of histology, first introduced the idea of a biological tissue at the turn of the nineteenth century, describing twenty-one different tissue types as "disparate" and more general and fundamental in structure and function than organs [6]. In modern physiology, twenty-one has been paired down to four, with epithelial tissues containing more than 60%

of the cells in the human body [7]. Epithelial tissues perform crucial functions as an organism develops and maintains homeostasis, covering organs to mechanically and chemically separate the inner workings of organisms from the outside world [8]. This makes them critical for all facets of life because, as Bichat said[1], "Such is the mode of existence of living bodies that everything surrounding them tends to destroy them" [11].

With the introduction of cell theory in 1839, it was realized that Bichat's tissues were actually collections of even more fundamental units [12]. Rudolf Virchow[2] brought to the fore the importance of the actions of these cells on tissue–and organism[3]–function, describing tissues as "a society of cells, a tiny well-ordered state... in which every cell is a citizen" [13].

Our work here has deep roots in Virchow's social framework, as well as Abercrombie's writings on cellular behavior from the 1950's [15, 16] that descibe how interactions between cells can regulate tissue function. Indeed, cell-cell interactions give rise to behaviors such as contact inhibition [15, 17, 18], collective cell migration [5, 19], and cell-cycle regulation [20–23], which underlie physiological functions such as tissue development and healing [24, 25], organ size control [26, 27], morphogenetic patterning [28], and even pathological processes such as tumor invasion [29, 30].

Cell-cell interactions are often studied with in vitro tissues that reduce the number of cell-cell interactions[4]; reduce the dimensionality of cell migration [5, 22, 32–34]; operate at timescales below which proliferation is important [35]; inhibit proliferation altogether [36]; or prevent natural size and shape changes that unconfined tissues

[1]While this declaration by Bichat was motivated by his adoption of the popular vitalist fallacies of the time [9], its message rings true when one considers the heroic battle biology must wage against entropy [10].

[2]Rudolf Virchow, declaring "Omnis cellula e cellula" (all cells come from cells) [13], corrected the original cell theory that hypothesized in a biological analogy to nucleation of crystals that cells formed via spontaneous generation [12].

[3]Virchow is considered the father of cellular pathology thanks to his foundational work in elucidating the cellular basis for several diseases [14].

[4]In the extreme, "tissues" of pairs of cells are isolated to study the relationship between cell-cell forces and cell forces with the surroundings [31]

undergo [37–40]. While these studies have been crucial in describing individual contributions to tissue behavior such as traction forces, migratory dynamics, and cell divisions, they lack the integrated approach of capturing whole-tissue dynamics that the social framework demands.

Moreover, while cell-cell interactions have been intensely investigated, less is known about tissue-tissue interactions. This is partly because "wound-healing" studies primarily focus on the initial outward migration [5] and do not include the collision and fusion that occurs when free edges meet [41], so opportunity lies in understanding more about these tissue collision events. Combining understanding about the expansion of tissues with these tissue collision dynamics additionally should allow us to build tissue sheets by allowing smaller sheets to expand and fuse.

1.3 Scope of this work and author contributions

In this dissertation, we address these opportunities by studying millimeter-scale tissues of tens of thousands of cells as they naturally expand, which, when cultured on the same substrate, leads to their collision and eventual fusion.

In Chapter 2, we cover important background and literature. We first summarize relevant subcellular structures that manifest cell and tissue behavior. We then discuss important mechanical properties of epithelial tissues and the environment in which they exist. We conclude with recent advances from the literature that shed light on the coordination of collective cell migration and proliferation and provide the backdrop for our studies here.

In Chapter 3, we investigate macro-scale, single-tissue expansion with the aim of studying large-scale coordination of cell migration and proliferation. To this end, we study the unconstrained expansion of whole monolayer tissues of varied size and shape, at length scales and timescales relevant to multiday development and regen-

eration processes. We find that, while expanding with an edge speed independent of initial conditions, millimeter-scale epithelial monolayers exhibit internal patterns of proliferation and migration that depend not on the current but on the initial tissue size, indicating memory effects. Specifically, the core of large tissues becomes very dense, almost quiescent, and ceases cell-cycle progression. In contrast, initially-smaller tissues develop a local minimum of cell density and a tissue-spanning vortex. To explain vortex formation, we propose an active polar fluid model with a feedback between cell polarization and tissue flow. Our findings here suggest that expanding epithelia decouple their internal and edge regions, which enables robust expansion dynamics despite the presence of size- and history-dependent patterns in the tissue interior. This work was adapted from work [23] published with coauthors Ricard Alert, Julienne LaChance, Tom Zajdel, Andrej Košmrlj, and Daniel J. Cohen. Ricard Alert was the primary contributor of the polar fluid model and associated analyses. Julienne LaChance contributed to experiments and data analysis, and Tom Zajdel contributed to data analysis. This author was the primary contributor to modeling[5], experiments, and analyses as lead author.

In Chapter 4, we investigate tissue-tissue interactions. We ask, what do the dynamics of tissue collisions tell us about the properties of the tissues that collide, and can we design tissue arrays that self-assemble into larger composite tissues with predefined patterns? To answer these questions, we studied tissue collisions resulting from the outgrowth of monolayer tissues with different geometries, cell densities, and cell types. We determine rules for tissue shape changes during binary collisions and describe complex cell migration at tri-tissue boundaries. Next, we demonstrate that genetically identical tissues displace each other based solely on cell density gradients, which vanish when density gradients equalize. We then present a physical model of tissue interactions that allows us to estimate the bulk modulus of the tis-

[5]excepting the polar fluid model

sues from these collision dynamics. Finally, we introduce TissEllate, a design tool for self-assembling complex tessellations from arrays of many tissues, and we use cell sheet engineering techniques to transfer these composite tissues like cellular films. This work provides insight into the mechanics of tissue collisions, harnessing them to engineer tissue composites as designable living materials. This work was submitted as a manuscript for publication [42] along with coauthors Ricard Alert, Abraham E. Wolf, Andrej Košmrlj, and Daniel J. Cohen. Ricard Alert contributed the physical modeling of tissue flows due to cell density gradients, and Avi Wolf contributed to co-culture experiments. Additionally, Jake Strain and Sofie Gonzalez assisted with experimental setup for several experiments. This author was the primary contributor for all other modeling, experiments, and analyses as lead author.

In Chapter 5, we review the significant findings contained in this dissertation and point to additional opportunities and promising avenues raised by this work.

Lastly, in Appendix A, we briefly describe efforts to supplement local health centers with personal protective equipment (PPE) components for powered air respirators (PAPRs). We present a design for a reusable face shield component of PAPR suits that replaces a disposable part that is often in short supply when needed most. These devices were worn by dozens of medical workers with the most severe exposure to the SARS-CoV-2 virus, with no reported COVID-19 infections. With a team of volunteers and efficient organizational structure, we built and assembled over 1,000 components, allowing a large regional medical center to continue to use all of their available PAPRs. Our approaches give insights for organizational strategies and rapid design processes that may become necessary during a crisis. This author developed initial prototypes with input from Daniel J. Cohen, as well as developing the organizational strategy and leading the PAPR face shield design and production efforts.

Chapter 2

Background

Before diving into the sweeping, coordinated actions of hundreds of thousands of cells that will be the focus of Chapters 3 and 4, we will briefly introduce a few of the molecular players and multicellular processes that make this possible.

2.1 Subcellular structures and functions

Ultimately, the collective effects discussed later rely on the structure of subcellular units inside and outside of the cell. This section will only provide a brief summary for which additional information can be found in the major text for this field [7].

2.1.1 The cytoskeleton

The mechanics of cells and tissues are intimately linked with the actions and structure of the cytoskeleton, an intricate network of protein filaments and tubules that provide the cell with mechanical integrity and the capability of exerting forces on its surroundings.

First, filamentous actin (F-actin) is the critical fiber the cell uses to push or pull on its surroundings. F-actin fibers have a relatively low bending stiffness (persistence

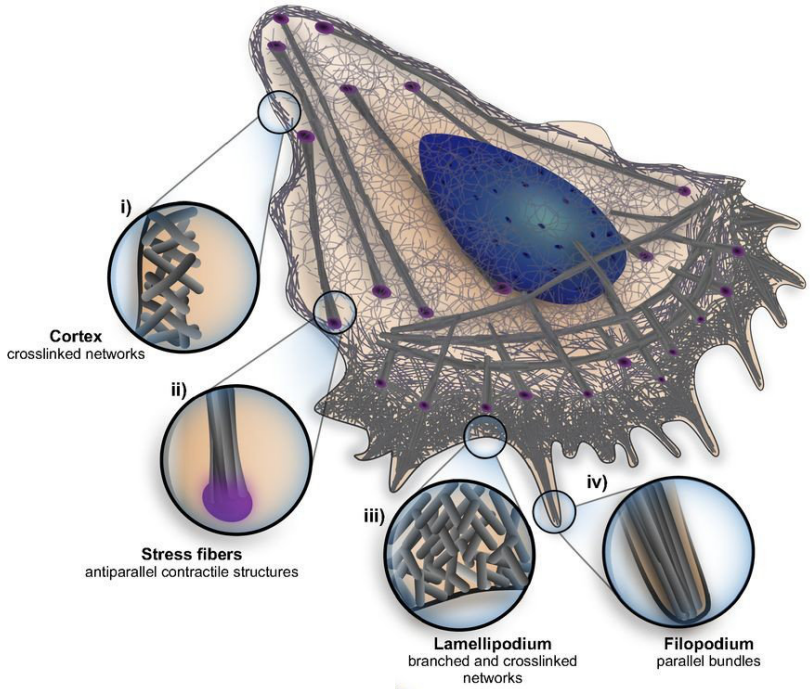

Figure 2.1: Actin structures. Crosslinked F-actin forms the contractile cortex (i); oppositely-oriented F-actin forms contractile stress fibers (ii); branched crosslinked actin form extensile lamellipodia (iii); and parallel bundles form protruding filopodia (iv). Adapted from [43] with permission from The American Physiological Society.

length $\sim 15\mu$m, a little less than the length of most epithelial cells), but they become stiffer once crosslinked into bundles, branches, or isotropic networks that perform varied functions within the cell [44] (see Fig. 2.1). F-actin has front-rear polarity and can exert an extensile force by assembly of globular actin (G-actin) on the front end of the filament(Fig. 2.2a). This extension is evident when branched F-actin causes a cell-scale, fan-like protrusion to emerge from the front of a cell; this lamellipodium is the hallmark of a polarized migrating cell [45], and cells in a tissue also extend these fan-like structures as "cryptic lamellipodia" under adjacent cells [46]. On the other hand, F-actin can "pull" with the help of the molecular motor myosin, forming a complex aptly referred to as a "stress fiber" [47]. An individual myosin motor "walks" in only one direction on the polarized F-actin filament; many myosin motors can then come together to form myosin filaments that simultaneously walk on nearby F-actin

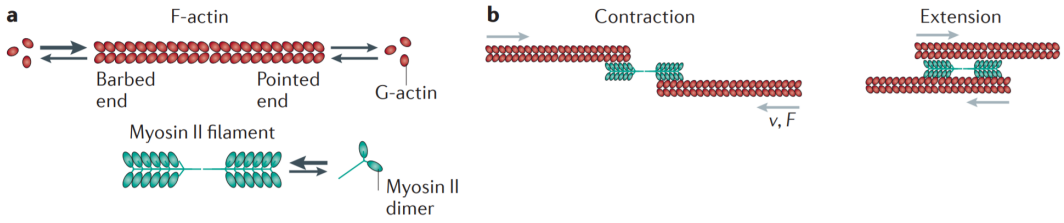

Figure 2.2: Actomyosin in action. (a) Myosin II dimers bundle to form Myosin filaments, and G-actin assembles into F-actin filaments. Myosin filaments on oppositely oriented F-actin filaments can produce contraction (b) or extension (c) depending on the relative location of the Myosin filaments and F-actin. Adapted by permission from Springer Nature Customer Service Centre GmbH: Springer Nature, Nature Reviews Molecular Cell Biology [48], Copyright 2015.

fibers. If these F-actin fibers are oriented oppositely, this walking will then produce either extension or contraction by pulling the fibers in opposite directions(Fig. 2.2b,c). Since F-actin can withstand higher tension than compression (where it buckles at low loads), the actomyosin network produces net contraction [48]. Such a contractile actomyosin network lines the interior of the epithelial cell membrane, giving cells active surface tension; stress fibers, on the other hand, span across the cell, enable it to contract.

Next, rope-like filaments called intermediate filaments provide the cell with tensile strength. Intermediate filaments are extremely bendable fibers (persistence length $\sim$0.5 μm [44]) that do not support directional movement of molecular motors, but their tensile strength makes them crucial to the mechanical integrity of cells and tissues. Extreme stretching can threaten the integrity of the cell; when this strain becomes large enough that the intermediate filaments straighten, the filaments themselves stretch and produce a restoring force that halts the dangerous deformation [3]. The importance of intermediate filaments becomes evident when considering the blistering of the skin or other disease symptoms that arise in epithelial tissue when intermediate filament function is hindered [49].

Finally, microtubules are hollow, tubular structures important for organizing internal components of the cell. Microtubules are the least bendable cytoskeletal structure (persistence length > 5mm[1]) [44], which gives them the ability to resist compressive loads [51]. While the functions of microtubules are essential to processes underlying cell migration [52] and cell division [53], they do not play as direct a physical role in the mechanics and migration of tissues as do actin and intermediate filaments. Readers interested in learning more about the cytoskeleton are directed to the appropriate texts [7] and reviews [44].

2.1.2 Cell-cell junctions

Cells adhere to one another through the binding of adhesive proteins on their surfaces. These proteins come from the cadherin superfamily, and the type of cadherin present at a cell-cell-junction can determine the properties of the cell-cell interaction [54]. Cadherins cross the cell membrane, forming complexes that bind to F-actin (at adherens junctions, see Fig. 2.3) and intermediate filaments (at desmosomes) within the cell. Adherens junctions allow the cell to transmit forces across many cells [55], while desmosomes provide structural integrity [56] and maintain the cell network connectivity [57]. In particular, E-cadherin is crucial in maintaining a cohesive cell sheet and avoiding pathological outcomes [54].

While cells exert forces on other cells via cell-cell junctions, they also sense forces through the complex of proteins that connect the cytoplasmic domain (interior part) of E-cadherin to contractile cytoskeleton [58]. When a cell-cell junction is put under tension, the protein α-catenin unfolds, which promotes the binding of the protein vinculin to the F-actin-E-cadherin complex [58]. This binding of vinculin then promotes accumulation of more E-cadherin to this particular binding site, increasing its adhesion and cohesiveness [59]. This recruitment of vinculin (and therefore E-cadherin)

[1]This generally-accepted very long persistence length can vary based on microtubule length and lateral forcing [50].

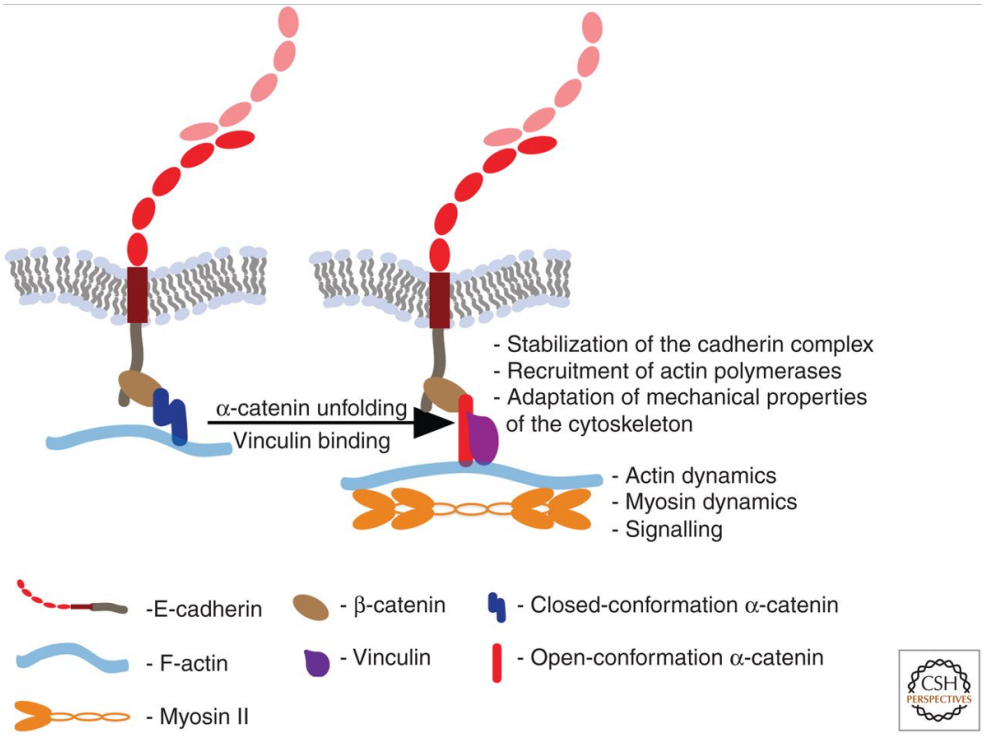

Figure 2.3: Cell-cell junctions link the cytoskeleton of adjacent cells.The intracellular portion of E-cadherin links with the cytoskeleton at complexes crucial for force transmission and mechanosensing [58]. This mechanosensing relies on the unfolding of α-catenin, which recruits Vinculin to the complex [58]; binding of Vinculin then recruits more E-cadherin to the adherins junction [59]. Reproduced from [58] with permission. Copyright 2018 Cold Spring Harbor Laboratory Press.

enables force transmission across many cells and alters collective cell migration [60], which will take center stage in Chapters 3 and 4.

2.1.3 Extracellular matrix and cell-ECM adhesions

Extracellular matrix (ECM) provides the scaffolding on and through which cells migrate and live. ECM, which is made and modified by cells, is composed of various proteins and molecules that assemble into fibrils or sheets [4]. Collagen is the most abundant ECM protein, and is found in 28 known types [4]. Type I collagen is the most abundant, forming fibrils, while type IV collagen forms a 2D sheet and composes most of the basement membrane on which epithelial tissues adhere [61]. As such we

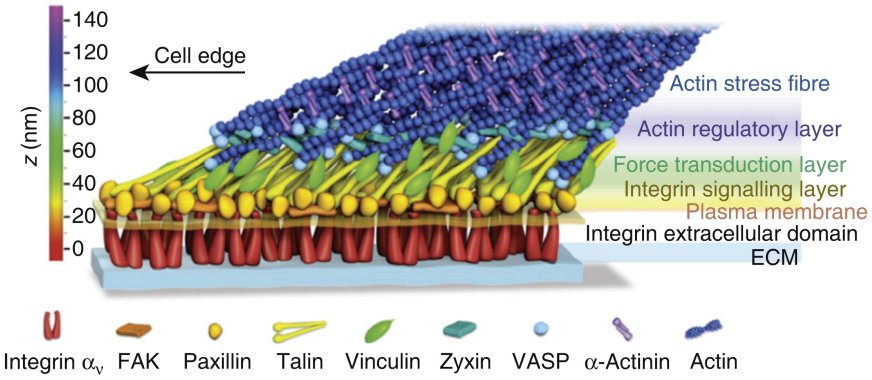

Figure 2.4: Cells anchor to their surroundings via focal adhesions. While the emphasis of focal adhesions is often the extracellular portion that adheres to ECM, we see here that a focal adhesion contains a highly structured intracellular portion containing many molecules. Reproduced from [62], Copyright 2011, with permission from Elsevier.

use petri dishes with type IV collagen adsorbed on their surface for the studies on epithelial tissues reported here.

Cells anchor to their environment through focal adhesions, which are large receptor complexes that adhere to the ECM (see Fig. 2.4). The adhesive protein in focal adhesions belongs to the integrin family, with different types of integrins binding to different sites (ligands) on different ECM proteins [7]. Similarly to adherens junctions, focal adhesions cross the cell membrane to connect with F-actin, allowing the cell to exert forces on the ECM [7].

2.1.4 Subcellular structures and functions act in concert

For an example of how some of the subcellular units in the previous subsections may act in concert during the life of a cell, let us take single cell migration. While the coordinated processes underlying cell migration are all occuring simultaneously and being adjusted to compensate for changing environments, the following stepwise sequence is instructive. First, branched actin protrudes the front of the cell membrane forward, which forms new focal adhesions as it prepares to use these new sites as anchoring points. Then, focal adhesions and actin must disassemble at the rear of

the cell [63] so that active contraction of actomysosin stress fibers can pull the cell body forward. Finally, new focal adhesions form in the new location, and the sequence can start again.

2.2 Multicellular structures and functions

When epithelial cells come together at adherens junctions and bind to a basement membrane of ECM, they form epithelial tissue. In the body, epithelial tissues exist as surfaces that line the outside of organs and other structures, separating the internal processes of tissues and organisms from the outside world [7]. As such, they must be cohesive, flexible, and able to close gaps or wounds.

How epithelial tissues coordinate cell proliferation and migration has been a question of interest for well over a century [64, 65] and is critical to development, regeneration, and cancer. Indeed, almost every animal was once a continuous epithelial sheet as an embryo, which then proceeded to undergo large, directed motions and cell divisions to plan and build the body [66]. Epithelial sheets are crucial in healing wounds as well, where the tissue must sense a gap in the tissue, migrate into it, and fill in missing cells via cell divisions [67]. Improper regulation of these processes have devastating results, as uncontrolled proliferation and invasive migration are the hallmarks of metastatic cancers in epithelial sheets [68].

Many biophysical insights about epithelial tissues come from in vitro studies in which an epithelium is cultured on a flat substrate that is usually coated with ECM proteins. Epithelial cells added to a culture dish float to the bottom and tightly adhere to the proteins adsorbed on the substrate. These adherent cells then bind to one another as they migrate and proliferate, eventually forming a continuous, single layer sheet of cells that migrates, proliferates, and continuously spreads on the substrate when unconstrained [65] (see Fig. 2.5). These systems are much different

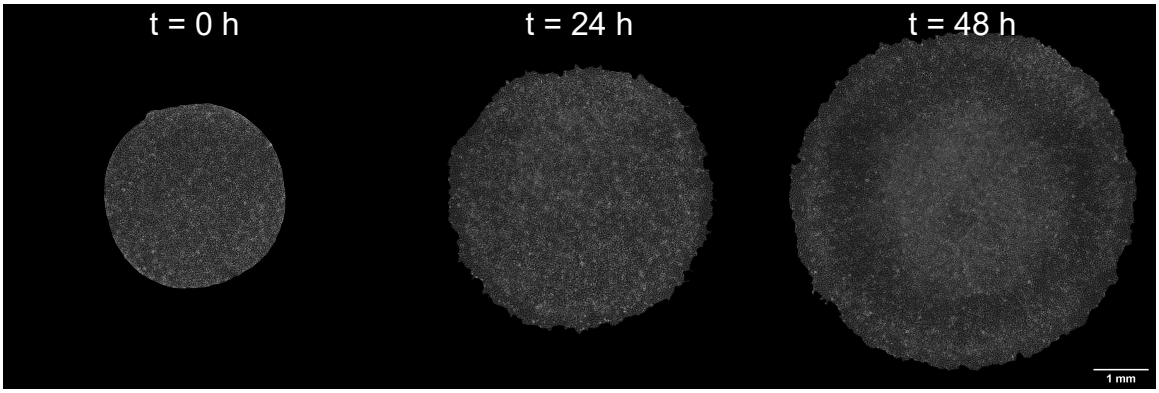

Figure 2.5: Epithelium freely expanding on a tissue-culture dish. Epithelial cells (here, MDCK cells) form tissues in vitro that continuously spread to fill available space.

from other collective cell colonies that are not adhesive [69, 70], as proliferation alone will not drive outward expansion of an epithelial tissue; the tightly-adhered cells must actively crawl into the available space [71]. The foundational behavior of epithelial spreading reflects the basic function of epithelia in vivo to form and restore barriers that are confluent, or gapless [72], and is the major process driving the much of the work presented here.

A majority of the studies discussed in the remainder of this Chapter were conducted with in vitro tissues formed from Madin-Darby Canine Kidney (MDCK) cells, an immortalized cell line originally from a biopsy of a cocker spaniel's kidney epithelial tissue [73]. This cell line features bright cell-cell junctions (when viewed in phase contrast) and conducts elegant, cohesive motions amenable to analyses of cell migration dynamics; additionally, the many mutant cell lines of MDCK cells enable study of the effect of myriad changes to cell structures or visualization of structures or processes that are not as easily visible in wild-type cells [74]. These factors have made MDCK tissue monolayers the gold standard in biophysical studies of epithelia and our primary model system of choice in Chapters 3 and 4.

In this section, we will first introduce the mechanical properties of tissues, the importance of mechanical forces on tissue function, and the impact of the environment

on tissue mechanics and forces; we will then overview the factors influencing cell migration and proliferation, starting with bulk tissue and moving to the effect of different boundary conditions.

2.2.1 Epithelial tissues have dynamic mechanical properties

When a materials scientist encounters a new material, the first question they may ask is "How does it respond to stress?" Does it deform immediately like a solid, or flow at some rate like a fluid? While epithelial tissue is not an ordinary material, these questions have been studied using several approaches.

For solid properties, biological tissues in general achieve an impressive range of mechanical moduli, from the GPa elastic modulus of bone [75] to the single kPa shear and elastic moduli of lung epithelial tissue [76]. Epithelial tissues fall in the softer range of the spectrum, ranging from below one kPa to several hundred kPa [4]. The measured modulus of even the same tissue may vary greatly depending on the method or direction of measurement, for example by three orders of magnitude in spinal cord tissue for microindentation [77] (kPa) vs. tensile extension [78] (MPa)[2][3]. In macroscopic measurement of the Young's modulus of an MDCK epithelial monolayer, stretching the tissue between two posts yielded a ∼20kPa elastic modulus, but this stretch also induced flow, highlighting the viscoelastic nature of this system [79].

Epithelial tissues can flow like a fluid at long timescales when the cell network topology changes, which can be due to cell rearrangement or addition or removal of cells from the monolayer [80]. The viscosity of tissue increases as cell-cell adhesion increases [60, 81], which will depend on the type and amount of cadherin proteins present in the tissue's adherens junctions [82]. In the MDCK monolayer system,

[2]Here, variation may come from the fact that microscopic techniques probe the cytoskeleton while macroscopic techniques probe bulk tissue

[3]Additionally, micro-scale measurements may result in smaller moduli than large-scale measurements because of non-linear strain-stiffening effects that become important only at larger deformations [4]

viscosity has been measured to be in the Pa·min range [79, 83], which is similar to the viscosity of honey. Interestingly, tissue viscosity in MDCK monolayrs was shown to increase by a factor of four over the course of a several hour experiment [83].

This increase in viscosity reflects an almost universal rule in biological tissues whereby tissues become progressively more rigid as they mature past the dynamic developmental and regenerative stages [4, 84]. This holds true in the case of epithelial monolayers as well, which become more viscous, stiff, and jammed over time [83, 85]. Moreover, these material property changes have also been shown to *drive* morphogenesis in embryonic tissues [86, 87]. The mechanisms by which tissues transition between more solid-like states and more fluid-like states is the subject of much study, and we will briefly summarize a few of the leading theories:

i Contact inhibition of locomotion (density-dependent) [20, 88]: Single cells within a tissue become inherently less motile when they are surrounded by greater numbers of cells. As the tissue becomes more crowded due to cell divisions, the tissue will gradually become quiescent and not undergo any cell network topology changes.

ii Jamming due to cell-cell junction maturation (largely density-independent) [85]: Adhesion at cell-cell junctions increases as the tissue matures, increasing the friction between cells. This drives an increase in cell-cell velocity correlations until cells no longer rearrange and the tissue jams.

iii Jamming due to cell shape changes (density independent) [89–91]: Cell adhesion and cortical tension compete to increase and decreases the cell junction length, respectively, and their balance sets a preferred perimeter for cells within the tissue. Cells with higher preferred perimeter can assume irregular shapes that enable "squeezing" between cells and therefore easier cell-cell rearrangement. See Fig. 2.6.

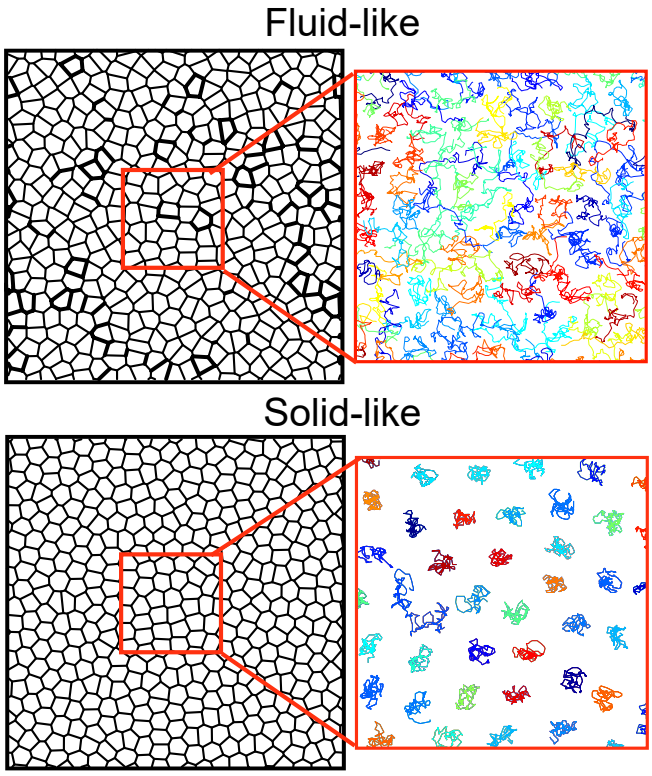

Figure 2.6: Proposed mechanism for tissue unjamming via cell shape change. Tissue shapes (left) and resulting tracks (right) in simulations of cells with high prefered perimeter (top) vs low preferred perimeter (bottom). Low preferred perimeter accompanies tissues that rearrange less frequently as seen by caging of cell tracks. This mechanism has experimental support [90]. Adapted from [91].

While these schools of thought differ in some details, cell density effects (i), cell junction maturation (ii), and cell shape changes (iii) all likely contribute to the solidification and reduction of cell motility in tissues over time.

Overall, epithelial tissues exhibit dynamic, wide-ranging mechanical properties that depend on the cellular state as well as the measurement technique, so native-like deformations should be used in the measurement of tissue mechanical properties whenever possible [4]. These wide-ranging properties accompany the wide-ranging environments to which epithelial tissues may be subject over their lifetime, and we will next see how tissues respond to their environment.

2.2.2 Cells within tissues respond to and actively generate forces

In *On Growth and Form* [92], D'Arcy Thompson argued that physical forces play a critical role in the development of a multicellular organism, opining that "The form of an object is a diagram of forces." It was later proven that bone [93] and blood vessels [94] remodel in response to mechanical stresses. Tissue-scale stretch, in particular, has been shown to initiate mechanical changes and biological processes, fluidizing tissue [95] as well as initiating [96] and orienting [97] cell division events. Forces can also induce a migratory response, and in one study, pulling on a single cell within a tissue caused the cell to migrate in the opposite direction [98].

While tissues are often subject to forces from the environment, they also exert forces on their environment using stress fibers to pull on the ECM through focal adhesions. Measuring these forces can be difficult, but refinement of traction force microscopy techniques over the previous decades made measurement of in vitro cell-ecm forces more accessible [99]. While it was previously assumed that cell-ECM forces within a growing tissue were restricted to only the leading edge, seminal work proved that large, directed traction forces emanated even from well into the tissue bulk [32]. This showed that collective cell migration was much more complicated from a mechanical perspective than simply follower cells passively flowing behind a migratory leading edge.

Cells not only exert forces on their surroundings, but they also exert forces on other cells. While recent advances in bioengineering molecular force-sensing probes have made direct measurement of cell-cell forces possible [100], most of the reporting of cell-cell forces is based on an assumed system-wide force balance of cell-cell and cell-substrate forces [31]. As most traction forces in an expanding monolayer point inward (propelling cells outward), the picture of a tissue under tension as a sort of multicellular tug-of-war begins to come into focus (Fig. 2.7). Here stress builds

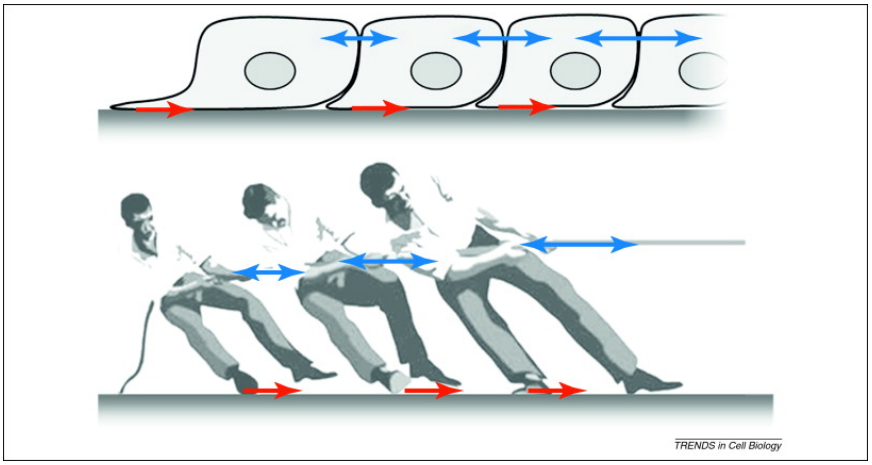

Figure 2.7: Cells build up stress by integrating their traction forces. In analogy to a tug-of-war, cell-cell stress builds up in the bulk of the tissue as cell traction forces co-act. Reproduced from [2], Copyright 2011, with permission from Elsevier.

up as we go from the edge inwards, as the forces of many thousands of cells act together. These effects are relevant in developmental and regenerative contexts, where stresses can propagate over long ranges [55, 101] and are important for the large-scale collective motions that arise in these dynamics situations [102].

2.2.3 Tissues interact with their surroundings: mechanical properties

The mechanical properties of a tissue's environment can also modulate cellular behavior. This realization [103] brought mechanics onto the stage of tissue biology, as biochemical effects were no longer the only game in town. In single cells, it was found that cells spread more and develop more mature stress fibers on stiff substrates than soft substrates [104] and that stem cell differentiation can be controlled by the stiffness of the environment [105].

Interestingly, undifferentiated stem cells exhibit memory of a stiff environment even after being moved to a soft environment [106]. Similarly, tissues in epithelial contexts exhibit memory of their mechanical environment, as they migrate differently

on soft substrates after having migrated over a stiff substrate [107]. In general, tissues migrate faster and divide more often in stiffer environments [108], a fact that should be considered when performing experiments on substrates with much higher stiffness than native physiological environments, as we do in this work. For more information on the biological response of cells and tissues to external forces, mechanics, and geometry, readers are pointed to the robust and growing field of mechanobiology [109].

2.2.4 Cell motion and proliferation in bulk tissue

We now turn our focus to tissue coordination of migration and proliferation. Even in the absence of an external directional migration signal like a gap in the tissue, the motions of individual cells within epithelial tissue are highly coordinated. The correlation length of bulk MDCK monolayer tissue, as measured by the distance at which correlations in the velocity field decay to almost zero, is approximately 200 μm, or about 10-15 cell lengths [110, 111]. These long-range correlations can be partially attributed to the fact that cells in a cohesive epithelium like an MDCK monolayer do not commonly exchange neighbors on timescales below which cell division would naturally separate them [111]. Complementarily, through the interconnected cytoskeleton of many cells, stress propagates over long ranges within an epithelium and allows forces generated by one cell to be "felt" by cells very far away [55]. Additional mechanisms for aligning cell-cell motion have been proposed, the most common of which depends on coupling of cell-cell polarity through the action of cryptic lamellipodia [40, 46]. In any case, the correlation length of an epithelium will vary throughout its lifetime, as correlations increase as its cell-cell junctions mature but decrease when sustained motion becomes impossible after the monolayer becomes very dense [85].

The highly dense and jammed state is the homeostatic state of a healthy epithelium. In homeostasis, cell divisions must occur at the same rate as cell death or cell

extrusions to avoid the opposite problems of loss of tissue or the formation of tumors [112]. During non-homeostatic times like development and regeneration, though, cell divisions must occur rapidly until the organism or organ has reached the appropriate size or the wound is healed. The Hippo pathway is particularly crucial in organism and organ size control, taking cell-cell contact area, local stiffness, cellular energy consumption, and other factors into account in regulating the rate of proliferation and cell death [26]. In general, cell divisions occur less frequently in a tissue as it becomes more dense [20]. However, cell cycle dwell times of MDCK cells were shown to depend more on cell tension than the local density [22], and stretching a tissue that is proliferating slowly can induce rapid cell division [112]. Moreover, the orientation of the cell division axis orients in the direction of maximum tension [113]. Together, we see that the timing and orientation of cell divisions are coordinated in a way that allows the release of mechanical stress.

2.2.5 Boundary condition: free edge

It has been said that "Epithelial sheets abhor a free edge [114]," and indeed, epithelia respond to this boundary condition by spreading into the free space. Epithelial spreading is also an important developmental motif [102], and its similarities to epithelial wound healing means that epithelial spreading and wound healing are generally studied concomitantly. In these 'wound healing' assays, a free edge is introduced to a confluent epithelium in primarily one of two approaches [115] (Fig. 2.8). In the first approach, an epithelial sheet is scratched with a scalpel or injured in some other way, which of course causes cell death, matrix damage, and many other complicating factors [116]. The second approach involves culturing an epithelium against a barrier and removing the barrier [5], which isolates the effect of the free edge introduction and is a major strategy for our experimental work here.

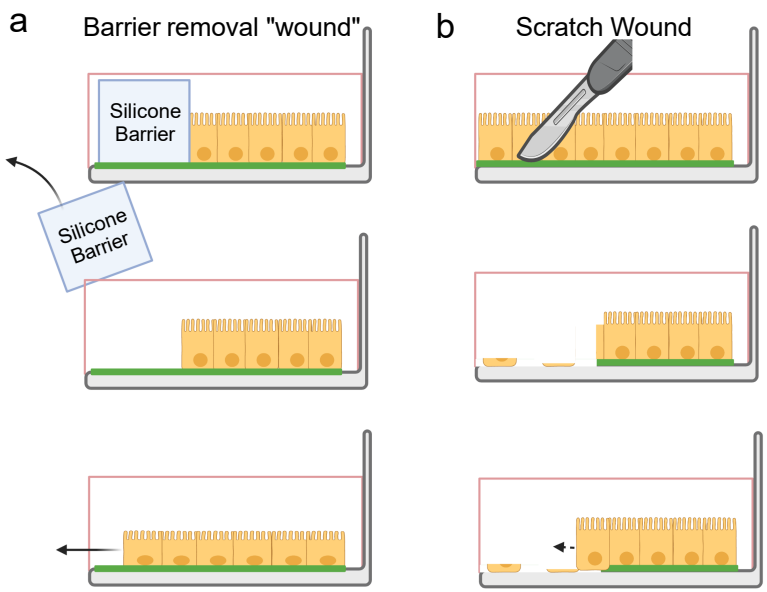

Figure 2.8: Wound healing assays. (a) A barrier limits epithelial expansion (top), and upon removal (middle) the tissue will spread and flatten (bottom). (b) Scratch assays create debris from cell damage and remove matrix proteins from the dish surface, complicating and slowing the tissue expansion process [117]. Created with Biorender.com.

From these wound healing assays, two complementary methods for epithelial closure have been described. The first, called 'purse string' closure (see Fig. 2.9), only occurs in regions of high negative curvature (very small wounds). In these regions, a multicellular actomyosin ring forms around the perimeter of the wound, contracting via myosin motors to bring the edges inward to a single point [118]. The second mechanism, which we will focus on here, involves outward motion of the epithelial sheet edge via active migration, which is also the mechanism for epithelial spreading.

When the edge of an epithelium advances during epithelial spreading, 'leader cells' with pronounced lamellipodia emerge along the edge, heading regions of increased motility that cause the perimeter of the tissue to become ruffled. Cells behind the leading edge "select" the leader by building up stress behind it [19], so predefining tissue geometry can preferentially induce leader cell formation where the tissue assumes high positive curvature and, as a result, higher stress [119]. Leaders cells would be

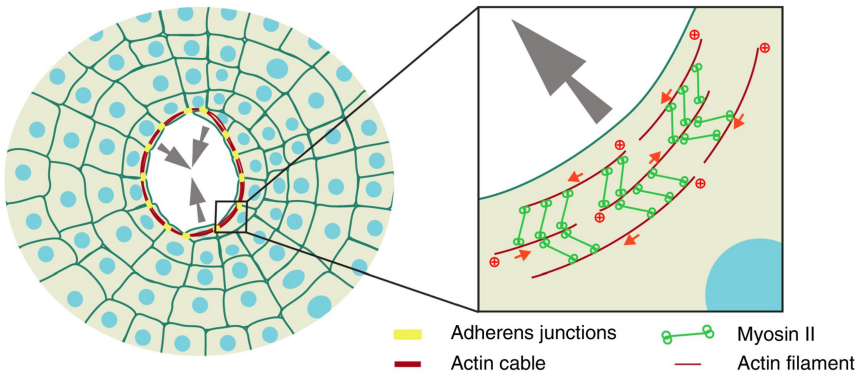

Figure 2.9: Small wounds close by "purse-string" closure. The edge of a wound forms a supracellular contractile actomyosin ring, the contraction of which brings the wound edges together in a method of closure that does not necessitate cell-substrate forces. Adapted from [71], Copyright 2016, with permission from Elsevier.

unlikely to form in regions of high negative curvature, then, where purse string closure is effective [71]. Before it was realized that cells well behind the leading edge contribute forces to cell migration [32], the striking morphology of leader cells seemed to indicate that the leaders simply dragged follower cells along. Instead, leader cells have been shown to organize cell migration by localizing signaling molecules to the leading edge of the tissue [120] and initiating traveling waves of signaling and mechanical deformation that propagate into the tissue bulk.

Traveling waves of cell signaling are especially dramatic after a destructive event such as a scratch assay, where waves of intracellular calcium levels [121], factors effecting cytoskeletal rigidity [116], and Erk signaling [122] travel backward rapidly from the leading edge and dissipate within several minutes. In the case of Erk signalling, an important enzyme for equipping myosin motors for cell migration, the fast propagation is followed by a slower, sustained backward wave that accompanies contraction-dependent mobilization of cells behind the leading edge [122–124]. A model of tissue expansion that couples the concentration of contractile actin with strain is sufficient for reproducing the experimental results and also provides a mechanism for supporting traveling waves in systems lacking inertia [125].

Overall, we see that the boundary condition of a free edge induces the epithelial response of closing gaps; next we will examine the migratory response to geometric confinement, where the edges of a tissue do not have accessible ECM on which to adhere.

2.2.6 Boundary condition: 2D and 3D confinement

Geometric perturbations via selective protein patterning have been one of the most common experimental perturbations in biophysical studies of cells and tissues since it was discovered that changing the shape and area of cell-scale adhesive regions on a substrate determined whether the individual cells adhered to them lived or died [126]. This strategy for introducing geometry involves patterning separate regions of a 2D substrate using adhesive and non-adhesive proteins. The non-adhesive regions do not support focal adhesion attachment, so single cells or cells within tissues cannot migrate onto them using cell-ECM forces [127] (Fig. 2.10).

This 2D geometric confinement can enhance the ability of cells to align their motions with one another by restricting the migratory degrees of freedom. For example, confinement of MDCKS cells within 1D looped, narrow tracks can produce trains of thousands of migrating cells [40], where the single-cell wide tissue of sorts "chases its own tail" [40](Fig. 2.11). Confinement of circular tissues within adhesive patches smaller than the velocity-velocity correlation length (about 10 cells) induces coherent rotation, while adhesive circles larger than the correlation length do not [128]. Epithelial tissue rotations have emerged as an important developmental motif, being necessary for aligning actin bundles [129] and elongating the egg chamber [130] in drosophila as well as forming spherical structures in glandular tissues [131]. Smaller vortices within MDCK tissues on the scale of 2-3 cells arise natively with [38] and without confinement [132] and have been shown to be caused by cell divisions, but

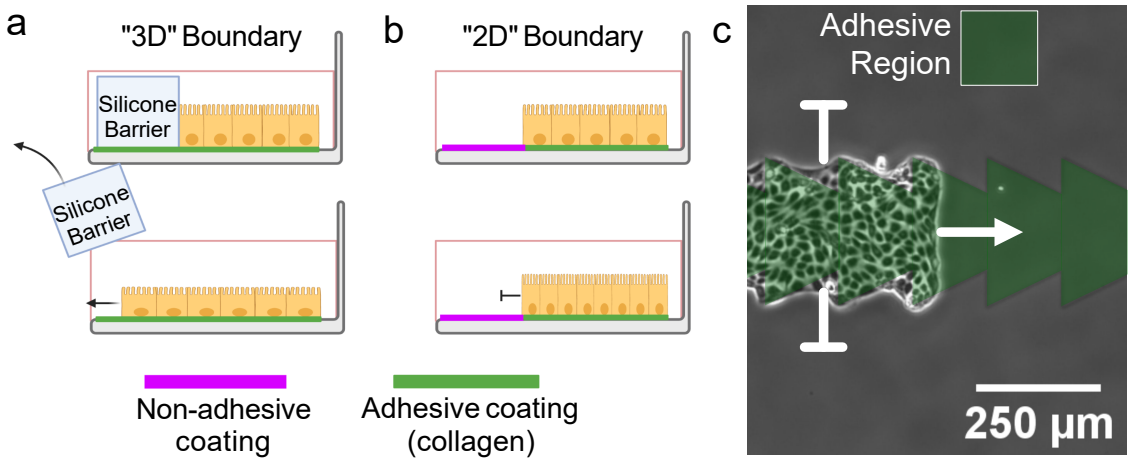

Figure 2.10: Confinement within 2D or 3D boundaries. (a) A barrier limits epithelial expansion (top), and upon removal (bottom) the tissue will spread and flatten. (b) Proteins from the cell media will adsorb onto an uncoated dish, so regions must be patterned with non-adhesive and adhesive proteins selectively to confine migration within regions of interest (top). The tissue will continue to divide without expanding, so its cell density will necessarily increase if there is no cell death or extrusion (bottom). Created with Biorender.com. (c) Example of a tissue migrating through a 2D "microchannel."

collective rotations of a larger scale in unconfined settings have not been observed in cohesive tissues before the work presented here in Chapter 3.

Confinement by 3D structures can also have a strong effect on collective cell migration, in phenomena generally referred to as contact guidance. Nanoscale features initiate contact guidance by aligning the nanoscale cytoskeletal fibers within the cell [133], a process that is relevant in directional cancer migration [134]. At the tissue-scale, confinement of cohesive tissues within tubes [135] or around cylindrical structures [136] also changes migration speeds and cytoskeletal organization. In general, mechanical barriers become the source of mechanical waves just like those originating from a migrating free edge [41], and the presence of a 3D barrier wall at the edge of a tissue increases migration speed at the edge and orients it parallel to the wall [137]. Interestingly, coating the barrier wall with the cell-cell adhesion protein E-cadherin reverses this effect, mimicking the self-healing process [137].

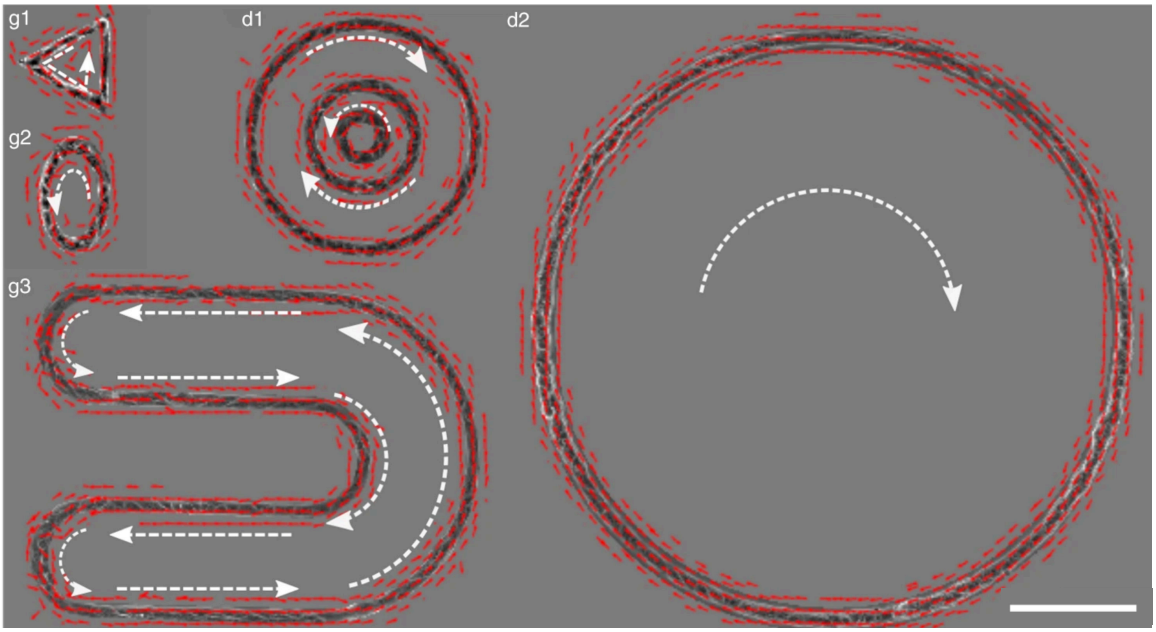

Figure 2.11: Confinement enhances cell-cell coupling. Confinement of tissues within looped tracks produces coherent rotation or migration of trains. Scale bar is 1 mm. Adapted by permission from Springer Nature Customer Service Centre GmbH: Springer Nature, Nature Physics [40], Copyright 2020.

Overall, we see that bulk tissue has native migratory and proliferative behaviors that can be strongly effected by the local boundary conditions. In the next Chapter, we will examine how the behavior of bulk tissue decouples from the edge region in a size-dependent manner.

Chapter 3

Epithelial expansion

3.1 Introduction

Since Virchow's [13] and Ambercrombie's [15] writings in the 19^{th} and 20^{th} centuries, concerted interdisciplinary effort has been brought to bear on understanding how cell-cell interactions give rise to the complex collective behaviors driving so many crucial biological processes. One of the most foundational collective behaviors is collective cell migration— the directed, coordinated motion of cellular ensembles present during critical times of developement, regeneration, and disease [102]. Given this importance, considerable effort spanning biology, engineering, and physics has been directed towards understanding how local cellular interactions can give rise to globally coordinated motions [138, 139].

One of the most foundational collective behaviors is collective cell migration— the directed, coordinated motion of cellular ensembles that enables phenomena such as gastrulation, wound healing, and tumor invasion [102]. Given this importance, considerable effort spanning biology, engineering, and physics has been directed towards understanding how local cellular interactions can give rise to globally coordinated motions [138, 139].

Studies of collective cell migration are most often performed using epithelial tissues due to their fundamental role in multicellular organisms and strong cell-cell adhesion, which in turn gives rise to elegant, cohesive motion. Moreover, given that epithelia naturally form surfaces in vivo, studying epithelial layers in vitro has a physiological basis that can inform our understanding of processes such as healing [5], envelopment [140], and boundary formation [141]. These features have made epithelia both the gold standard in collective cell migration studies, and one of the most well-studied models for biological collective behaviors.

Due to the complexity of collective behaviors, much effort has gone towards reductionist assays that restrict degrees of freedom and ensemble size to simplify analysis and interpretation. One such approach is to confine a tissue within predefined boundaries using micropatterning to create adhesive and non-adhesive regions [128, 142–146]. Such confinement mimics certain in vivo contexts such as constrained tumors as well as aspects of compartmentalization during morphogenesis [147]. Alternately, many studies have explored the expansion of tissues that initially grow into confluence within confinement but are later allowed to migrate into free space upon removal of a barrier. A popular assay of this type relies on rectangular strips of tissue that are allowed to expand in one or both directions [5, 22, 32, 36, 100, 111, 124, 148, 149], where averaging along the length of the strip can reveal coordinated population-level behaviors such as complex migration patterns, non-uniform traction force fields, and traveling mechanical waves. Other studies have focused on the isotropic expansion of micro-scale (< 500 μm diameter) circular tissues using the barrier stencil technique [150] as well as photoswitchable substrates [35]. Still more work has explored approaches to induce directional migration, from geometric cues to applied electric fields [39, 151].

In contrast to micro-scale confinement assays, other work has focused on large, freely-expanding tissues of uncontrolled initial size and shape, which grow from either

single cells [20, 152] or cell-containing droplets [153, 154]. Related experiments track long-term growth of cell colonies via images taken once per day over several days, but this low temporal resolution cannot access timescales over which migration is important [152, 155]. Thus, there is still a lack of assays to study long-term expansion and growth of large-scale tissues with precisely-controlled initial conditions, especially initial tissue size, shape, and density.

To address this gap, we leveraged bench-top tissue patterning [5, 137] to precisely pattern macro-scale circular epithelia of two sizes (>1 mm in diameter) and performed long-term, high frequency, time-lapse imaging after release of a barrier. To elucidate the consequences of size effects on the tissue, we tracked every cell, relating the overall expansion kinetics to cell migration speed, cell density, and cell-cycle dynamics. We find that, whereas the tissue edge dynamics is independent of the initial conditions, the tissue bulk exhibits size-dependent patterns of cell proliferation and migration, including large-scale vortices accompanied by dynamic density profiles. Together, these data comprise the first comprehensive study of macro-scale, long-term epithelial expansion, and our findings demonstrate the importance of exploring collective cell migration across a wider range of contexts, scales, and constraints.

3.2 Materials and Methods

3.2.1 Cell culture

All experiments were performed with MDCK-II cells expressing the FUCCI cell-cycle marker system as received from: [21]. After treatment with Mycoplasma Removal Agent (MPI Biological), cells tested negative for mycoplasma (MycoProbe, R&D Systems). We cultured cells in MDCK media consisting of low-glucose (1 g/L) DMEM with phenol red (Gibco, USA), 1 g/L sodium bicarbonate, 1% strepto-

mycin/penicillin, and 10% FBS (Atlanta Biological, USA). Cells were maintained at 37°C and 5% CO_2 in humidified air.

3.2.2 Tissue patterning

We coated tissue-culture plastic dishes (BD Falcon, USA) with type-IV collagen (MilliporeSigma, USA) by incubating 150 μL of 50 μg/mL collagen on the dish under a glass coverslip for 30 minutes at 37°C, washing 3 times with deionized distilled water (DI), and allowing the dish to air-dry. We then fabricated silicone stencils with cutouts of desired shape and size and transferred the stencils to the collagen coated surface of the dishes. Stencils were cut from 250 μm thick silicone (Bisco HT-6240, Stockwell Elastomers) using a Silhouette Cameo vinyl cutter (Silhouette, USA). We then seeded the individual stencils with cells suspended in media at 1000 cells/mL. Suspended cells were concentrated at $\sim 2.25 \times 10^6$ cells/mL and pipetted into the stencils at the appropriate volume. Care was taken not to disturb the collagen coating with the pipette tip. To allow attachment of cells to the collagen matrix, we incubated the cells in the stencils for 30 minutes in a humidified chamber before flooding the dish with media. We then incubated the cells for an additional 18 hours to allow the cells to form monolayers in the stencils, after which the stencils were removed with tweezers. Imaging began 30 minutes after stencil removal, while cells were still actively cycling (Fig. 3.1. Media without phenol red was used throughout seeding and imaging to reduce background signal during fluorescence imaging.

3.2.3 Live-cell Time-lapse Imaging

All imaging was performed with a 4X phase contrast objective on an automated, inverted Nikon Ti2 with environmental control (37°C and humidified 5% CO2) using NIS Elements software and a Nikon Qi2 CMOS camera. Phase contrast images were captured every 20 minutes, while RFP/GFP channels were captured every 60 minutes

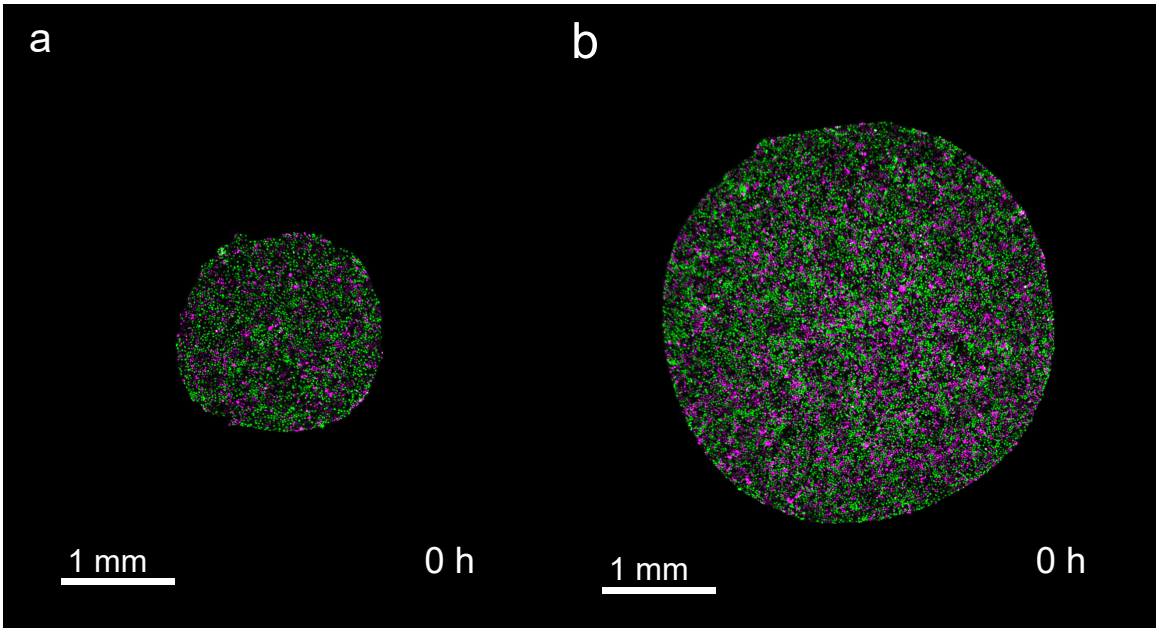

Figure 3.1: Actively cycling cells at experimental start. Cell cycle is well mixed at t0 for small (a) and large (b) tissues. Magenta cells are those in G0-G1-S phases of the cell cycle while green cells are those in S-G2-M phases.

at 25% lamp power (Sola SE, Lumencor, USA) and 500 ms exposure time. No phototoxicity was observed under these conditions for up to 48 hrs. Final images were composited from 4x4 montages of each dish using NIS Elements.

3.2.4 Tissue edge radial velocity

Tissues were segmented to make binary masks using a custom MATLAB (Mathworks) script. Tissue edge radial velocity was measured from the binary masks within more than 200 discrete sectors of the tissue; the edge radial velocity of all sectors were averaged to arrive at the tissue average edge radial velocity. Radial velocity at each sector was calculated for each timepoint as the rate of change of the average extent of the boundary pixels of the sector, utilized a rolling average of 3 timepoints (1 h) to account for capture phase offsets resulting from capturing phase and fluorescence images at different frequencies. Sectors originated from the center of each tissue at

the initial timepoint and were $\sim 20\mu$m wide at the edge of the tissue at the starting point.

3.2.5 Cell counts

The FUCCI system contains a period after M-phase where cells go dark, making FUCCI unreliable for cell counting. Instead, we developed and trained a convolutional neural network to reproduce nuclei from 4X phase contrast images using our in-house Fluorescence Reconstruction Microscopy tool [156] . The output of this neural network was then segmented in ImageJ to determine nuclei footprints and centroids.

3.2.6 Tissue PIV and density measurements

Tissue velocity vector fields were calculated from 2x2 resized phase contrast image sequences using the free MATLAB package PIVLab [157] with the FFT window deformation algorithm. We used a 1st pass window size of 64×64 pixels and second pass of 32×32 pixels, with 50% pixel overlaps. This resulted in a 115×115 μm window. The window size was chosen to be smaller than the velocity-velocity correlation length but large enough to enable fast computation of PIV fields for many tissues.

Local density was also calculated for each PIV window by counting the number of approximate nucleus centroids in that window. Data from PIV was smoothed in time with a moving average of 3 time points centered at each timepoint as before.

3.2.7 Average kymographs

First, we constructed kymographs for individual tissues using distance from the tissue center as the spatial index for each measurement window corresponding to a kymograph pixel. We did not plot kymograph pixels for which more than 95% of the

measurements at that distance were beyond the tissue footprint. We then averaged the individual tissue kymographs, aligning by the centers.

3.2.8 Cell density simulation

To test whether the observed spatiotemporal evolution of density $\rho(r,t)$ could be explained by flow of material (rather than divisions, extrusions, and cell death), we solved the continuity equation for a homogenous tissue in a circular geometry with spatiotemporal evolution of average radial velocity $v_r(r,t)$ as measured from PIV in experiments (Fig. 3.7b). The continuity equation is

$$\frac{\partial \rho}{\partial t} = -\nabla \cdot \mathbf{j} + k_0 \rho, \tag{3.2.1}$$

where a homogeneous cell proliferation rate $k_0 = 1.04 h^{-1}$ is assumed throughout the tissue, which corresponds to the cell doubling time of 16 h. The current density is $\mathbf{j} = \rho \mathbf{v_r} - D\nabla\rho$, where we included a diffusion term with a small diffusion constant $D = 0.22\,\mathrm{mm}^2/\mathrm{h}$ for numerical stability.

The continuity equation (3.2.1) was discretized using the finite volume method [158], which is briefly summarized below. The tissue domain was divided into an inner circle Ω_0 of radius $r_{1/2} = \frac{1}{2}\Delta r$ and circular annuli Ω_i with inner radii $r_{i-1/2} = (i-\frac{1}{2})\Delta r$ and outer radii $r_{i+1/2} = (i+\frac{1}{2})\Delta r$, respectively, where $i = 1, 2, 3, \ldots$ and $\Delta r = 115\mu m$ corresponds to the width of 1 window in the PIV analysis (see Fig. 3.2). The continuity equation (3.2.1) was then integrated over the inner circle Ω_0 and circular annuli Ω_i as

$$\frac{1}{A_0}\int_0^{r_{1/2}} (2\pi r dr)\frac{\partial \rho}{\partial t} = \frac{1}{A_0}\int_0^{r_{1/2}} (2\pi r dr)\big[-\nabla \cdot \mathbf{j} + k_0\rho\big], \tag{3.2.2a}$$

$$\frac{1}{A_i}\int_{r_{i-1/2}}^{r_{i+1/2}} (2\pi r dr)\frac{\partial \rho}{\partial t} = \frac{1}{A_i}\int_{r_{i-1/2}}^{r_{i+1/2}} (2\pi r dr)\big[-\nabla \cdot \mathbf{j} + k_0\rho\big], \tag{3.2.2b}$$

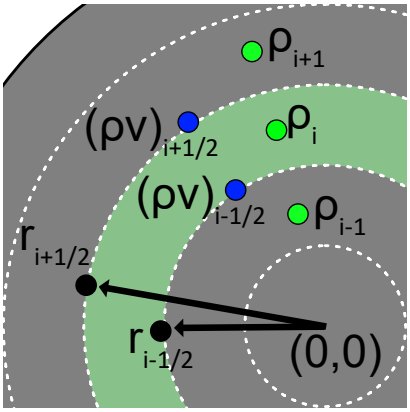

Figure 3.2: Discretization scheme.

where $A_0 = \pi r_{1/2}^2$ is the area of the inner circle Ω_0 and $A_i = \pi r_{i+1/2}^2 - \pi r_{i-1/2}^2$ is the area of the circular annulus Ω_i. The integrals in equation (3.2.2) can be approximated as

$$\frac{\partial \rho(0,t)}{\partial t} = -\frac{2\pi}{A_0} r_{1/2} j(r_{1/2},t) + k_0 \rho(0,t), \tag{3.2.3a}$$

$$\frac{\partial \rho(r_i,t)}{\partial t} = -\frac{2\pi}{A_i}\left[r_{i+1/2} j(r_{i+1/2},t) - r_{i-1/2} j(r_{i-1/2},t)\right] + k_0 \rho(r_i,t). \tag{3.2.3b}$$

Here, density profiles $\rho(r_i,t)$ are evaluated at $r_i = i\Delta r$ for all $i = 0,1,2,\ldots$. Current densities are evaluated as $j(r_{i+1/2},t) = \rho(r_{i+1/2},t) v_r(r_{i+1/2},t) - D[\rho(r_{i+1},t) - \rho(r_i,t)]/\Delta r$ for all $i = 0,1,2,\ldots$, where $\rho(r_{i+1/2},t) = [\rho(r_i,t) + \rho(r_{i+1},t)]/2$ and $v_r(r_{i+1/2},t) = [v_r(r_i,t) + v_r(r_{i+1},t)]/2$ (see Fig. 3.2). Density profiles $\rho(r_i,t)$ were then obtained by integrating equation (3.2.3) with the forward Euler method using a time step $\Delta t = 20$ min to align with experimental data collection of radial velocity profiles $v_r(r_i,t)$ from Fig. 3.7b. The initial conditions were $\rho(r_i,0) = 2700\,\text{cells/mm}^2$ for $r_i < r_{tissue}$ and $\rho(r_i,0) = 0\,\text{cells/mm}^2$ for $r_i > r_{tissue}$, where r_{tissue} is the radius of tissue at the beginning of experiment. For comparison with experimental data (see Fig. 3.12), we thresholded the kymographs of simulated density at $100\,\text{cells/mm}^2$, which corresponds to much lower density than a confluent tissue.

3.2.9 Cell cycle analysis

The Fucci system consists of an RFP and GFP fused to proteins Cdt1 and Geminin, respectively [159]. Cdt1 levels are high during G1 and low during the rest of the cell cycle, while Geminin levels are high during the S, G2, and M phases [21, 159]. After capturing the appropriate fluorescence images, preprocessing was implemented identically for GFP and RFP channels to normalize channel histograms. To determine local cell cycle fraction, we determined the median value of RFP and GFP signal for each cell nucleus and manually selected thresholds for RFP and GFP signals separately to classify cell cycle for each cell as G0-G1-S (RFP above threshold), S-G2-M (RFP below threshold and GFP above threshold), or postmitotic (RFP and GFP below threshold). Local cell cycle fraction of each state could then be easily computed for each PIV pixel. Note that S phase (both RFP and GFP signals above threshold) did not prove to be a reliable feature for segmentation.

3.3 Results

3.3.1 Expansion of millimeter-scale epithelia of different sizes and shapes

We began by characterizing the overall expansion and growth of tissues with the same cell density but different initial diameters of 1.7 mm and 3.4 mm (a 4X difference in area, with tissues hereafter referred to as either "small" or "large"), using an MDCK cell line stably expressing the 2-color FUCCI cell-cycle marker [21, 22, 154, 159, 160]. We patterned the tissues by culturing cells in small and large circular silicone stencils for ∼18 hrs [5, 137], whereupon stencils were removed and tissues were allowed to freely expand for 46 h (Fig. 3.3a, Supplementary Video 1), while images were collected at 20 minute intervals using automated microscopy (see Materials and Methods). Our

cell seeding conditions and incubation period were deliberately tuned to ensure that the stencils did not induce contact inhibition of proliferation prior to stencil removal (checking FUCCI to ensure the tissue was not arrested in G1, see Materials and Methods and Fig. 3.1). Upon stencil removal, tissues expanded while maintaining their overall circular shape throughout the 2-day experiment. Unless otherwise noted, cell density at stencil removal was $\sim$2700 cells/mm^2, a value consistent with active and growing confluent MDCK epithelia [21, 22].

First, we measured relative areal increase (Fig. 3.3b) and relative cell number increase (Fig. 3.3b inset) of small and large tissues. By 46 h, small and large tissues had increased in area by 6.4X and 3.3X, respectively, while cell number increased by 9.2X and 5.5X, respectively. Since proliferation outpaces area expansion in long-term growth, average tissue density increased by the end of the experiment. The evolution of average tissue density was more complex, however, as small tissues experienced a density decrease from 4-12 h while large tissues exhibited a monotonic increase in cell density (Fig. 3.3c). Accordingly, at any given time after stencil removal, large tissues had a higher density than small tissues. Non-monotonic density evolution has been observed in thin epithelial strips [5] and likely arises from competition between migration and proliferation dynamics, which we discuss later.

We then related area expansion to the kinematics of the tissue edge. To quantify edge motion, we calculated the average radial velocity of the tissue boundary, $v_r(t)$, at 1 hr intervals over 46 hrs (Materials and Methods). We found that v_r is independent of both tissue size and a wide range of initial cell densities, in all cases reaching $\sim$30 μm/h after $\sim$16 h (Fig. 3.3d). Before reaching this constant edge velocity, v_r ramps up during the first 8 h after stencil removal, and, notably, overshoots its long-time value by almost 30%. We hypothesize that the overshoot is due to the formation of fast multicellular finger-like protrusions that emerge at the tissue edge in the early stages of expansion and then diminish (Fig. 3.4a). Indeed, the peak in

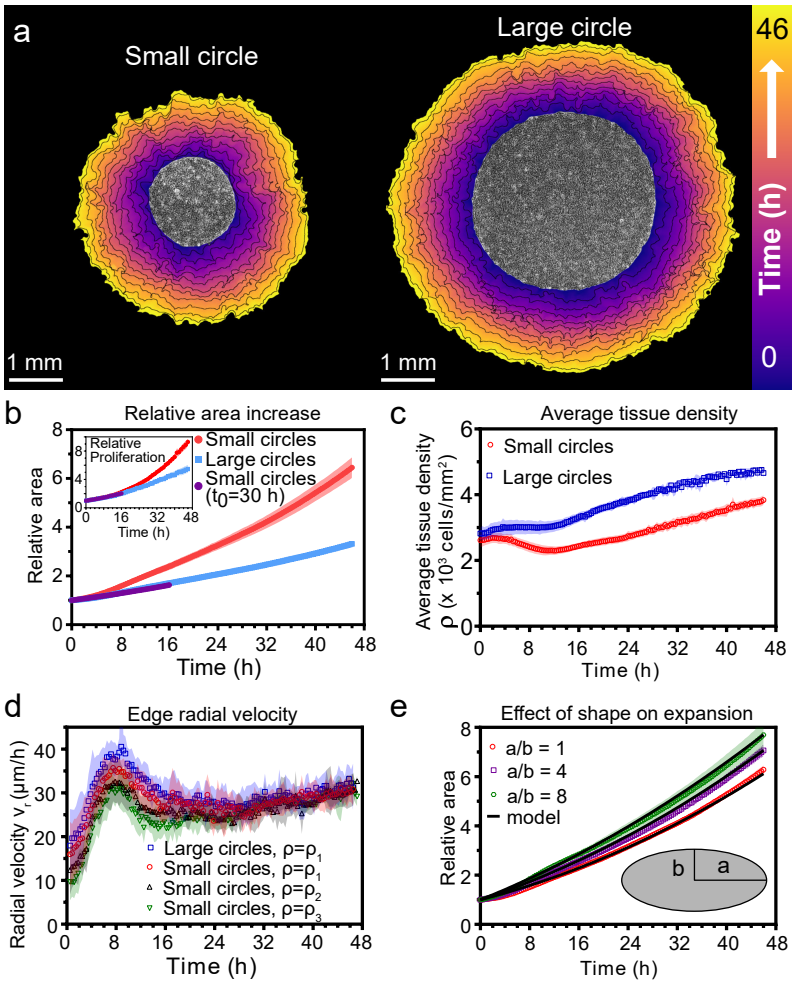

Figure 3.3: Expansion dynamics of millimeter-size cell monolayers. (a) Footprint throughout 46 h expansion period of representative small (left) and large (right) circular tissues, with the tissue outlines drawn at 4 h increments. Initial diameters were 1.7 mm and 3.4 mm. (b) Small circles exhibit faster relative area, $A(t)/A_0$, increase than large circles, where A_0 and $A(t)$ are the areas of tissues at the beginning of the experiment and at time t, respectively. Purple points show the data from small tissues using the time $t_0 = 30$ h when they reached the size of the large circles. Inset: Relative proliferation $N(t)/N(0)$ for small and large tissues. (c) Average tissue density $\rho(t) = N(t)/A(t)$, where $N(t)$ is the number of cells in a tissue at time t. (d) Edge radial velocity v_r. We grouped initial cell densities as $\rho_1 = [2350, 3050]$ cells/mm^2, $\rho_2 = [1650, 2350)$ cells/mm^2, and $\rho_3 = [1300, 1650)$ cells/mm^2. (e) Experimental data on tissue shape and model fits with $v_n \approx 29.5$ μm/h for all tissues, yielding normalized χ^2 values of 0.79, 0.13, and 0.06 for aspect ratios of 8, 4, and 1 respectively, calculated as $\frac{1}{N}\sum_{i=1}^{N}\frac{(u_i-\mu_i)^2}{\sigma_i^2}$, where N is the number of time-points in the curve, u_i are the model predictions, and μ_i and σ_i are the mean and standard deviation of the measured values, respectively. With these definitions, a fit with $\chi^2 < 1$ is good. Shaded regions correspond to standard deviations.

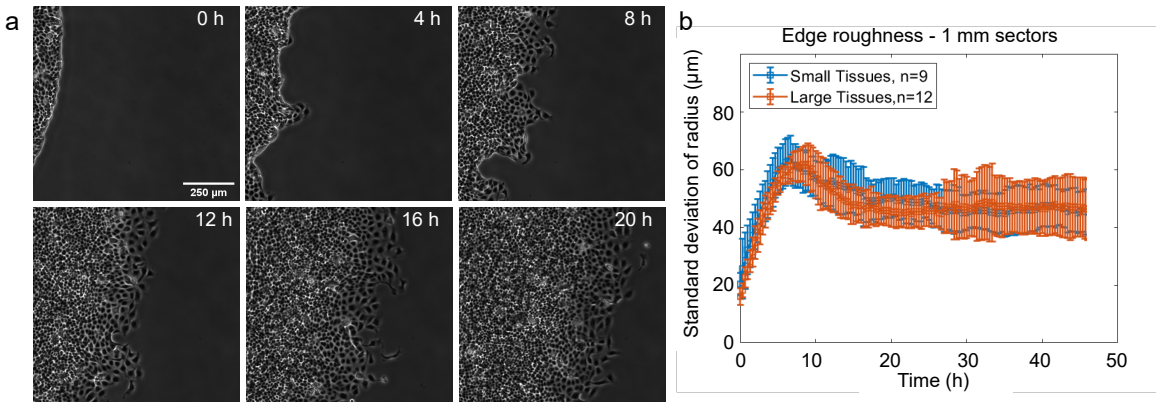

Figure 3.4: Evolution of tissue edge roughness. (a) Representative time series of tissue edge morphology, which shows an increase in edge roughness from 0-8 h followed by decrease from 12 h on. (b) Quantifying edge roughness as the standard deviation of the boundary radius of 1mm sectors, we see that the dynamics of edge roughness follow the dynamics of v_n from Fig. 3.3d).

edge roughness occurs at the same time as the peak in v_r (Fig. 3.4b). This hypothesis is further supported by a recent model showing that edge acceleration (as observed during the first 8 h in Fig. 3.3d) leads to finger formation [161]. It is remarkable that the edge radial velocity $v_r(t)$ is independent of the initial tissue size and density, especially considering that cell density evolution shows opposite trends at early stages of expansion for small and large tissues (Fig. 3.3c). This observation suggests that the early stages of epithelial expansion are primarily driven by cell migration rather than proliferation or density-dependent decompression and cell spreading.

The observation that v_r is independent of tissue size ought to explain why small tissues have faster relative area expansions than large tissues. We hypothesized that the relation between tissue size and areal increase could be attributed primarily to the perimeter-to-area ratio. Assuming a constant edge velocity v_n normal to the tissue boundary, the tissue area increases as $dA = Pv_n dt$, where P is the perimeter of tissue and dt is a small time interval. Thus, the relative area increase $dA/A = (P/A)v_n dt$ scales as the perimeter-to-area ratio, which is inversely proportional to the radius for circular tissues, so the relative area increases faster for smaller tissues (Fig. 3.3b).

To verify that the perimeter-to-area ratio is proportional to the relative area increase, we analyzed elliptical tissues with the same area and cell density but different perimeters. Increasing the perimeter-to-area ratio of a tissue by increasing its aspect ratio indeed leads to faster relative area expansion (Fig. 3.3e). A simple, edge-driven expansion model with linear increase of the tissue major and minor axes predicts $A(t)/A(0) = (a + v_n t)(b + v_n t)/(ab)$, where a and b are the initial major and minor axes of the tissue. This model fits our data well assuming the same edge speed $v_n \simeq 29.5$ μm/h for all tissues (Fig. 3.3e). This observation suggests that edge speed is mostly independent of edge curvature. However, we measure a smaller edge speed at the major axes of ellipses, which are high-curvature points with radius of curvature $r_c \lesssim 0.75$ mm (Fig. 3.5). Such high curvatures are concentrated around the major axes of our elliptical tissues. However, most of the tissue edge has a smaller curvature, and therefore advances at a curvature-independent speed. Further, the slower v_n at the tip actually causes high curvature regions to blunt over time. As a result, our model with a single edge speed $v_n \simeq 29.5$ μm/h is sufficient to capture the area expansion of both circular and elliptical tissues (Fig. 3.3e).

Together, our findings demonstrate that epithelial shape and size determine area expansion dynamics via the perimeter-to-area ratio. This relationship results from the fact that tissues exhibit a constant, size-independent, migration-driven edge speed normal to tissue boundary. Since initial tissue size does not affect boundary dynamics, but does impact the relative growth and expansion of the tissue, we hypothesize that cells in the tissue bulk exhibit tissue size-dependent behaviors.

3.3.2 Spatiotemporal dynamics of migration speed and radial velocity

Having demonstrated the role of the boundary in the expansion of large-scale epithelia, we sought to relate tissue areal expansion rate to internal collective cell migration

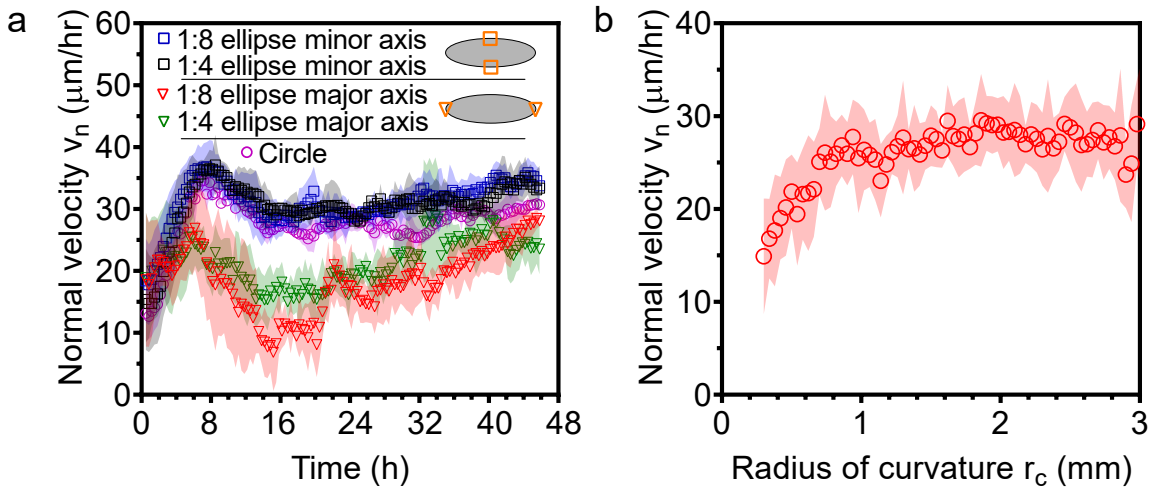

Figure 3.5: Normal edge velocity v_n of elliptical tissues at the major and minor axes. (a) Elliptical tissues spread with different normal velocities along their major and minor axes. Data are from elliptical tissues with the same initial area than small circular tissues. (b) Normal expansion velocity is roughly independent of the local radius of curvature r_c of the tissue edge for large radii of curvature. For radii of curvature smaller than $\sim$ 1 mm, the normal velocity decreases with decreasing r_c. This plot includes data both from circular tissues and from the major and minor axes of elliptical tissues, excluding the first 16 hours of expansion to eliminate any affects from initial front acceleration. Curvature at the major and minor axes of growing tissues was approximated at each time-point by fitting an ellipse to the tissue footprint and taking the radius of curvature at the minor and major axes as b^2/a and a^2/b, respectively, where a is the major semi-axis length and b is the minor semi-axis length.

dynamics. We used Particle-Image-Velocimetry (PIV, Materials and Methods) to obtain flow fields describing cell migration within freely expanding epithelia [5, 111, 151, 162, 163]. We constructed kymographs (Materials and Methods) to display the full spatiotemporal flow patterns of the tissue [100, 124], averaging over the angular direction(Fig. 3.6) and over 16 tissues (Fig. 3.7a,b). We also separately show time evolution (Fig. 3.7c) and spatial profiles (Fig. 3.7d) of speed and radial velocity to compare small and large tissues.

Kymographs of speed and radial velocity reveal the existence of an edge region of fast, outward, radial cell motion (Fig. 3.7 a,b), with speeds similar to the radial edge velocity reported in Fig. 3.3d. Up to $\sim$500 μm from the tissue edge, the speed and

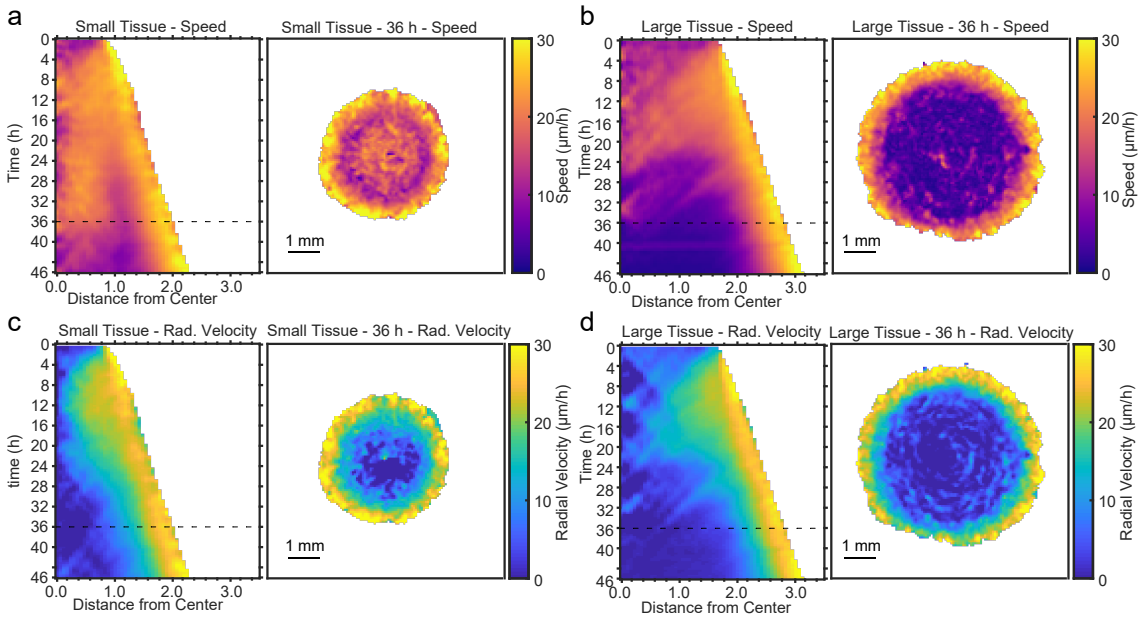

Figure 3.6: Representative kymographs and heatmaps for speed and radial velocity. (a-d) Dashed lines indicate timepoint of 36 h to which heatmaps correspond. Kymographs and heatmaps in each column are from the same representative tissue.

radial velocity profiles are practically identical for small and large tissues (Fig. 3.7d), showing that cell motion near the tissue edge is independent of tissue size.

The tissue centers, in contrast, exhibit size-dependent behaviors. For both small and large tissues, a wave front of cell speed and radial velocity propagates toward the tissue centers at $\sim$90 μm/h (Fig. 3.7a and b, dashed lines). This is approximately 3X faster than the tissue edge speed, consistent with previously described waves of strain rate in cell monolayers [124]. Soon after the wave of radial velocity reaches the center, it retreats, leaving a region of low radial velocity that increases in extent in the center of both small and large tissues (Fig. 3.7b). This decrease of radial velocity is accompanied by a reduction in cell speed in the center of large tissues but not in small tissues, in which cell speed remains high until 36 h (Fig. 3.7a, 3.7c Bottom). We examine the behavior of this high-speed but low-radial-velocity central region of small tissues in the next section.

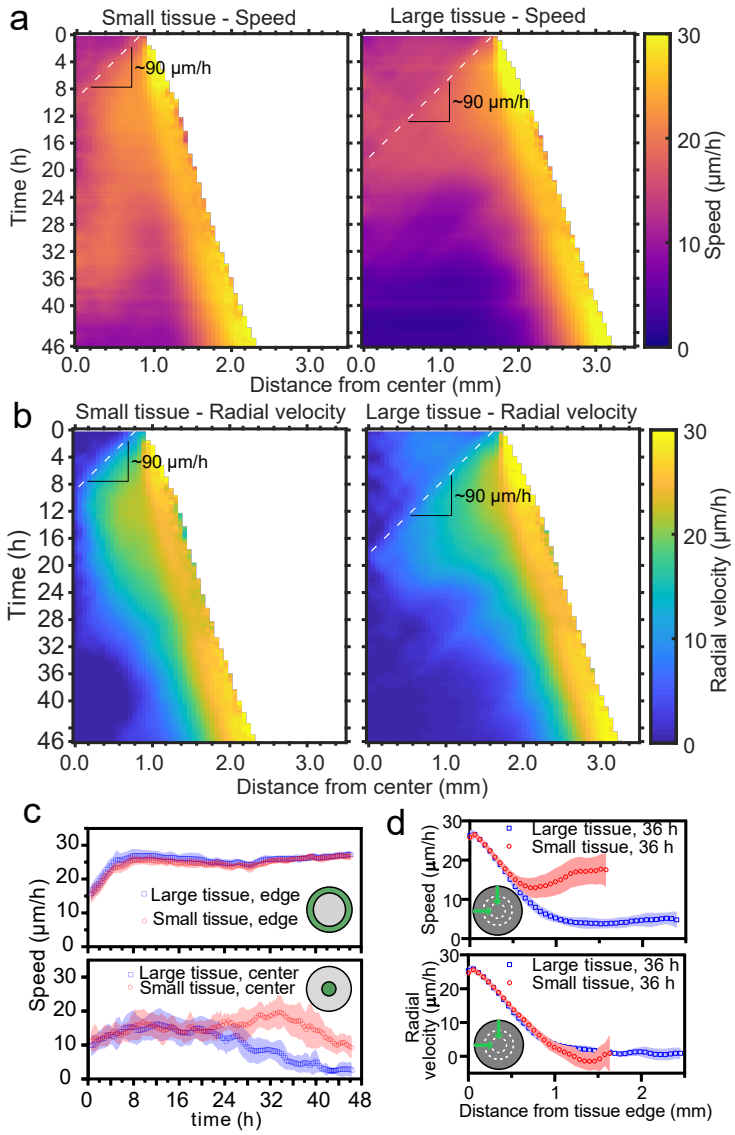

Figure 3.7: Speed and radial velocity in inner and outer tissue zones. (a,b) Average kymographs of (a) speed and (b) radial velocity v_r throughout expansion for small (left) and large (right) tissues. (c) Evolution of the average speed of boundary (top) and center (bottom) zones, defined as regions extending $\sim$200 μm from the tissue center and tissue edge, respectively. This width of the zones corresponds approximately to the velocity-velocity correlation length for MDCK cells [111]. (d) Profiles of speed (top) and radial velocity (bottom) at 36 h, from the edge of the tissue inwards. Arrows indicate that the tissues are indexed from the edge of the tissue inwards. Speed and radial velocity profiles of large and small tissues match closely for the first 500 μm from the tissue edge. The average difference between the profiles in this zone is 0.39 μm/h (speed) and 0.27 μm/h (radial velocity), respectively, while the smallest standard deviation for any point in either profile is 0.56 μm/h.

3.3.3 Emergence of large-scale vortices

The propagation of low radial velocity out from the center of small tissues coincides with the formation and expansion of a millimeter-scale, persistent vortex (see Fig. 3.8a, Supplementary Video 1). These large vortices are observed in both small and large tissues, but they only reach tissue-spanning sizes in small tissues.

To visualize the form and scale of these vortices, we tracked individual cell motion and colored cell trajectories according to their orientation [165] for a representative small and large tissue tissue (Fig. 3.8a-b). The vortex period was most apparent from 20-40 h in small tissues and can also be detected in 0-20 h in large tissues. During the vortex period in small tissues, cell trajectories are primarily radial in the boundary zone, but mainly tangential in the entire central zone (Fig. 3.8c). To understand the emergence of the vortices, we build on a continuum physical model of tissue spreading that describes the cell monolayer as a two-dimensional compressible active polar fluid [83, 144, 161]. Consistent with our velocity measurements (Fig. 3.7c), we assume that cells at the edge zone are radially polarized and motile, whereas cells in the bulk of the tissue are unpolarized and non-motile. We describe cell polarization at a coarse-grained level via a polarity field $\mathbf{p}$ that obeys the following dynamics [138]:

$$\partial_t \mathbf{p} = \frac{\mathbf{h}}{\gamma} + \nu_s \mathbf{v}. \tag{3.3.1}$$

Here, γ is the rotational viscosity that damps polarity changes. Respectively, $\mathbf{h} = -a\mathbf{p} + K\nabla^2\mathbf{p}$ is the so-called molecular field that governs polarity relaxation: the first term drives the polarity to zero, and the second term opposes spatial variation of the polarity field. As a result of these terms, the radial polarity at the tissue edge decays over a length scale $L_c = \sqrt{K/a}$ into the tissue bulk.

With respect to previous models of tissue spreading, we add the last term in Eq. 3.3.1, which couples the polarity to the tissue velocity field $\mathbf{v}$. This coupling

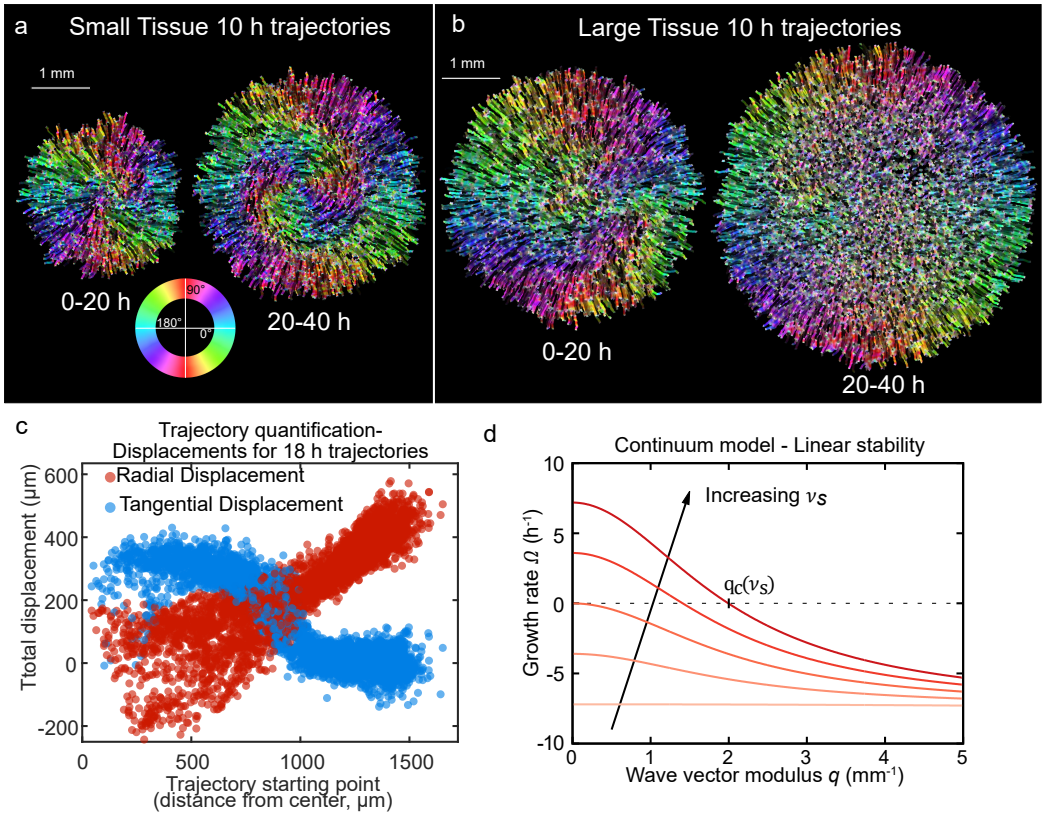

Figure 3.8: Vortex formation in expanding tissues. Vortical flows seen from 10 h traces of cell trajectories in small (a) and large (b) tissues, colored according to its local orientation. We first generated a plot of all relevant trajectories [164] colorized randomly in grayscale using a custom MATLAB (Mathworks) script. We then used the Fiji plugin OrientationJ on this plot to colorize the resulting image according to orientation [165]. (c) Displacements from 18 h trajectories in a representative small tissue vortex show a transition from high to low tangential displacement moving away from the center of small tissues. (d) Growth rate of perturbations of wave vector modulus q around the unpolarized state of the tissue bulk, Eq. 3.3.3. Perturbations with wavelength longer than $2\pi/q_c$ grow ($\Omega > 0$), leading to large-scale spontaneous flows in the tissue bulk. We show curves for the following values of the polarity-velocity coupling parameter: $\nu_s = 0, 1, 2, 3, 4$ mm^{-1}. For the remaining parameters, we took $T_a = 100$ Pa/μm, $\xi = 100$ Pa·s/μm^2, $\eta = 25$ MPa·s, $\gamma = 10$ kPa·s, $a = 20$ Pa, $K = 10$ nN, as estimated in Ref. [144].

is a generic property of active polar fluids interacting with a substrate [166–169]. Previous works in agent-based models showed that similar polarity-velocity alignment interactions [138] can lead to waves [146], flocking transitions [170–174], and vortical flows [175–180] in small, confined, and polarized tissues. Here, using a continuum model, we propose that cell polarity not only aligns with but is also generated by

tissue flow, and we ask whether this polarity-velocity coupling can lead to large-scale spontaneous flows in the unpolarized bulk of unconfined tissues.

To determine the flow field $\mathbf{v}$, we impose a balance between internal viscous stresses in the tissue, with viscosity η, and external cell-substrate forces, including viscous friction with coefficient ξ, active traction forces with coefficient T_a, and the cell-substrate forces associated with the polarity-velocity coupling ν_s:

$$\eta\nabla^2\mathbf{v} = \xi\mathbf{v} - T_a\mathbf{p} - \nu_s\mathbf{h}. \tag{3.3.2}$$

This force balance predicts that even if cell polarity, and hence active traction forces, are localized to a narrow boundary layer of width $L_c \sim 50$ μm [83, 144], cell flow can penetrate a length $\sim \lambda = \sqrt{\eta/\xi}$ into the tissue. Based on our measurements (Fig. 3.7d), we estimate $\lambda \sim 0.5 - 1$ mm, which is larger than the velocity correlation length of ~ 200 μm in the tissue bulk [111].

A linear stability analysis of Eqs. 3.3.1 and 3.3.2 shows that perturbations of wave number q around the quiescent ($\mathbf{v} = 0$) and unpolarized ($\mathbf{p} = 0$) state grow with a rate

$$\Omega(q) = -\frac{a}{\gamma}(1 + L_c^2q^2) + \frac{T_a\nu_s - a\nu_s^2(1 + L_c^2q^2)}{\xi(1 + \lambda^2q^2)}. \tag{3.3.3}$$

This result shows that, if $T_a\nu_s > a(\xi/\gamma + \nu_s^2)$, the unpolarized state of an active polar fluid described by Eqs. 3.3.1 and 3.3.2 is unstable ($\Omega > 0$) to perturbations of wavelength longer than a critical value $2\pi/q_c$ given by $\Omega(q_c) = 0$ (Fig. 3.8d). This analysis suggests that, for tissues larger than this critical value $\sim 2\pi/q_c$, the quiescent tissue bulk becomes unstable and starts to flow spontaneously at large scales, consistent with the emergence of large-scale vortices. The mechanism of this instability is the positive feedback between flow-induced cell polarization and the flows due to migration of polarized cells. Previous studies, which considered smaller tissues, have not been shown to feature such large-scale rotations. This may be

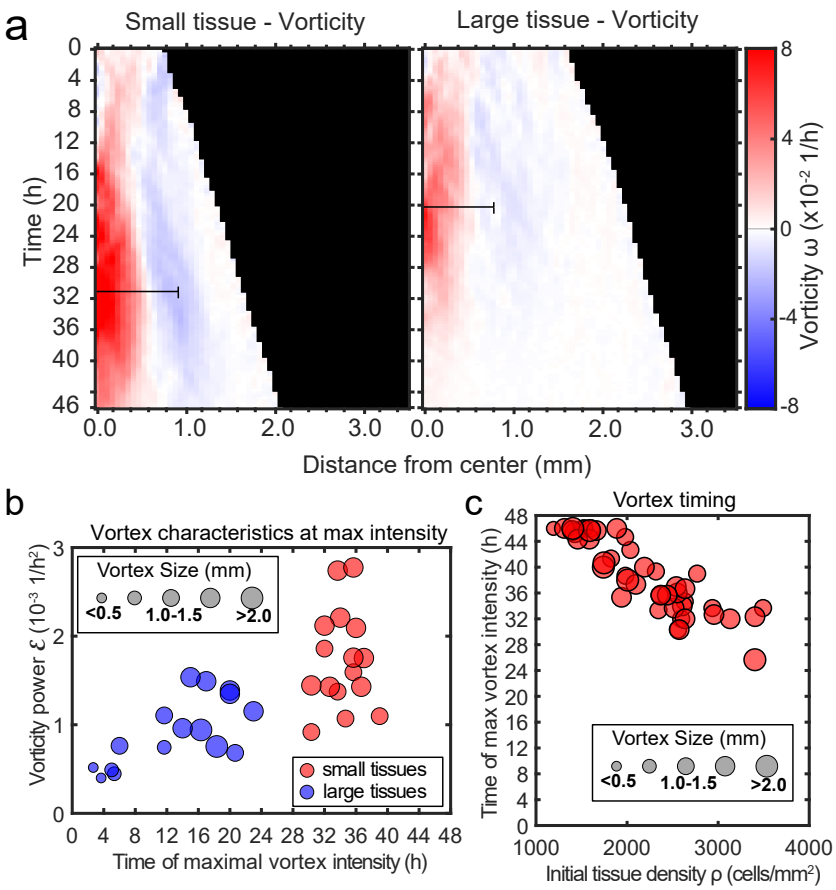

Figure 3.9: Vortex evolution. (a) Average kymographs of vorticity show that the vortex in small tissues appears in the center and expands to >1 mm (n = 16), while vorticity in large tissues is present only during the early stages of tissue expansion (n = 16). The black bars indicate a characteristic vortex size. (b) Characteristic vortex size (marker size), time (horizontal axis), and intensity (vertical axis) of each tissue's maximal vortex intensity. Small tissue vortices are generally more intense, with $p < 0.0001$ calculated using a two-tailed Mann-Whitney U test. (c) For small tissues, the time of maximal vortex intensity decreases with the initial cell density.

because they lie below the predicted critical size of the order of millimeters. Here, we do not consider tissues at sizes below this threshold, so further study is necessary to explicitly test this size-dependent prediction of the model.

3.3.4 Vortex kinematics

To quantify the kinematics of the large-scale vortical flows, we obtained the vorticity field $\omega(\mathbf{r}, \mathbf{t}) = \nabla \times \mathbf{v}(\mathbf{r}, \mathbf{t})$. Before averaging over tissues, we took the dominant

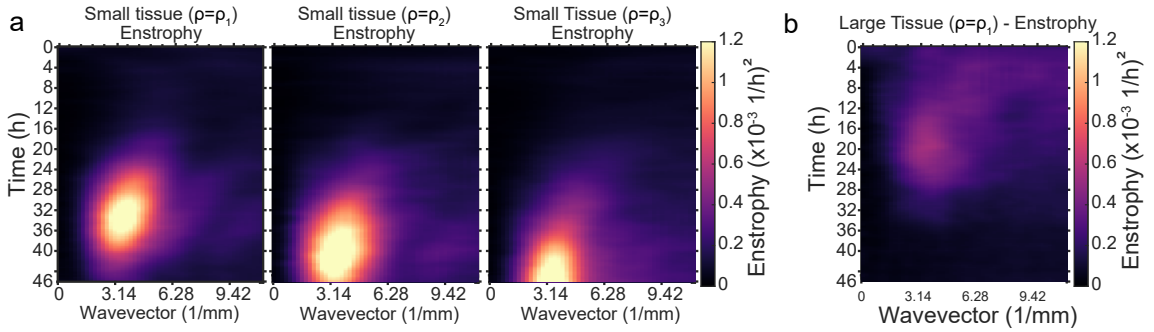

Figure 3.10: Vortex enstrophy. (a) From left to right, enstrophy kymographs of small tissues for decreasing starting density. $\rho_1 > \rho_2 > \rho_3$ ($2350 < \rho_1 < 3050$ cells/mm^2, $1650 < \rho_2 < 2350$ cells/mm^2, and $\rho_3 < 1650$ cells/mm^2). Decreasing starting density clearly delays the onset of high power, long wavelength (small wavevector) vorticity. Small tissue enstrophy peaks at a wavevector of ~ 3.14 mm^{-1}, which corresponds to a wavelength of 2 mm. Data from n=16 tissues for $\rho = \rho_1$ (left); n=13 tissues for $\rho = \rho_2$ (middle); and n=11 tissues for $\rho = \rho_3$ (right). (b) Average kymograph of enstrophy for large tissues ($\rho = \rho_1$). The peak at large wavelength is not evident since the vortex is not as prevalent in large tissues.

direction of rotation of each tissue to correspond to positive vorticity. This direction was counterclockwise in 51.5% of tissues and clockwise in 49.5% of tissues, with a sample size of 68. With this convention, the vortex core always has positive vorticity. Accordingly, the outer region of the vortex exhibits negative vorticity (Fig. 3.9a), which corresponds to the counter-rotation that occurs when the central vortical flow transitions to the outer radial flow (Fig. 3.8a, right). We define a characteristic vortex radius as the radial position of the center of the negative-vorticity region, which is $\sim$1 mm at 36 h in small tissues (Fig. 3.9a, black bars).

To analyze vortex dynamics across different tissues with varying vortex positioning, and to quantitatively capture the onset and strength of vortices, we calculated the enstrophy spectrum $\mathcal{E}(q,t) = |\tilde{\omega}(\mathbf{q},t)|^2$, where $\tilde{\omega}(\mathbf{q},t) = \int (d\mathbf{r}/A)\omega(\mathbf{r},t)e^{i\mathbf{q}\cdot\mathbf{r}}$ are the spatial Fourier components of the vorticity field $\omega(\mathbf{r},t)$ [181]. The enstrophy spectrum is the power spectral density of the vorticity field as a function of the wave-vector modulus q, and therefore provides a measure of the vortex intensity at a length scale

$2\pi/q$. The kymographs of the enstrophy spectrum show that most of the vortex's intensity is found at a characteristic length scale of $\sim 1-2$ mm (Fig. 3.10a).

For each tissue, we characterized the maximal vortex strength by the maximum value of $\mathcal{E}(q,t)$ as well as its associated wavelength $2\pi/q$ and time of occurrence. We represented these three quantities on a scatter plot, which shows that vortices in small tissues have generally higher intensity than those in large tissues (Fig. 3.9b, Fig. 3.10a,b). Vortices in small tissues are also larger relative to tissue size, since the absolute size of vortices in small and large tissues is similar (Fig. 3.9b). Furthermore, vortex strength peaks several hours later in small tissues than in large tissues (Fig. 3.9b). We hypothesized that this difference is due to large tissues featuring a faster density increase than small tissues (Fig. 3.3c). To test this hypothesis, we varied the initial cell density of small tissues and observed that the time of maximum vortex intensity decreases with increasing density (Fig. 3.9c, Fig. 3.10a). These results prompted us to examine spatiotemporal cell density evolution.

3.3.5 Spatiotemporal dynamics of cell density

Given that cell density appears to affect vortex formation and is known to control contact inhibition of locomotion and proliferation [182], we explored the spatiotemporal evolution of cell density. Strikingly, snapshots of small and large tissues reveal that large-scale vortices occur in low-density regions, regardless of location within the tissue (Fig. 3.11a-d). Moreover the highest vorticity magnitudes occur in low density regions in the center of tissues, even though the center of large tissues is predominantly high density, especially at 24 h and later (Fig. 3.11e,f). Constructing average kymographs in the same way as for speed, radial velocity, and vorticity, we observe that the vortex region in the center of small tissues is accompanied by an unexpected local density minimum from $\sim$ 12-36 h (Fig. 3.12a left). However, given that vortices

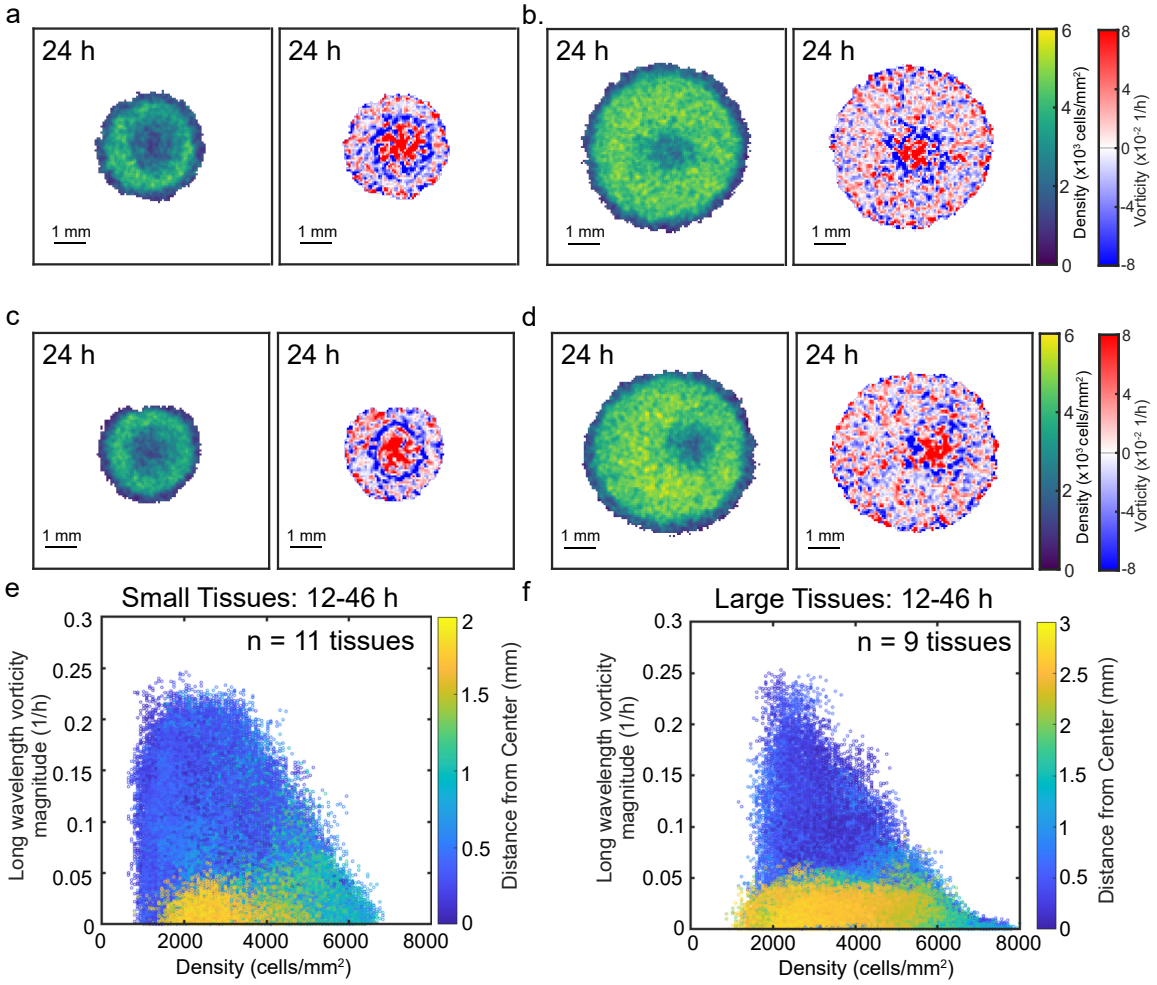

Figure 3.11: Large vorticies co-occur with regions of low density. (a-d) Regions of high vorticity (red) coincide with regions of low density, even when the large vorticies are off-center as in d. (e,f) Low-pass filtered vorticity magnitude vs. local density, colored as distance from the center in small (e) and large (f) tissues. To keep only mm-scale patterns, we applied a Fourier low-pass filter on vorticity fields, retaining only large-scale vorticity fluctuations (with wavelengths longer than 1 mm). We excluded the tissue edge region (500 μm from the boundary) that is outward polarized and does not exhibit vortical flows. Each point in panels (e) and (f) corresponds to a point in the filtered vorticity field, plotted against the cell density in that point.

in large tissues are often off-centered, the low-density region does not appear in their average kymograph of cell density (Fig. 3.12a right).

To investigate the effects of initial conditions, we tracked the density evolution of the center and boundary zones across tissues with different starting densities and sizes, grouping initial densities into 3 ranges as before (Fig. 3.12b and c). As with

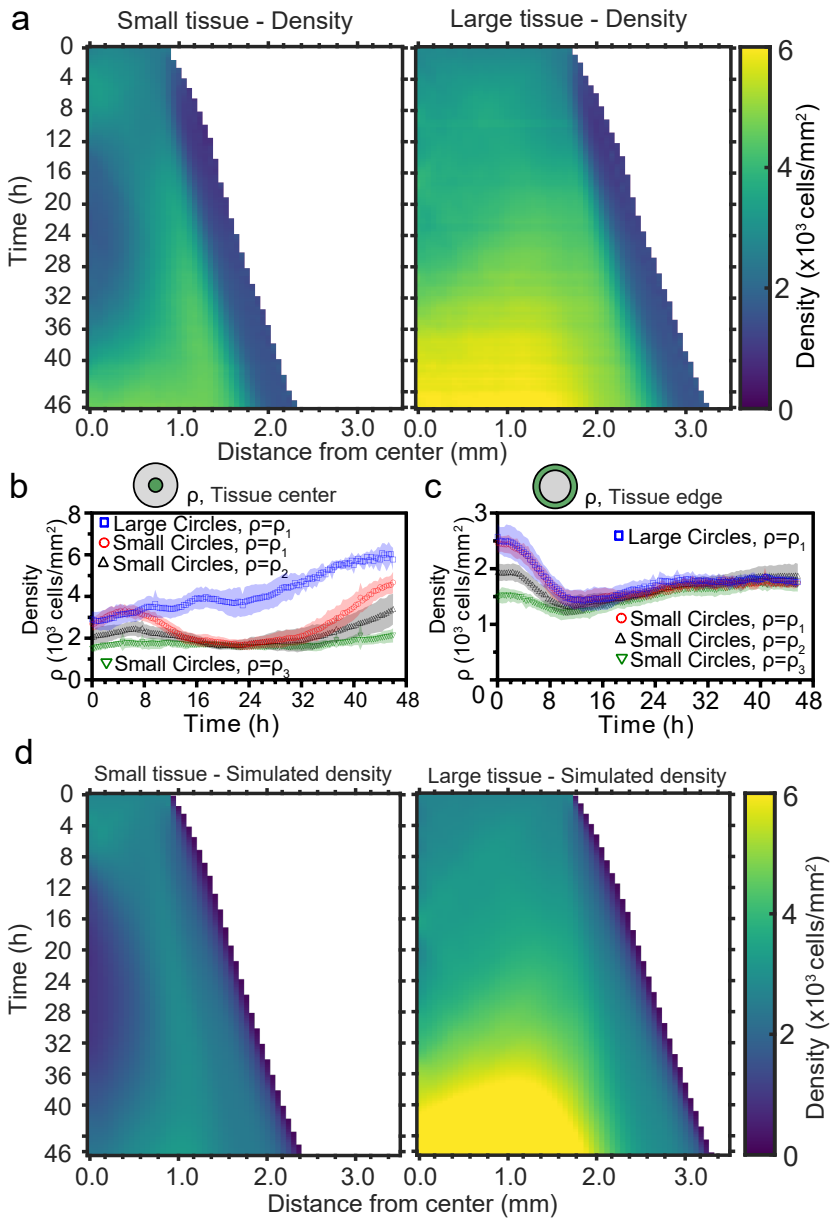

Figure 3.12: Spatiotemporal dynamics of cell density during epithelial expansion. (a) Averaged kymographs of cell density for small (left, n=11) and large (right, n=9) tissues. Small tissues develop a central low-density region that persists more than 20 h. (b-c) Cell density, ρ, in the center (b) and edge zone (c) of small and large circles of varying starting density. Center and boundary zones are defined as in Fig. 3.7b. (d) Simulated evolution of cell densities obtained from the numerical solution of the continuity equation using the average radial velocity measurements $v_r(r,t)$ (Fig. 3.7b) and a uniform and constant cell proliferation rate corresponding to a 16 h cell doubling time.

the average density in Fig. 3.3c, the density monotonically increases in large tissues centers but is non-monotonic in small tissues. Notably, the cell density at the center of small tissues of different initial cell densities reach a common minimum during the 16-32 h time period (Fig. 3.12b), which includes the vortex onset time. At the boundary zone, the long-time evolution of the cell density is independent of initial tissue size and density (Fig. 3.12c). This common long-time evolution is reached at about 12 hours (Fig. 3.12c), which coincides with the time at which the edge radial velocity stabilizes upon the overshoot (Fig. 3.3d).

To understand the unexpected transient density decrease at the center of small tissues, we sought to explain it as the result of combined advective transport based on the measured radial flow fields $\mathbf{v}_r(\mathbf{r}, t)$ and homogeneous cell proliferation at a rate $k(\mathbf{r}, t) = k_0$ throughout the tissue. To test this hypothesis, we solved the continuity equation for the cell density field $\rho(\mathbf{r}, t)$,

$$\frac{\partial \rho}{\partial t} = -\nabla \cdot (\rho \mathbf{v}) + k_0 \rho, \tag{3.3.4}$$

using the average radial velocity profiles $v_r(r, t)$ measured by PIV (Fig. 3.7d), and a proliferation rate $k_0 = 1.04$ h^{-1}, which corresponds to a cell doubling time of 16 h (Materials and Methods). This minimal model recapitulates the major features of the evolving density profiles for both small and large tissues (compare Fig. 3.12d with Fig. 3.12a). Therefore, the unexpected formation of a central low-density region results from the combination of outward tissue flow and proliferation within the colony. However, further research is required to determine the biophysical origin of the non-monotonic density evolution. Moreover, having assumed a density-independent proliferation rate, our model predicts a cell density in the center of large tissues higher than the one measured at the end of the experiment, and it does not quantitatively reproduce the cell density profiles at the edge regions. These discrepancies suggest

that more complex cell proliferation behavior is required to fully recapitulate the density dynamics in expanding cell monolayers.

3.3.6 Spatiotemporal dynamics of cell cycle

To better understand how tissue expansion affects cell proliferation, we analyzed the spatiotemporal dynamics of cell-cycle state. Our cells stably express the FUCCI markers, meaning that cells in the G0-G1-S phase of the cell cycle (referred to here as G1) fluoresce in red (shown as magenta), and cells in the S-G2-M phase of the cell cycle (referred to here as G2) fluoresce in green [159]. Additionally, immediately-post-mitotic cells do not fluoresce and appear dark. Small and large tissues are initially well mixed with green and magenta cells, confirming that cells are actively cycling throughout the tissue at the time of stencil removal (see Materials and Methods, Fig. 3.1). During tissue expansion, spatiotemporal patterns of cell-cycling behavior emerge (Fig. 3.13a, Supplementary Video 2).

To quantitatively investigate these cell-cycle patterns, we obtained the local fractions of G1, G2, and post-mitotic cells by evaluating cell cycle state for each cell nucleus (see Materials and Methods). We then overlaid kymographs of the G1 and G2 cell-cycle-state fractions (Fig. 3.13b) and plotted the time evolution of G1, G2, and post-mitotic fractions together (Fig. 3.13c,d). Immediately after stencil removal, we observe a cell division pulse in all tissues, which manifests in a decrease in G2 and increase in post-mitotic fraction (Fig. 3.13c,d). After about 12 h of tissue expansion, the boundary region becomes primarily populated by rapidly-cycling cells (Fig. 3.13b, c), which results in a predominance of cells in this region that either have recently divided (post-mitotic, black) or are likely to divide soon (G2, green). The high numbers of post-mitotic cells indicate that cells in G1 rapidly proceed to mitosis. Given that the edge radial speed overshoots during the first 12h of tissue expansion

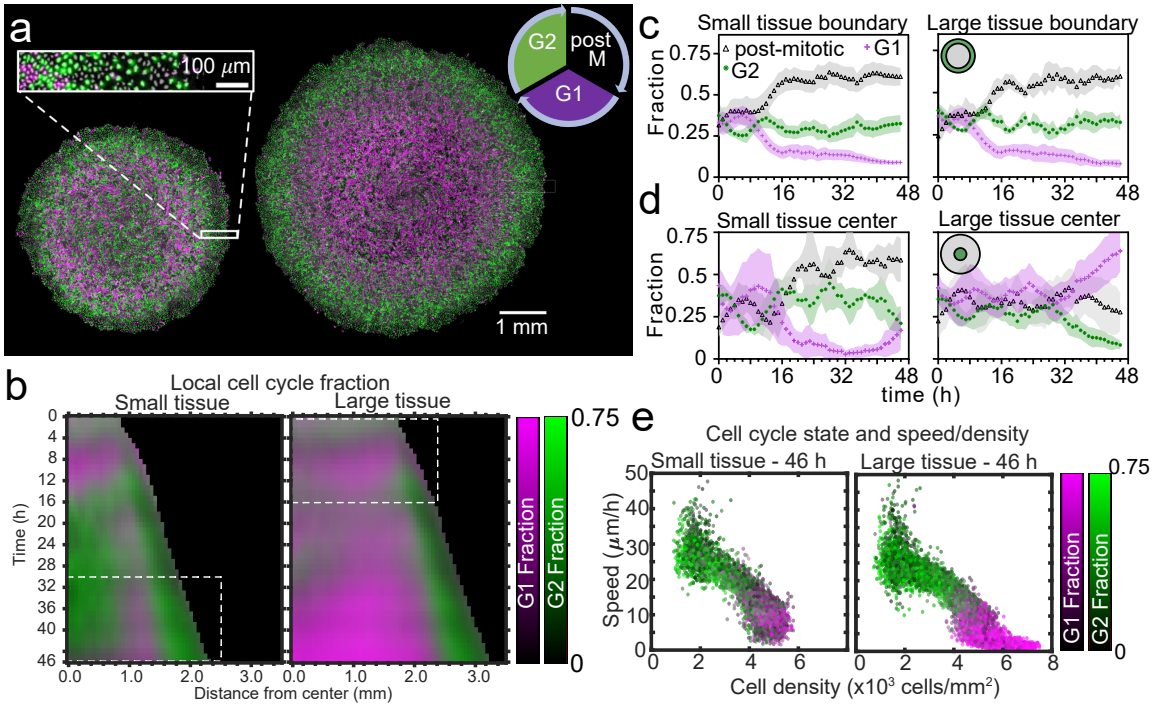

Figure 3.13: Coordinated spatiotemporal cell-cycle dynamics. Transition from the G1 (magenta) to the G2 (green) phase of the cell cycle corresponds to DNA replication (during S phase). Subsequently, a cell proceeds to mitosis (M phase, dark), and eventually back to the G1 phase upon cell division. (a) Fluorescence images of the Fucci marker of cell-cycle state at the end of the experiment (46 h) of representative small and large tissues overlaid with nuclei positions (gray). The boundary zone of both tissues has more cells in the G2 than in the G1 phase, along with a substantial proportion of dark cells (inset). (b) Average kymographs (small, n=5; large, n=11) of cell-cycle-state fraction. In small tissues, a G1-dominated transition zone, which appears as a vertical magenta streak from 16 h onward, is interposed between G2-dominated center and edge zones. While the size of small tissues from 30 to 46 h matches that of large tissues from 0 to 16 h (dashed boxes), cell-cycle states between these times are clearly distinct. (c) Fraction of cell-cycle states in the boundary zone. (d) Fraction of cell-cycle states in the center zone. Center and boundary zones are defined as in Fig. 3.7. (e) Scatter plot of density and speed, with color indicating the fraction of cells at G1 and G2, corresponding to each PIV pixel of the final timepoint of a representative small (left) and large (right) tissue.

(Fig. 3.3d), future work is necessary to characterize the effect of cell cycling on edge motion at early stages of expansion.

In the central region of small tissues (Fig. 3.13b left, d left), we observe cell-cycling dynamics similar to the boundary region. Thus, in the tissue-spanning vortex

of small tissues, cells are also rapidly cycling. The fraction of cells in G1 only starts to increase at ∼40 h (Fig. 3.13d left), coinciding with the weakening of the vortex (Fig. 3.9a left). In contrast, the center zone of large tissues undergoes strong cell-cycle arrest at the G1-G2 transition at about 30 h (Fig. 3.13b right, d right), but this also coincides with the weakening of the vortex in large tissues (Fig. 3.9a right). Cells already past G1 at this time continue to division and re-enter G1, evidenced by the steady increase in local fraction of G1 accompanied by a steady decrease in G2 after 30 h. Similar cell-cycle arrests were previously reported both in growing epithelia [21] and in spreading 3D cell aggregates [154]. Before the onset of cell-cycle arrest, the center of large tissues exhibits large-scale coordinated cell-cycling dynamics in the form of anti-phase oscillations, with peaks in G2 fraction accompanied by troughs in G1 fraction (Fig. 3.13b right, d right).

Finally, we sought to link cell-cycle dynamics to the kinematics of tissue expansion by studying correlations between local measurements of cell cycle, cell speed, and cell density (Fig. 3.13e). Here, each point represents one PIV window, with color indicating its average cell-cycle state. As expected, cell speed is negatively correlated with cell density. Further, in large tissues, the cell-cycle state transitions from G1-dominated to G2-dominated when cell density increases above ∼5000 cells/mm^2 and cell speed falls below ∼12 μm/h (Fig. 3.13e right). In this regime, the decrease of cell speed with increasing cell density bears similarities to previously-reported glass transitions and contact inhibition of locomotion [85, 88, 183]. Small tissues, by contrast, lack the G1-dominated, slow, high-density cell population (Fig. 3.13e, left) found in the center of large tissues. Taken together, our findings emphasize that cell cycling, cell flow, and cell density patterns are inextricably linked and depend on the initial size of an expanding tissue.

3.4 Discussion

We began this study by asking how changes in initial size affect the long-term expansion and growth of millimeter-scale epithelia. By means of high spatiotemporal resolution imaging and precisely controlled initial conditions, our assays systematically dissected tissue expansion and growth from the overall boundary kinematics (Fig. 3.3) to the internal flow patterns (Figs. 3.7, 3.8, 3.12) and cell-cycle dynamics (Fig. 3.13). While we demonstrated that 'small' tissues increase in area relatively much faster than do 'large' tissues, our data suggest a surprising and stark decoupling of the outer and inner regions of an expanding epithelium. Notably, the behaviors of the edge zones are largely independent of tissue size, cell density, and history, while interior dynamics depend strongly on these factors.

Unexpectedly, the overall tissue growth and expansion dynamics (Fig. 3.3) could be attributed to one dominant feature: these epithelia expanded at the same edge speed regardless of initial tissue size, shape, and cell density. The only exception is the major axes of ellipses, where the normal edge speed is smaller when the radius of curvature is $r_c < 0.75$ mm. This observation, combined with the fact that the velocity penetration length is $\gtrsim 500$ mm (Fig. 3.7d), suggests that a tissue must be $\gtrsim 1$ mm in diameter for the tissue edge to move independently of bulk flows. As a result of this robust edge motion, the areal expansion rate of the tissue is dictated by its perimeter-to-area ratio. To further emphasize the decoupling of the boundary and internal dynamics of epithelia, consider that the key findings in Fig. 3.3 neither predict nor depend upon the radically different internal dynamics we observed within 'small' and 'large' tissues. For instance, despite the roiling vortices occupying large portions of 'small' tissues and the pronounced, large-scale contact inhibition of 'large' tissues–two antithetical phenomena–no hints of these behaviors can be detected in the motion of the boundary.

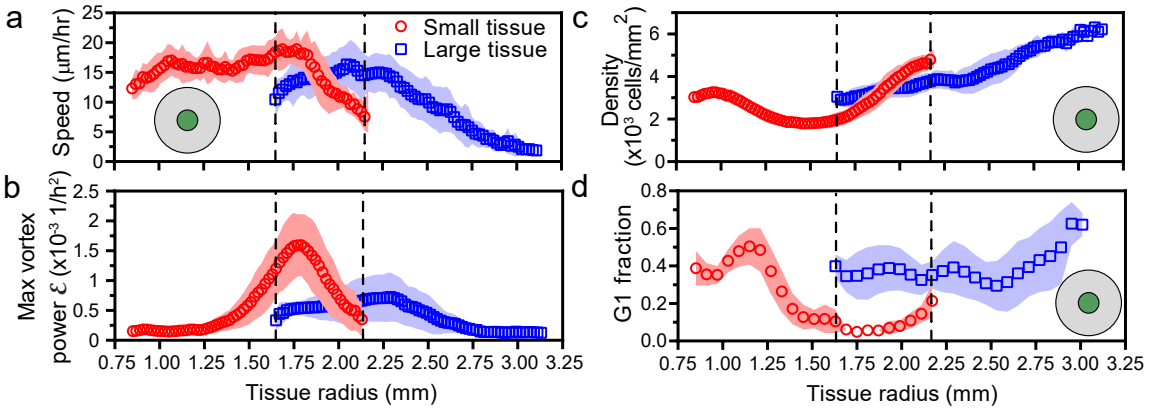

Figure 3.14: Initial tissue size, rather than current tissue size, determines the internal dynamics of expanding epithelia. Here, we quantify the internal state of the tissue in terms of the cell speed in tissue center (a), maximal vortex power (b), cell density in tissue center (c), and fraction of cells in the G1 phase of the cell cycle in tissue center (d). At late times, initially-small tissues reach radii that initially-large tissues had at early times. When they have the same current size (overlap region in between dashed lines), initially-small and initially-large tissues have distinct internal dynamics of cell migration and cell proliferation. The tissue center zone in a, c, and d was defined as in Fig. 3.7.

Critically, the type and timing of internal dynamics are dictated not by the current size but by the expansion history of a given tissue. While a small tissue eventually expands to reach the initial size of a large tissue, it exhibits different internal dynamics from the large tissue at this size (Fig. 3.14). This difference in internal dynamics is perhaps easiest to observe in spatiotemporal evolution of cell cycle (Fig. 3.14d, Fig. 3.13b dashed boxes); the small-tissue footprint from 30-46 h closely matches the large-tissue footprint from 0-16 h, but the cell cycle distribution during these time periods bears almost no similarities. This applies as well to other important bulk properties of the tissue (Fig. 3.14a-c), as cell cycle is tightly linked to cell speeds and density (Fig. 3.13e). For example, at equal current sizes, the center of initially-small tissues features high vorticity with decreasing cell speed whereas initially-large tissues exhibit low vorticity and increasing cell speed (Fig. 3.14a,b). Respectively, at equal current sizes, while absolute cell densities in the tissue centers share some overlap, it is notable that the rate of density change at the tissue center is increasing

faster in initially-small tissues than in initially-large tissues (Fig. 3.14c). However, the most striking differences in cell density evolution occur not at equal current sizes but during the early stages of tissue expansion: whereas the cell density at the center of large tissues increases at all times, the center of small tissues features a marked density decrease between ~ 8 and ~ 24 h (Fig. 3.12a,b). Overall, while edge dynamics are stereotyped and conserved across different sizes, our findings suggest that initial tissue size impacts the bulk dynamics by altering the constraints under which the tissue grows. We expect that tissues with sizes between our two choices would exhibit similar edge dynamics and internal patterns that cross over between our small and large tissues.

The vortices are a particularly striking example of such size- and history-dependent internal patterns (Fig. 3.8, Fig. 3.14b). Our active fluid model suggests that the vortices emerge from a dynamical instability of the tissue bulk, which occurs when the tissue reaches a critical size. Thus, whereas the instability itself is a bulk phenomenon independent of the tissue edge, edge-driven expansion allows small tissues to reach the critical size that triggers the instability. In addition, our data suggest a strong correlation between vortex formation and the development of non-monotonic density profiles. Not only did small tissues exhibit co-occurrence of vortices with density decreases in the tissue center, but also off-center vortices in large tissues always co-localized with a local density decrease (Fig. 3.11). Our model does not currently describe cell density, and hence cannot explain the relationship between vortex formation and local density decreases. Thus, our experimental findings call for the development of more detailed models that couple cell density to both the velocity and the polarity fields, accounting for how density gradients influence cell polarization [138].

The pronounced decoupling between boundary and internal dynamics in epithelia confers stability to the overall expansion of the tissue, making it robust to a wide

range of internal perturbations. From the perspective of collective behavior, we speculate that such robust boundary dynamics may be beneficial in a tissue such as an epithelium whose teleology is to continuously expand from its free edges to sheath organ surfaces. Further, the ability to accurately predict epithelial expansion with a single parameter, the edge speed, will have practical uses in experimental design and tissue-engineering applications. Finally, given that many of the phenomena presented here only occurred due to the millimetric scale of our unconfined tissues and the long duration of the experiments, our results showcase the value of pushing the boundaries of large-scale, long-term studies on freely-expanding tissues.

Chapter 4

Epithelial collision and tissue-tissue interactions

4.1 Introduction

As we saw in the previous chapter, cell-cell interactions and cell behavior strongly depends on a cell's location in the tissue, and these cell-cell interactions can give rise to collective motions on the scale of thousands of cells. In this chapter, we proceed up a level to tissue-tissue interactions, which occur when two or more communities of cells come into contact.

In places where tissues meet, the resulting tissue is a living composite material whose properties depend on its constituent tissues. In particular, tissue-tissue interfaces underlie both biological processes such as organ separation and compartmentalization [184, 185], as well as biomedical applications such as tissue-mimetic materials [137, 186, 187] and engineered tissue constructs [188–190]. Thus, recent research has focused on the formation and dynamics of tissue-tissue boundaries. For instance, the interplay between repulsive Eph/ephrin and adhesive cadherin cell-cell interactions regulate tissue boundary roughness, stability, and cell fate [191–195]. Furthermore,

colliding monolayers with differences in Ras gene expression were able to displace one another [196, 197], while epithelial tissue boundaries were found to induce waves of cell deformation and traction long after the tissues had collided [41].

Our goal in this chapter was to harness these fundamental concepts to define broad 'design principles' for assembling composite tissues in a controlled way. Specifically, we sought to harness mechanical tissue behaviors in the context of cell-sheet engineering, which aims at harvesting intact cell monolayers to create scaffold-free, high-density tissues [189]. Such cell sheets are typically produced by allowing cells to come to confluence within a stencil or patterned substrate to form a monolayer with a desired geometry [198, 199]. Here, we propose an alternative approach where we create arrays of individual epithelial monolayers and then allow them to grow out and collide, fuse at the interfaces, and ultimately self-assemble into tessellated patterns.

We performed live imaging as these tissue arrays self-assembled into patterns over 2-3 days, which we predicted by extending our earlier model of tissue expansion (introduced in Chapter 3) to account for multi-tissue interactions. We then characterized the dynamics of the boundary in collisions of tissues with different size, cell density, and composition. Moreover, we proposed a physical model for understanding the resulting boundary motion and extracting tissue mechanical properties from it. We next introduced a design framework for the systematic assembly of many-tissue composites (3 cell types and 30+ tissues), and finally investigated more complex cases such as tissue engulfment and the singular dynamics of tri-tissue junctions.

4.2 Materials and Methods

4.2.1 Cell culture

MDCK.2 wild type canine kidney epithelial cells (ATCC) were cultured in customized media consisting of low-glucose (1 g/L) DMEM with phenol red (Gibco, USA), 1 g/L

sodium bicarbonate, 1% streptomycin/penicillin (Gibco, USA), and 10% fetal bovine serum (Atlanta Biological, USA). MCF10A human mammary epithelial cells (ATCC) were cultured in 1:1 DMEM/F-12 (Thermo Fisher Scientific, USA) media which consists of 2.50 mM L-Glutamine and 15 mM HEPES buffer. This media was supplemented with 5% horse serum (Gibco, New Zealand origin), 20 ng/mL human EGF (Sigma, USA), 0.5 µg/mL hydrocortisone (Fisher Scientific), 100 ng/mL cholera toxin (Sigma), 10 µg/mL insulin (Sigma, USA), and 1% penicillin/streptomycin (Gibco, USA). MDA-MB-231 (ATCC) and MCF7 (ATCC) human mammary cancer cells were both cultured in 1:1 DMEM/F-12 (Thermo Fisher Scientific, USA) media supplemented with 10% fetal bovine serum (Atlanta Biological, USA) and 1% penicillin/streptomycin (Gibco, USA). All cells were maintained at 37°C and 5% CO_2 in humidified air.

4.2.2 Tissue patterning and labeling

Experiments were performed on tissue-culture plastic dishes (BD Falcon, USA) coated with type-IV collagen (MilliporeSigma, USA). Dishes were coated by incubating 120 μL of 50 μg/mL collagen on the dish under a glass coverslip for 30 minutes at 37°C, washing 3 times with deionized distilled water (DI), and allowing the dish to air-dry. Stencils were cut from 250 μm thick silicone (Bisco HT-6240, Stockwell Elastomers) using a Silhouette Cameo vinyl cutter (Silhouette, USA) and transferred to the collagen coated surface of the dishes. Cells were separately labelled using CellBrite^{TM} (Biotium, USA) Red and Orange dyes for two-color experiments and CellBrite^{TM} (Biotium, USA) Red, Orange, and Green dyes for three-color experiments.

For MDCK experiments, suspended cells were concentrated at $\sim 2.25 \times 10^6$ cells/mL and separated according to eventual labelling color. We added 8 μL of the appropriate membrane dye per 1mL of media and briefly vortexed each cell suspension.

Then, we immediatedly pipetted into the stencils at ∼1000 cells/mm^2, taking care not to disturb the collagen coating with the pipette tip. To allow attachment of cells to the collagen matrix and labelling of the cell membranes, we incubated the cells in the stencils for 30 minutes in a humidified chamber before washing out the dye and filling the dish with media.

For experiments using other cell types, suspended cells were concentrated at $\sim 3\times 10^6$ cells/mL and 10μL of membrane dye per 1 mL of media. We briefly vortexed the cell suspension and allowed it to incubate for 20 minutes at 37°C. We then centrifuged the suspension and removed the supernatant, replacing it with the appropriate media without dye. We pipetted into the stencils at the same volume as before (greater number of cells), and incubated the cells in the stencils for 2-3 h to allow attachment before filling the dish with media.

For all experiments, we then incubated the cells for an additional 18 h after cell attachment to form confluent monolayers in the stencils. Stencils were removed with tweezers, with imaging beginning $\sim$ 30 minutes thereafter. Media without phenol red was used throughout seeding and imaging for three-color experiments to reduce background signal during fluorescence imaging.

4.2.3 Live-cell time-lapse imaging

We performed imaging on an automated, inverted Nikon Ti2 with a Nikon Qi2 CMOS camera and NIS Elements software. We equipped the microscope with environmental control for imaging at 37°C and humidified 5% CO_2. Final images were composited in NIS Elements from montages of each pair or tessellation.

For experiments from Fig. 4.9c-j, we used a 10X phase contrast objective to capture phase-contrast and fluorescence images every 10 minutes. RFP/Cy5 images were captured at 10% lamp power (Sola SE, Lumencor, USA) and 150 ms exposure time. No phototoxicity was observed under these conditions for up to 24 h.

For all other experiments, we used a 4X phase contrast objective to capture phase-contrast images every 20 minutes. For two color time-lapse images, RFP/Cy5 images were also captured every 20 minutes at 15% lamp power (Sola SE, Lumencor, USA) and 500 ms exposure time. For three color time-lapse images, RFP/Cy5 images were captured every 60 minutes at 15% lamp power (Sola SE, Lumencor, USA) and 300 ms exposure time, while GFP images were captured every 120 minutes at 15% lamp power (Sola SE, Lumencor, USA) and 300 ms exposure time. No phototoxicity was observed under these conditions for up to 72 h. Final images were composited in NIS Elements from montages of each pair or tessellation.

4.2.4 Tissue dye segmentation

The tissue dye becomes diluted as cells divide and spread, so the dye at tissue edges (where cells are more spread and divide more frequently) becomes much more dim than the center of tissues. To aid visualization, and because we saw no mixing in our collisions, we segmented the fluorescence channels using a custom MATLAB (Mathworks) script and overlaid them with the phase contrast images. To segment fluorescence images, we normalized the fluorescence channel histograms to each other and compared relative brightness for each pixel between channels. We then masked with the binary masks obtained from the phase contrast channel.

4.2.5 Model of expansion and collision of homotypic tissues

Based on our previous work [23], we modeled the expansion of monolayers of arbitrary shape by moving its boundary with constant outward normal velocity v_n. Here, we worked with pixelated binary images of initial tissue footprints I_{t_0} at time t_0 (Fig. 4.1), which enabled us to take advantage of standard image processing tools in Matlab. The goal is to find the expected tissue image footprints $I_{t_0+\Delta t}$ at any later time $t_0+\Delta t$. For each tissue, we first used the bwdist method to calculate the distance map D, which

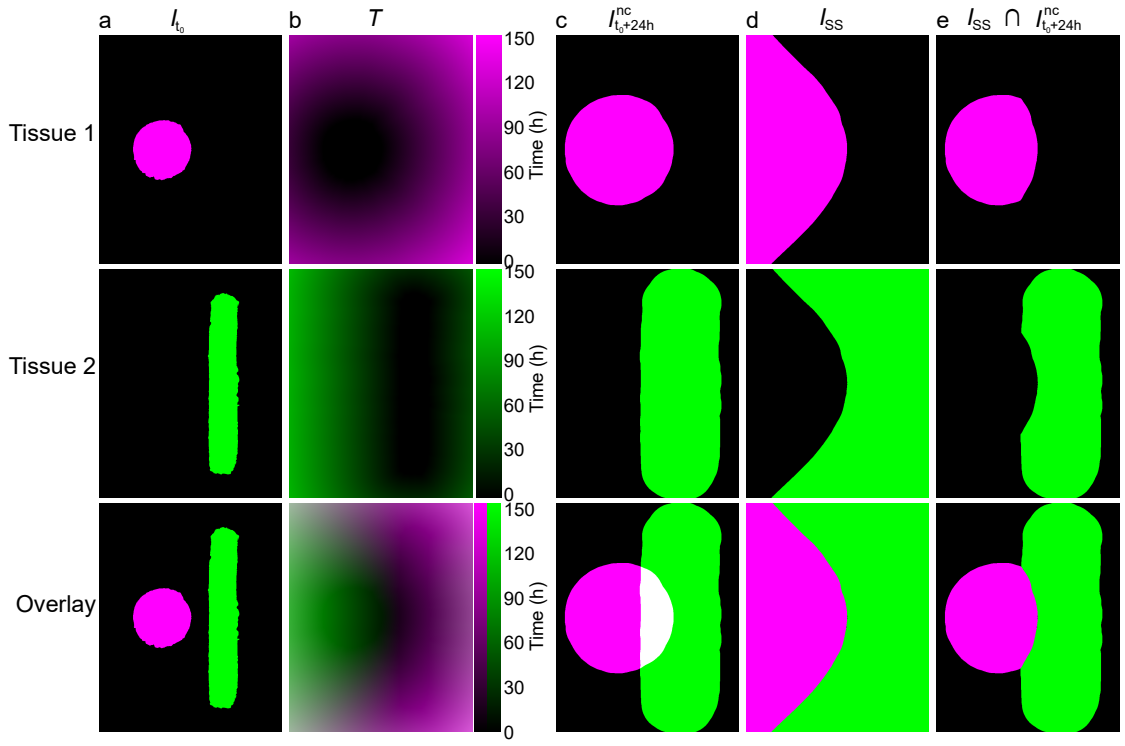

Figure 4.1: Phenomenological model of collisions. (a) Binary image of Initial tissue footprints I_{t_0}. (b) Heatmap of time that would elapse for initial tissues to fill pixels within image (T). (c) Binary image of predicted tissue footprints after 24 h of growth, without non-mixing collision $I^{nc}_{t_0+24h}$. (d) Steady state forms of tissue footprints I_{SS}, with non-mixing collisions that pin in place on contact. I_{SS} for tissue 1 is found as $T_{Tissue1} < T_{Tissue2}$. (e) Binary image of predicted tissue footprints after 24 h of growth, with non-mixing collision.

shows the shortest distance between a given pixel and the initial tissue. This distance map is then used to calculate the time map $T = D \times l_{pixel}/v_n$ at which a tissue reaches every pixel (Fig. 4.1b), where l_{pixel} is the pixel size. In the absence of collisions with other tissues, we can then find the new tissue footprint $I^{nc}_{t_0+\Delta t}$ simply as all pixels for which $I_{time} < \Delta t$. (Fig. 4.1c). For multiple expanding tissues, we assumed that the boundary gets pinned upon collision. After a long time (steady state) each tissue thus occupies all the pixels that it manages to reach before any other tissue. The steady state tissue form I_{SS} of a given tissue thus contains all pixels for which the value of T is the minimum across all tissues (Fig. 4.1d). Note that for the homotypic tissues that expand with equal outward speed v_n, the steady state tissue form I_{SS}

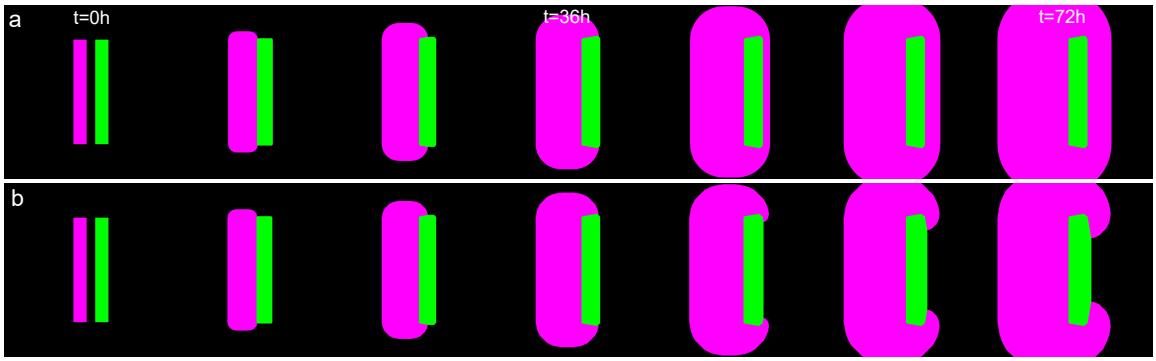

Figure 4.2: Model considerations for edge speed differences and envelopment. (a) Time course of envelopment for basic model, where faster tissue (magenta, 40 μm/h) unphysically grows "through" the slower tissue (green, 7 μm/h). (b) Re-setting initial tissue locations to current tissue locations periodically (here, every 6 h) prevents unphysical envelopment. Images shown once every 12 h.

corresponds to the pixels that are the closest to a given tissue, in a finite-size analog of the classic Voronoi tessellation. The time evolution of each tissue image $I_{t_0+\Delta t}$ can then be obtained as the intersection between the tissue footprint without collisions $I^{nc}_{t_0+\Delta t}$ and the steady state tissue form I_{SS}, i.e., $I_{t_0+\Delta t} = I^{nc}_{t_0+\Delta t} \cap I_{SS}$ (Fig. 4.1e).

4.2.6 Model extension for heterotypic tissues

The model described above has to be slightly adjusted for the heterotypic tissues that expand with different outward velocities. The problem is that the model above predicts that a faster expanding tissue migrates "through" a slower expanding tissue to reach distant points (Fig. 4.2a). To correct for this issue, we repeatedly calculate the distance map D with respect to the current tissue forms (rather than initial forms) for all tissues at a time interval chosen to be sufficiently small such that the faster tissue cannot migrate through the slower tissue. If this interval produces artifacts of the square lattice in the slower tissue, a smaller pixel size may be chosen at the expense of processing time. The rest of the steps are identical as in the model described above. This slight modification of the model is sufficient to properly capture how faster expanding tissues envelop slower ones (Fig. 4.2b).

4.2.7 Setting v_n for model

We set the normal velocity for the model (all shapes and tessellations) according to the outward velocity of outer edges of the control rectangle collisions. The outward velocity was found to be 29.4 $\pm$ 2.3 μm/h (standard deviation), so we used the previously reported speed for expanding circles of 29.5 μm/h [23].

4.2.8 Velocity measurements

We calculated tissue velocity vector fields from phase contrast image sequences, rotating each image so that the initial tissue locations in image pairs were horizontal. We used the free MATLAB package PIVLab with the FFT window deformation algorithm, employing a 1st pass window size of 96×96 pixels and second pass of 48×48 pixels, with 50% pixel overlaps. This resulted in a final window size of 88×88 μm. Data was smoothed in time with a moving average of 3 time points centered at each timepoint.

4.2.9 Average kymographs

We first constructed kymographs of each rectangular collision pair, averaging over the vertical direction of each timepoint and ignoring the top and bottom 1 mm. We then averaged the individual tissue kymographs, aligning by the initial tissue configuration, and determined the edge extent from the median extent of the individual kymographs.

4.2.10 Cell density measurements

We first reproduced nuclei positions from 4X phase contrast images using our in-house Fluorescence Reconstruction Microscopy tool [156]. The output of this neural network was then segmented in ImageJ to determine nuclei footprints and centroids.

Local density was calculated for each PIV window by counting the number of nucleus centroids in that window.

4.2.11 Cell sheet engineering tissue patterning and transfer

We first patterned tissues on 3.5 cm NUNC^{TM} UpCell^{TM} dish with supportive membrane (ThermoFisher Scientific, USA). We followed the same collagen coating and stencil application process as before, but passivated the underside of our stencils to avoid damaging the UpCell^{TM} surface. To passivate the stencils, we incubated them for 30 min at 37°C in Pluronic^{TM} F-127 solution (ThermoFisher Scientific, USA) diluted in PBS to 2%. We washed the stencils three times in DI and gently dried them with compressed air before transferring to the dish.

After the tissues reached confluence within the stencils, we removed the stencils and allowed the tessellation to collide and heal for ∼72 h. To release the tessellation monolayer from the dish, we changed to cold media and moved the dish to an incubator set to 25°C for 1.5 h. We then pre-soaked the supportive membrane in media to avoiding membrane folding, and floated the membranes on the media above the tessellations. We then carefully aspirated the media from beside the membranes to ensure tight contact between the membrane and monolayer with no bubbles. We moved the UpCell^{TM} dish with membrane to a 4°C refrigerator to ensure total release, and prepared a standard 3.5mm tissue culture dish (BD Falcon, USA) coated with collagen IV as before and filled with warm media. After 7 minutes at 4°C, we then carefully removed the membrane and tessellation monolayer from the UpCell^{TM} dish and floated it in the tissue culture dish with the tessellation side down. We aspirated the media from beside the membrane to initiate bubble-free contact with the dish surface and covered the membrane with 350 μL of warm media. We incubated the membranes at 37°C overnight before floating the membrane off the surface by filling the dish with media and removing it with tweezers.

4.3 Results

4.3.1 Collisions between archetypal tissue pairs.

We first characterized interactions between growing pairs of millimeter-scale epithelial tissues, including equal-size rectangles, circles, small vs. large circles, and circles vs. rectangles (Fig. 4.3, Supplementary Video 3). We used MDCK cells, a standard model [5, 20], and labeled each tissue in a pair with a different color (Materials and Methods) to clearly distinguish the boundary. Imaging over 2-3 days, we observed no mixing, because cells do not commonly rearrange in most epithelial tissues with desmosomes [57].

Collisions between identical rectangular tissues are well characterized from the traditional wound healing scratch and barrier removal assays [5, 41], and our data here confirmed the expected symmetric collision and fusion along the midline (Fig. 4.3a). We next compared identical circles, where we observed a straight boundary form at the midline as before (Fig. 4.3b), but it was almost two times smoother than the boundary between colliding rectangles (Fig. 4.4a, p value 0.014, see Methods). We suspect that this is due to the difference in collision dynamics: while parallel strips of tissue collide all along the collision line at once, circles collide at a single point and gradually extend the boundary line outward.

We introduced asymmetry by replacing one of these circles with either a much larger circle, or a long, thin rectangle (Fig. 4.3c,d). In each case, we observed a curving of the boundary away from the larger tissue, which was especially notable in the circle-rectangle collisions. We aligned and averaged the final segmented fluorescence signals to demonstrate how stereotyped these collision patterns are (Fig. 4.3, rightmost column).

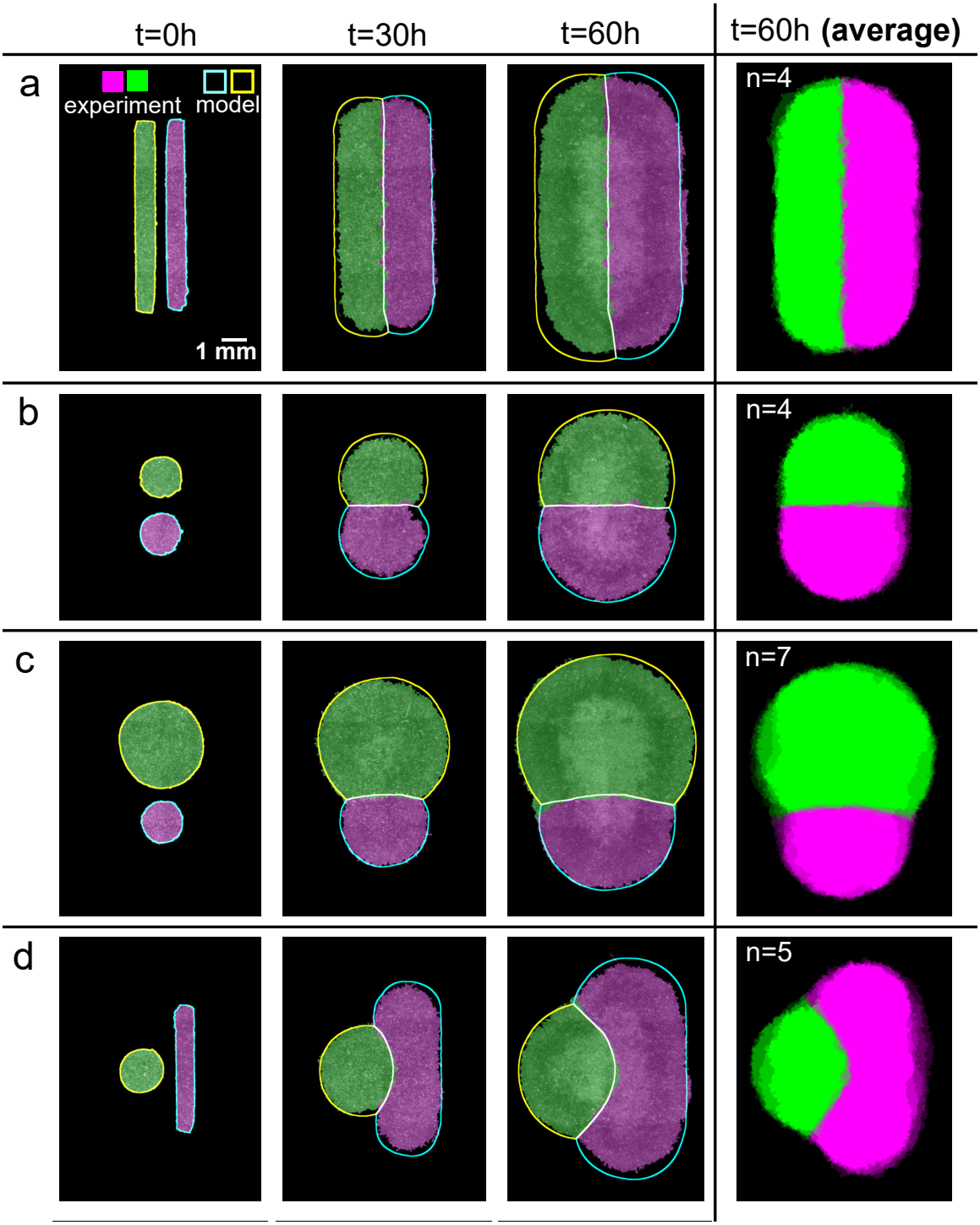

Figure 4.3: The shape changes of colliding tissue pairs are stereotyped and predictable. Archetypal collision experiments (solid) and simulations (outline) for equally-sized rectangles (a), equally-sized circles (b), mismatched circles (c), and circle-rectangle pairs (d). Averages over several tissues at 60 h are shown in the rightmost panels (n = 4-7). See Supplementary Video 3.

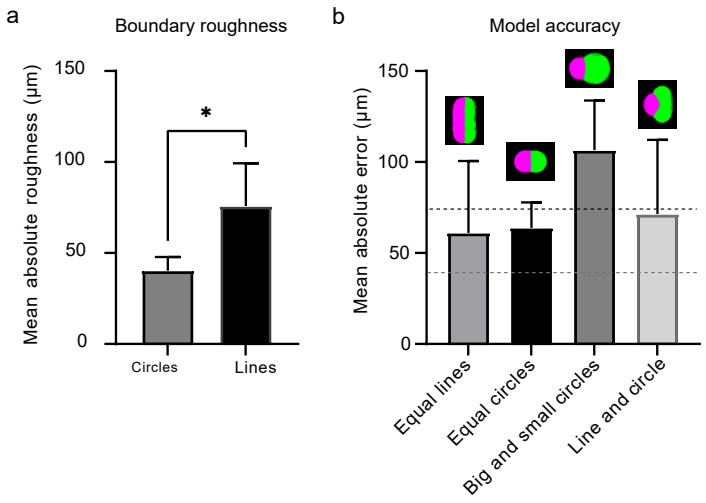

Figure 4.4: Boundary roughness and model accuracy. (a) The collision boundary that forms between circles is smoother than the boundary between parallel rectangles. Roughness was quantified as the mean absolute error of 2mm line fit to the steady state interface. P value < 0.05, error bars are standard deviation. (b) Error of model is compatible with the boundary roughness. Error was found as the mean distance from the actual boundary to the boundary in model. Black and gray dotted lines are the roughness of the boundary line between colliding rectangles and circles, respectively. Error bars are standard deviation.

4.3.2 Predicting the shape of colliding tissues

The stereotyped nature of these collision patterns suggested value in a computational design tool to predict the evolution of tissue shapes upon collisions. We previously established that freely-growing epithelia expand outward with a normal velocity v_n, which, except in high-curvature zones, is uniform around the perimeter of a tissue and independent of the tissue geometry or density [23]. Here, we implemented this observation into our model to predict the expansion and interaction of multiple tissues by assuming that tissue edges pin in place upon contact (see Materials and Methods and Fig. 4.1). We initialized the model simulations using the initial tissue locations from experiments, and we used $v_n = 29.5$ μm/h as measured in Ref. [23] and confirmed here (Materials and Methods). Without any fit parameters, these simulations predict the shape evolution of the colliding tissue pairs in our experiments (Fig. 4.3, Supplementary Video 3, blue/yellow/white outlines show model predictions).

Consistent with our observations, pairs of equally-sized rectangles or circles produce a straight boundary, while mismatched shapes produce a curved boundary (Fig. 4.3a-d). In our model, this is because the initial tissue edges are equidistant to the dividing midline in equal tissues but closer to the midline in large tissues than smaller tissues. In all cases, we found that the mean error of the predicted boundary was compatible with its measured roughness (Fig. 4.4b), showing that our modeling approach is appropriate at these large scales.

4.3.3 Homotypic tissue boundary dynamics and collision memory

Having analyzed the macro-scale patterns formed by colliding tissues, we next focused on the dynamics at the collision boundaries. Using the same configuration of two rectangles as in 4.3a as a control (Fig. 4.3a), we then compared the boundary dynamics of tissue pairs with a mismatch in either tissue width (1000 μm vs. 500 μm, 4.5b) or cell density (2640 cells/mm^2 vs. 1840 cells/mm^2, 4.5c).

First, we determined how asymmetry in tissue width or density affected boundary motion upon collision. We tracked the mean tissue boundary and found that wider and denser tissues displaced narrower and less dense tissues, respectively. Boundary motion was pronounced, directed, and sustained for $15-20$ h before stopping (red and blue in 4.5d). In contrast, control experiments with symmetric tissue collisions showed larger boundary fluctuations with very little average drift (black in 4.5d). Prior studies have noted similarly biased boundary dynamics, but only in *heterotypic* tissue collisions, for example between wild-type and Ras-transformed endothelial cells [196, 197]. Here, we show that collisions between *homotypic* tissues – genetically identical – also produce boundary motion due to asymmetry in tissue size or cell density. In contrast to heterotypic collisions [197], however, homotypic tissue boundary motion eventually stops.

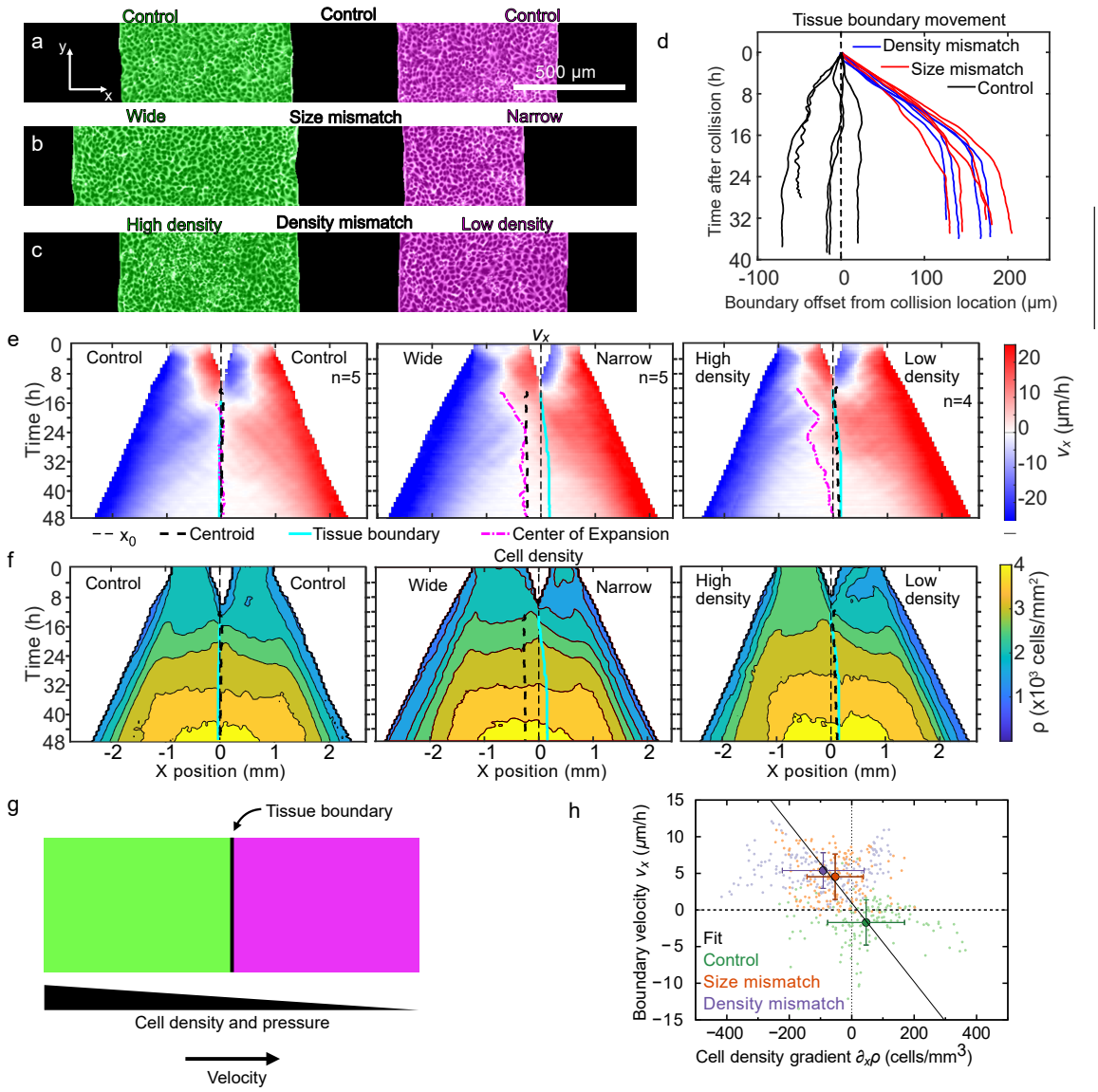

Figure 4.5: Asymmetric tissue collisions produce boundary motion. (a-c) Initial condition of collisions between control (a), size mismatch (b), and density mismatch (c) rectangle tissue pairs. (d) Tissue boundary displacement in both mismatch and control collisions. (e-f) Kymographs of tissue velocity v_x (e) and cell density (f) along the collision direction for control (left), size mismatch (center), and density mismatch (right) collisions. The superimposed curves indicate initial midline location x_0 (thin black dashed line), the geometric tissue centroid (thick black dashed line), the tissue boundary (cyan line), and the center of expansion (pink dash-dotted line) as defined in the text. (g) Our model proposes that the tissue boundary moves driven by pressure gradients between tissues of different cell density. (h) Consistent with our model, the velocity and the cell density gradient at the tissue boundary are negatively correlated ($r = -0.34$). Small points represent individual experiments, big points correspond to the averages for each of our three assays, and the black line is a linear fit through the averages. Error bars are standard deviation.

We related boundary motion to tissue flow using particle image velocimetry (PIV) to measure the velocity field. We represented these data in kymographs of the velocity component along the collision direction, v_x, averaged over the tissue length, across multiple tissue collisions (Fig. 4.5e, see Materials and Methods). With identical (control) tissues, cells around the tissue boundary symmetrically reversed their velocity shortly after collision; convergent motion became divergent. We defined the "center of expansion" as the position from which tissue flow diverges. To determine this position, we first thresholded each kymograph of v_x as $|v_x| < 3$ μm/h. We filtered for the largest contiguous region and took the midline of this region as the center of expansion. For control tissues, the center of expansion lies very near the tissue centroid shortly after collision (Fig. 4.5e left).

At what point, if any, do two fused tissues act as one? We investigate this question in collisions between tissues with size or density mismatch, which exhibited tissue flow towards the less dense or narrower tissues. In these cases, the centers of expansion began at the centroid of wider or denser tissues rather than at the overall centroid or collision boundary (Fig. 4.5e center and right). The center of expansion then gradually shifted towards the centroid of the fused tissue. After the center of expansion reached the overall centroid, the fused tissue expanded symmetrically without memory of the collision. Thus, by comparing expansion centers to geometric centroids, we identified the transition whereby two colliding tissues shift behaviors to act as one larger tissue.

4.3.4 Cell density gradients drive boundary motion

We hypothesized that collision boundary motion was driven by cell density gradients [200–204]. To test this, we quantified local cell density (Materials and Methods) and represented it in kymographs for each collision assay (Fig. 4.5f). In all cases, we found collision boundaries moved down local density gradients, consistent with our hypothesis. While tissues in the size-mismatch assay had the same initial density,

the larger tissue had a higher density at the time of collision (Fig. 4.5f center). This observation is consistent with our prior work showing that, even when prepared with the same density, larger tissues develop higher cell densities than smaller tissues as they expand(see Fig. 3.12).

To understand the mechanics of this process, we modeled the expanding tissue as an active compressible medium [138]. Tissue expansion is driven by polarized active cell-substrate forces, which are known to be maximal at the tissue edge and decay over a distance $L_c \sim 50$ μm as we move into the cell monolayer [83, 144]. Hence, we ignore active traction forces at the tissue boundary after collision, which is ~ 1 mm away from the outer tissue edges. At the collision boundary, we establish a force balance whereby pressure gradients drive tissue flow $\boldsymbol{v}$ as

$$-\boldsymbol{\nabla} P = \xi \boldsymbol{v}, \tag{4.3.1}$$

where ξ is the cell-substrate friction coefficient. Moreover, we assume that the tissue pressure P increases with cell density ρ as specified by an unknown equation of state $P(\rho)$, with $P'(\rho) > 0$. Hence, we obtain

$$\boldsymbol{v} = -\frac{P'(\rho)}{\xi} \boldsymbol{\nabla} \rho, \tag{4.3.2}$$

which predicts that the collision boundary moves from high to low densities with a speed proportional to the density gradient (Fig. 4.5g).

To test this prediction, we measure both the velocity and the density gradient at the boundary for each experiment in our three different assays. Boundary velocity was found from the position change of the midine in Fig. 4.5d. Cell density gradient $\partial_x \rho$ was found as $\frac{\rho_R - \rho_L}{x_R - x_L}$, where ρ_L and ρ_R are the total density within 300 μm wide regions immediately to the left and right of the tissue boundary, respectively, and $x_R - x_L = 300$ μm. We plotted $\partial_x \rho$ for timepoints between 20 h and 36 h, which is

after collisions and before the boundary stops moving. Consistent with our prediction, the results show a negative correlation between the boundary velocity and the cell density gradient (Fig. 4.5h).

4.3.5 Estimating tissue mechanical properties from collisions

Based on our model, we use our measurements of cell density and velocity to extract information about the tissue's equation of state $P(\rho)$. To this end, we obtain the average boundary velocity and density gradient for each assay, and we fit a line to them (Fig. 4.5h). From this fit, and using $\xi \sim 100$ Pa·s/μm^2 [144, 205], we obtain $P'(\rho) \sim 1.5$ Pa·mm^2. This result indicates that, in the conditions of our experiments, for every cell that we add per square millimeter, the tissue pressure goes up about 1.5 Pascals.

Next, we use these results to estimate the mechanical properties of the cell monolayer. To this end, we assume a specific equation of state:

$$P(\rho) = K \ln\left(\frac{\rho}{\rho_e}\right), \tag{4.3.3}$$

where K is the bulk modulus of the monolayer and ρ_e is a reference cell density. This equation of state was justified theoretically for growing tissues around their homeostatic state, around which the cell proliferation rate varies linearly with cell density [206]. From 4.3.3, we have $P'(\rho) = K/\rho$. Using the average cell density measured in our experiments during boundary motion, $\rho = (3.4 \pm 0.2) \times 10^3$ mm^{-2} (S.D.), we estimate $K \sim 5$ kPa.

This order-of-magnitude estimate falls in between two previous measurements of bulk moduli of MDCK cell monolayers. First, in-plane stretching of suspended cell monolayers yielded a stiffness $E = 20 \pm 2$ kPa [79]. Because these monolayers have no substrate, cells do not migrate, and hence suspended monolayers might have different

mechanical properties than on a substrate. Second, in spreading cell monolayers, a linear relationship between tension and strain revealed an effective tensile modulus $\Gamma = 2.4 \pm 0.4$ mN/m [207]. Using a monolayer height $h = 5$ μm [124, 144], this value translates into a stiffness $E \approx 0.48$ kPa. Complementary to these measurements, which probe tissue stiffness under extension, our estimate reflects the stiffness of the cell monolayer under the compression that results from a tissue collision.

Overall, our collision assays provide a way to probe the bulk mechanical properties of migrating cell monolayers, which are otherwise difficult to measure. Remarkably, analyzing collisions between tissues that differ only in their cell density allowed us to infer mechanical properties without measuring any mechanical forces. Rather, we employed our model to relate tissue flows to pressure and density gradients, from which we inferred the relationship between pressure and density. In the future, collision assays might be used to measure the equation of state of cell monolayers, which is a key input for mechanical models of growing and expanding tissues [80, 138].

4.3.6 Heterotypic tissue boundary dynamics

Having studied collisions between homotypic tissues, we now turn to collisions between heterotypic tissues with different cell migration speed and cell-cell adhesion strength. We prepared co-cultures of the breast cancer cell lines MCF10A (benign), MCF7 (malignant, non-invasive), and MDA-MB-231 (metastatic) as monolayers of the same size and cell density. We used homotypic MCF10A collisions as a reference, for which we observed non-mixing collision boundaries.

We first collided monolayers of MCF10A and MDA-MB-231 cells, which have the largest phenotypic difference among the cell lines we used. While these tissues have similar expansion speeds, MCF10A tissues have much higher E-cadherin expression and therefore cell-cell adhesion strengths [208]. Upon collision, the MCF10A tissue

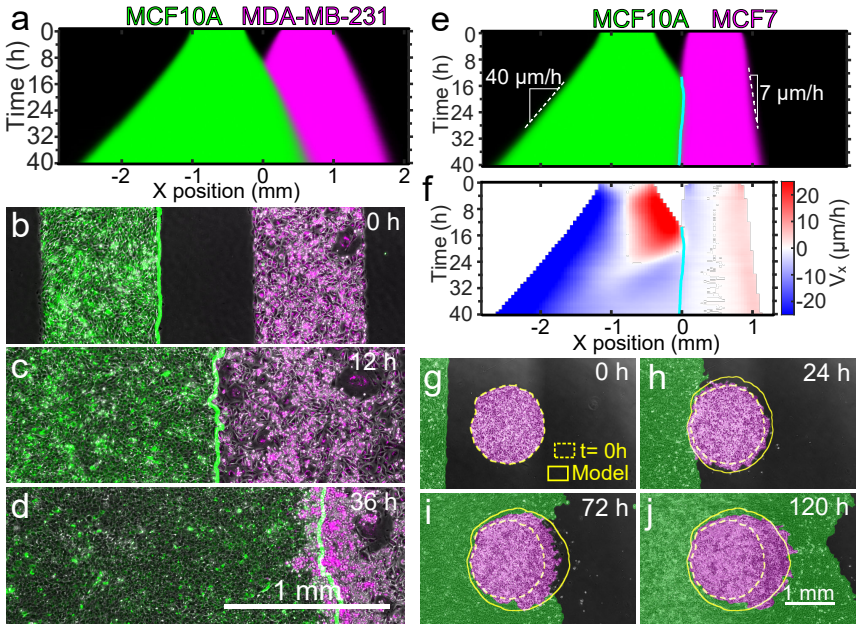

Figure 4.6: Heterotypic tissue collisions. (a) Average kymograph of segmented fluorescence for collisions between rectangular MCF10A and MDA-MB-231 tissues of the same size and cell density. The MCF10A tissue displaces the MDA-MB-231 tissue. (b-d) Snapshots of the co-culture at the initial configuration (b), the collision time (c), and 24 h after collision (d). The green line indicates the edge of MCF10A tissue. (e-f) Average kymographs of segmented fluorescence (e) and velocity v_x (f) for collisions between rectangular MCF10A and MCF7 monolayers of the same size and cell density. The cyan line indicates the tissue boundary. (g-j) Snapshots of the initial configuration (g), collision onset (h), partial engulfment (i), and full engulfment (j) of a circular MCF7 tissue by a rectangular MCF10A tissue. Simulations (yellow outlines) confirm that a difference in expansion speed is sufficient to predict the engulfment process.

simultaneously displaced and crawled underneath the MDA-MB-231 tissue (Fig. 4.6a-d).

We next investigated collisions between MCF10A and MCF7 monolayers. The MCF7 monolayer expands about 6 times more slowly than the MCF10 monolayer, which allowed us to explore the effects of different edge speeds on tissue collisions. Surprisingly, we found that the slower MCF7 tissues actually displaced the MCF10A tissues (Fig. 4.6e), which may be due to differences in cell-cell adhesion and eph/Ephrin signaling [209]. This, at least, shows that a higher expansion speed does not imply a higher "strength" upon collision. In fact, MCF10A cells at the collision boundary

reversed their velocity and migrated away from the MCF7 tissue within 8 hours after collision, starting at the boundary and progressively moving into the MCF10A monolayer (Fig. 4.6f). This behavior seems a tissue-scale analog of the cellular behavior known as contact inhibition of locomotion[1], whereby a cell stops and reverses its direction of motion upon collision with another cell [15, 17, 18].

Further, in collisions between tissues with different expansion speed, the faster tissue should be able to engulf the slower tissue, similar to the engulfment between tissues with differential adhesion [210]. We confirmed this hypothesis in collisions between strips of MCF10A cells (fast) and circles of MCF7 cells (slow), which we reproduced with our tissue shape model by incorporating different speeds into our simulation (Fig. 4.6g-j; see Materials and Methods and Fig. 4.2). Future work is needed to elucidate the biophysical properties of heterotypic tissue interfaces, but here we highlight how differences in expansion speed enable design options.

4.3.7 Large-scale tissue tessellations for cell sheet engineering

The stereotyped nature of tissue-tissue collisions suggest simple underlying design rules that would allow self-assembled tissue tessellations to be designed first in silico and then realized in vitro. We tested this idea with a tesselation inspired by the artwork of M.C. Escher—a 'dice lattice' (Fig. 4.7a). To design this tesselation, we used the computational model described above to simulate many initial tissue array conditions until converging on the pattern of ellipses shown in 4.7b. We engineered this pattern with tissues (Fig. 4.7c) and filmed it developing as predicted (Fig. 4.7d; Supplementary Video 4). This computer-aided-design (CAD) process generalized to

[1]This is the classical definition of contact inhibition proposed by Abercrombie [15] to describe how a cell repolarizes upon collision with another cell. Contact inhibition of locomotion has also come to describe the decrease in cell velocities observed as the cell density increases in a tissue (see Fig. 3.13e)

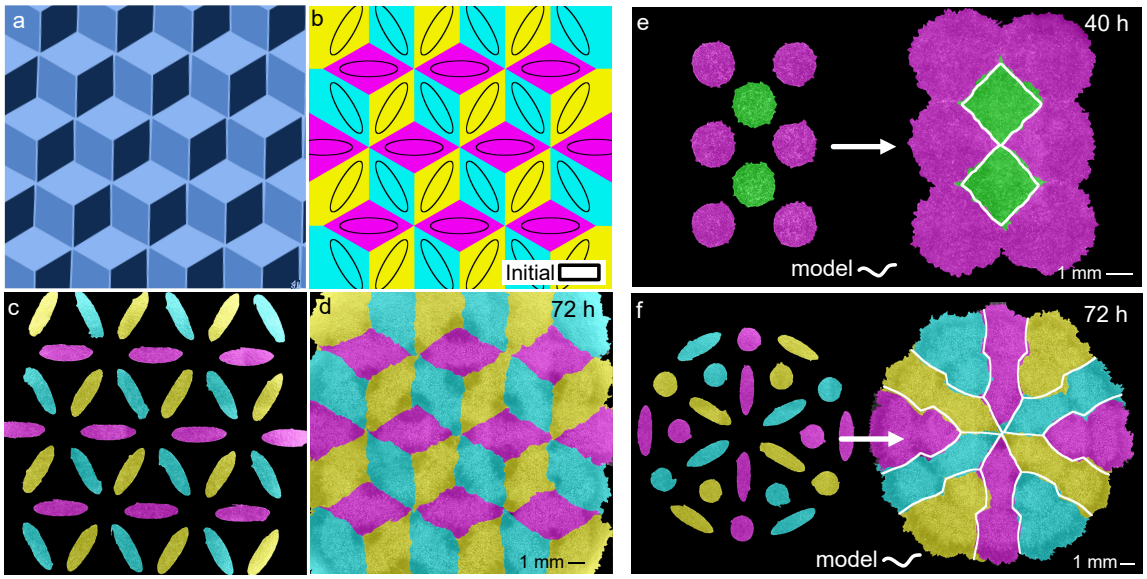

Figure 4.7: TissEllate approach to design complex tissue composites. (a,b) Target tricolor tessellation (a) and chosen initial condition with accompanying final pattern simulated using *TissEllate* (b). (c,d) In vitro realization of the tissue composite, which self-assembles from the initial pattern (c) to the final tesselation by collision (d). (e,f) Initial pattern and final tessellation for a two-dimensional hexagonal lattice (e) and another complex pattern (f). The white outlines indicate the simulated tissue shapes.

arbitrary tessellations (Fig. 4.7e,f), offering a 'TissueCAD' approach to designing and building composite tissues.

Composite cell sheets may be particularly useful for tissue engineering, where cell sheets are extracted from culture vessels and used as building blocks for larger constructs. We demonstrated compatibility of this process with our tissue composites by culturing a dice lattice on a temperature-responsive substrate (UpCell dishes) and then transferring the tissue to a new culture dish (Fig. 4.8, Materials and Methods). The morphology of sharp tissue-tissue interfaces were preserved during the transfer, demonstrating that such tissue composites can, in principle, be handled like standard cell sheets.

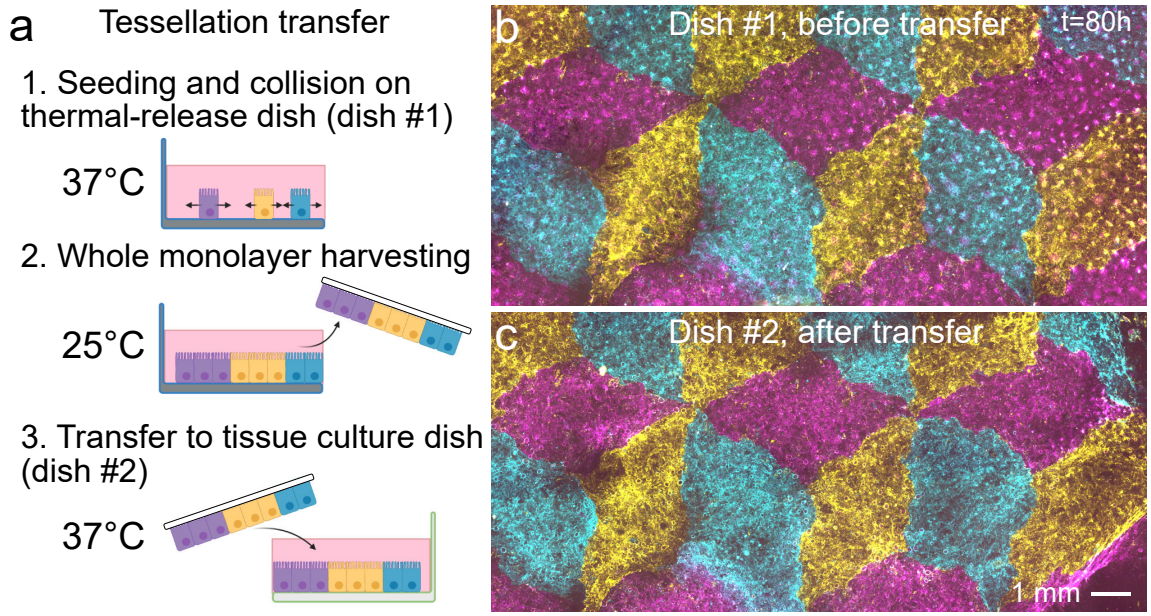

Figure 4.8: Transfer of intact tissue tessellations. (a) Schematic of the tissue tessellation transfer process. A support membrane (white) facilitates cell sheet removal and transfer at room temperature from cell culture-ware with temperature-switchable cell adhesion (UpCell). Created with Biorender.com. (a,b) Tessellation on UpCell dish (b) is transferred to standard tissue-culture dish (c).

4.3.8 Dynamics at tri-tissue collisions

During the self-assembly of tissue tesselations, we observed a special behavior at tri-tissue collision points: We often found long streams of tissue that necked down to the single cell scale, visually reminiscent of streams of invasive cancer cells (Fig. 4.9a, b). These events, which we denote 'escapes', involve the co-migration of all three tissues rather than the invasion of one tissue into the others (Fig. 4.9c-e). Consequently, the initial relative positions of the three colliding tissues is a strong statistical determinant of escape events (Fig. 4.10a, b). For a baseline quantification of the frequency of escape events (here for an interior angle of 110°), we defined escapes as those 'escaping' tissues that are within 1 correlation length of the tissue edge ($\sim$200 μm) after 60 h of tissue expansion and collision. We note that all tissues reach closer to the edge than the simulation, indicating the escape effect is present in all tissues (see Fig. 4.11).

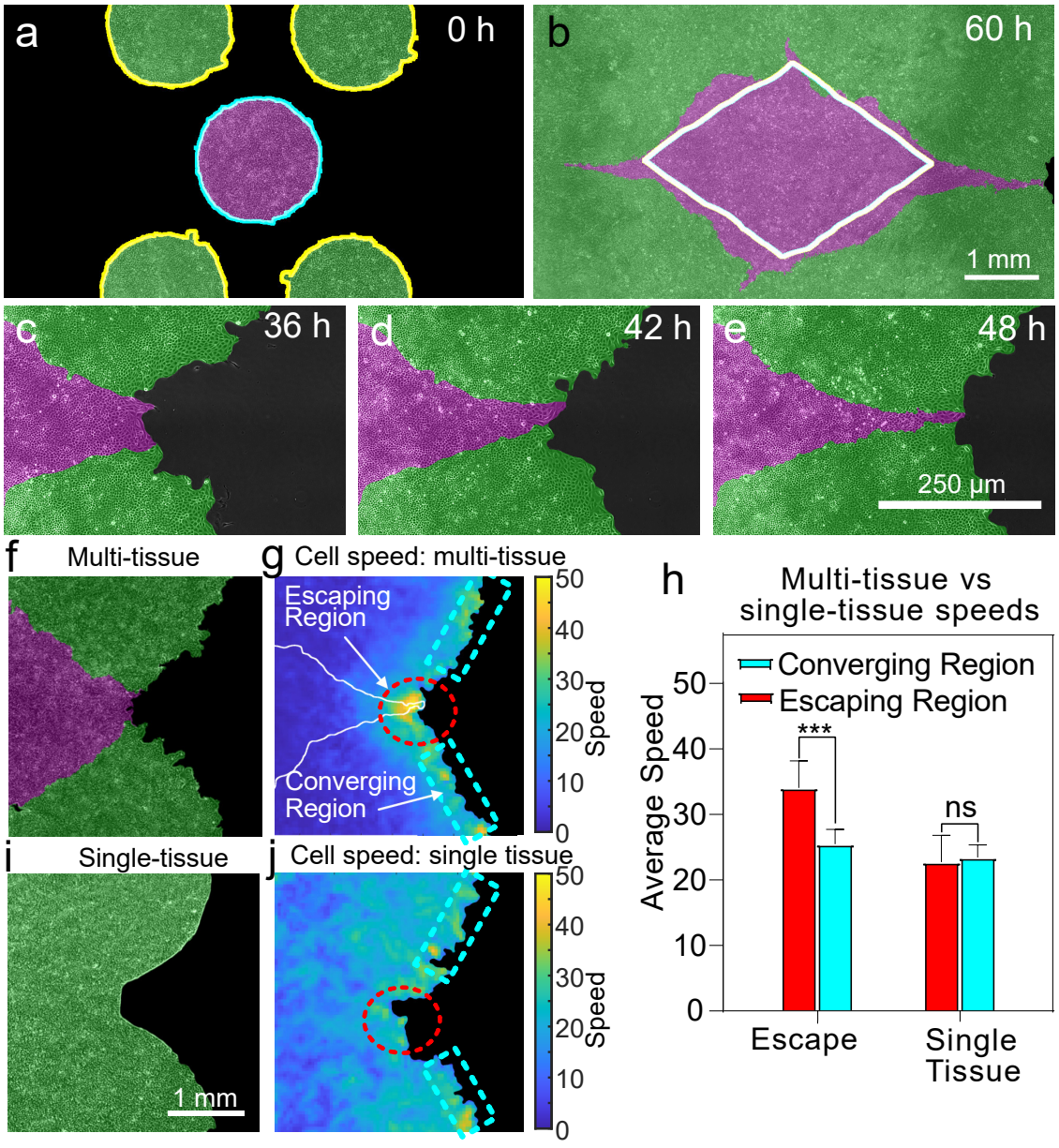

Figure 4.9: Tri-tissue collisions produce 'escape' events. Escapes occur in 50% of cases, $n = 14$, see Fig. 4.11. (a,b) Example configuration in which the magenta tissue nearly escapes in between the green tissues during expansion. (c-e) Close-up view of the escape process, from a different experiment with higher magnification. (f-h) Tissue dynamics in a tri-tissue collision (f)) feature a higher local cell speed in the escaping region than the converging region (g) with a p-value of 0.006 (h) calculated using a two-tailed Mann-Whitney U test. (i,j) A single tissue with a similar pre-escape geometry (i) does not have this speed increase in the escaping region (j). Error bars are standard deviation.

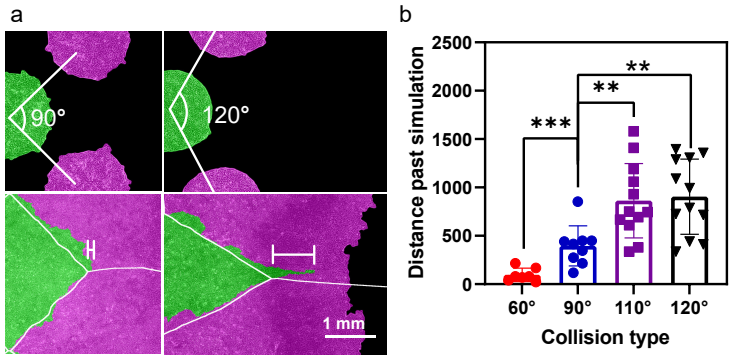

Figure 4.10: Escape amounts depend on starting tissue configuration. (a) Representative escapes for converging tissues at an initial interior angle of 90° vs. 120°. TissEllate predicts the green tissue will migrate farther laterally between the magenta tissues in the 120° configuration than in the 90° configuration (white outlines). Even so, the green tissue exceeds these predictions by more in the 120° case. Distance bar represents the distance past simulation for these examples. (b) Distance that escaping tissue overshoots the model at 60 h for a variety of initial tissue angles. P-values were calculated using a two-tailed Mann-Whitney U test.

We characterized the dynamics of escapes by measuring cell speed fields around tri-tissue collisions, which showed that the escaping tissue migrated faster than its neighbors (Fig. 4.9f-h, measurements via PIV). To determine whether this speed increase was a generic consequence of the local negative curvature of tri-tissue collision points, we compared tri-tissue collisions to a single tissue patterned to match the overall shape of the colliding tissues at the time of escape (Fig. 4.9i). For the single tissue case, we did not observe any speed increase (Fig. 4.9h,j), which rules out local curvature as the sole cause of escape events. These findings suggest that escapes are an emergent dynamical property of three-tissue interactions.

Overall, multi-tissue collisions produce unique, dynamic boundary conditions and mechanical states that give rise to surprising, almost morphogenetic behaviors at tissue junctions, suggesting an important role for collisions in composite tissue development and engineering.

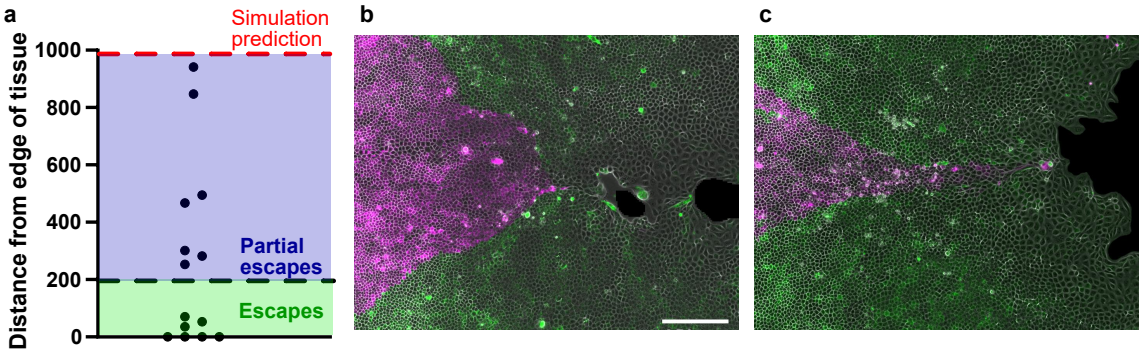

Figure 4.11: Escape frequency. (a) Distance of escaping tissue from the outer edge of converging tissues after 60 h of tissue growth, for converging tissues with interior angle of 110°. In these examples, the phenomenological model would indicate expectation of ∼1 mm from the tissue edge at this time. Representative escapes, with partial escape (b) and true escape (c).

4.4 Discussion

We investigated how tissue-tissue interactions can be harnessed to self-assemble complex composite tissue sheets – tissue tessellations. First, we demonstrated that colliding tissues change shape in stereotyped and predictable ways. Then, we proposed a physical model of tissue-tissue collisions that links the motion of the tissue boundary to underlying gradients in cell density, which drive tissue flow. Further, we used this model to estimate material properties of the colliding tissues without any force measurements. In this context, previous work had shown that heterotypic tissues can displace each other upon collision [196, 197]. Our findings revealed that even homotypic tissues, which are genetically identical, can displace each other based on purely mechanical differences. Therefore, our collision assays could be used to study mechanical tissue competition [200–204, 211, 212], which might provide biophysical insight into development [213, 214], homeostasis [215], and tumor growth [200, 211].

Based on the reproducible and almost algorithmic tissue interactions that we found, we developed computational design tools to create complex tissue tesselations. The tesselations are obtained by self-assembly, which allows the tissue boundaries to develop naturally. Thus, our work demonstrates how tissue sheets can be treated

as 'designable' living materials. Specifically, we developed a simulator that, despite lacking both biophysical laws and cellular resolution, predicts tissue patterns accurately at the 100+ μm scale. This feature makes the simulator useful to design tissue composites in silico before realizing them in vitro. This approach is compatible with advanced biofabrication strategies such as cell sheet engineering, which we demonstrated by transferring an 'Escher' tissue sheet between Petri dishes while preserving tissue integrity and internal boundaries. Tissue tessellation should also be compatible with bioprinting, which could be used to pattern larger arrays of the initial tissue seeds.

Chapter 5

Conclusions and outlook

5.1 Conclusions

In this work, we study macroscopic tissue expansion, collision, and fusion using the MDCK monolayer tissue model system. Broadly, we find that our experiments with larger length scales and longer timescales produce larger and more persistent coordinated motion than have been previously reported [39]. Moreover, the remarkably steady tissue expansion (Fig. 3.3) and collision (Fig. 4.5) dynamics allowed us to precisely build tessellated tissue composites via self-assembly from arrays of seedling tissues.

In Chapter 3, we used whole-tissue, long-term, high resolution time-lapse imaging to characterize the dynamics of free expansion of large epithelia. We found that, due to the constant normal velocity v_n of the expanding tissue edge, the rate of area increase of a spreading tissue depends on its perimeter-to-area ratio. The local density evolution, which depends on the relative increase of area vs. cell number, will then depend on tissue shape and size. Moreover, below and above the tissue sizes for which proliferation exactly balances area increase, tissue density will oppositely decrease and increase, respectively, which is exactly what we saw in the case of our

'small' and 'large' expanding circular tissues. This difference in density evolution has a critical effect on the dynamics of small vs. large tissue centers, which was most obvious in the case of the tissue-spanning vortex.

From a collective dynamics perspective, the presence of intense, large scale vortices points to potential length scales of collective behavior that dwarf the expected limit of the velocity-velocity correlation length of the constituent agents; in our case, the vortices included thousands of cells despite the fact that the velocity-velocity correlation length for this cell type is usually only 5-10 cells lengths. For biological processes, the long-time evolution of the vortices over several cell cycles emphasizes the ability for biological processes to synchronize cell divisions with cell migration over longer timescales, and the decoupling of the center vortex region from the boundary growth region demonstrates that a single, cohesive tissue may undergo multiple biological processes independently.

This decoupling of center and edge regions was especially pronounced in our cell cycle data. The highly cell-dense large tissue centers became enriched in G0/G1 phase, while the edge region was enriched in G2/M phase from 12 h until the end of the experiment. In large tissues, the tissue centers achieve a 'homeostatic' steady state (low velocities, cell cycle arrest, high cell density) while the expanding edges adopt a much more dynamic steady state of fast migration and high proliferation. The cell cycle and migration dynamics of the tissue edge was so robust to internal tissue perturbations that the tissue-spanning vortex did not produce any perceptible change in edge dynamics.

In Chapter 4, we investigated the dynamics of tissue collisions, a phenomenon less studied than general tissue expansion. We saw that, for colliding parallel strips of tissue with mismatched starting tissue size or cell density, the boundary between tissues systematically moved away from the larger and higher density tissues. We model this phenomenon as pressure driven flow(see Fig. 4.5), where a very general

equation of state for tissue with positive $P'(\rho)$ agrees with our observed direction of boundary motion. This density gradient-driven tissue displacement in *genetically-identical* tissues represents a major finding of this work, since tissue displacement had only previously been observed in collisions between tissues from different cell lines.

Assuming a specific equation of state then allowed us to estimate the bulk modulus of our tissues, which represents the stiffness of the tissues under the compression resulting from a tissue collision. While the modulus of freely-suspended tissue monolayers have been measured via stretch [79], compressing a tissue is much more difficult. Moreover, as discussed in Chapter 2, measurements of mechanical properties should be performed via external perturbations at time scales, length scales, and magnitudes relevant to the tissue of interest; here, the deformation indeed comes from another genetically-identical tissue.

We then examined tissue shape changes as multiple tissues expand, collide and fuse. The eventual tessellations formed during tissue collision proved to be highly stereotyped and predictable, so we developed a tool (TissEllate) for designing patterns that self-assemble from arrays of seedling tissues (Fig. 4.7). Tessellated sheets are used in co-culture experiments for studying interactions across different cell types and are limited by current techniques to two cell types; our approach in principle allows as many cell types as initial seedling tissues, and we demonstrate 28 seedling tissues with three 'colors.' Cell sheets are also used in cell therapy applications, and we demonstrated here that our cell sheet tessellations can be harvested intact like cellular films (Fig. 4.8). Our approach to building 2D cell sheets represents a middle-ground between full self-assembly and direct construction. While initial conditions and geometries were precisely controlled, these conditions changed as the system was allowed to naturally evolve.

5.2 Future directions

Looking forward, there are many potential directions of investigation either directly stemming from or related in principle to this work.

First, one may consider whether the size-dependent patterns of proliferation and migration that we observed in Chapter 3 are relevant to tissues with more homeostatic-like initial conditions. In our study in Chapter 3, we were careful to begin our experiments with tissues that were still actively dividing and proceeding through the cell cycle. However, it would be interesting–and perhaps more physiologically-relevant to regeneration contexts–to begin experiments with a tissue fully in cell cycle arrest, like the final state of large tissue centers. Release of the stencil would then represent an immediate departure from a pseudo-homeostatic state. While the dynamics of the tissue edges would likely be similar to what we saw here, the tissue centers (especially of small tissues) would likely be effected by this difference, perhaps even preventing vortex formation. We saw that moderate increases in density resulted in earlier vortex peaks, and such a high starting density may halt cell motion before the vortex can emerge.

This leads to another question of interest: What are the necessary and sufficient conditions for the emergence of our persistent, tissue-wide vortex? Cell divisions may be necessary to fluidize [80] the tissue so that the interior can rotate freely. By introducing a cell division inhibitor before or after the time of vortex emergence, one could learn if cell division events are necessary for vortex emergence or growth. Along similar lines, inhibiting the action of myosin at the vortex emergence time should inform whether active cell-cell contractile forces are necessary for vortex formation and growth. Finally, investigating a spectrum of tissue sizes may reveal a critical tissue size below which long-wavelength spontaneous flows do not emerge, which was predicted by the polar fluid model in Fig. 3.8.

Our discussions of tissue memory could also be developed further. In a direct follow-up experiment, one may ask at what point one of our initially-small tissues will be no different from an initially-large tissue of the same current size. As a major contributor to a manuscript in preparation with lead author Abraham E. Wolf and coauthors Isaac Breinyn and Daniel J. Cohen, we studied mechanical memory effects in the context of electric stimulation. In preliminary results, we see that the tissue centers exhibit much more robust memory of a prior electric stimulation than tissue edges. While tissue edges follow the 'signal' of the free edge once electric stimulation is stopped, the tissue bulk features lasting mechanical changes that alter migration patterns and cell coordination.

Our work using tissue collisions for relating tissue pressure with other physical properties also offers promising future directions. Future work can put theorized tissue equations of state to the test by carefully sweeping over collisions over a range of densities and density gradients[1] [80, 138]. While we only considered the effect of *cell density* on tissue pressure, it would be interesting to consider other factors such as tissue maturity[2]. Cell-cell junction maturation increases the viscosity of the tissue [83], but it is not clear how this factor will influence its pressure. We saw in Fig. 4.6 that the cohesive tissue overwhelmed the tissue with low adhesion, so we may expect a more mature tissue to displace a less mature tissue; however, these cell lines feature many other complicating differences as well.

Bioprinting, and tissue engineered constructs in general, still face broad challenges in creating cell-dense tissues of physiological sizes with nutrient supply and mechanical functionality [216]. Our design framework for building tessellated cell sheets suggests

[1] While we were focused on collisions of whole tissues, studies of boundary motion with the intent of extracting mechanical properties should use much wider starting tissues, so the expansion process does not significantly alter tissue densities. This approach should also result in longer-lasting density gradients and less noise

[2] It should be straightforward to control the tissue density while changing tissue maturity by seeding tissues on different days and compensating for the density increase in the first tissue while waiting to seed the second tissue.

potential analogous strategies such as bioprinting tissue primitives that grow evolve and fuse into final forms rather than predifining all geometries. Nature builds organisms by directed migration, cell growth, and self-assembly of a very small initial clump of cells, so this may be an important direction for the future to complement current approaches. More presently, we hope that our findings inspire the tissue engineering community to develop more engineering design tools as we build the tissues of the future.

Appendix A

Reusable replacement component for Powered Air Purifying Respirators

Early in the COVID-19 pandemic of 2020, this author and many others in the Princeton community determined to help local hospitals and health centers by taking on projects ranging from 3D printing face shields to designing off-the-shelf ventilators. This author took particular interest in helping to address Princeton Penn Medical Center's dire shortage of the face-covering component for Powered Air Purifying Respirators (PAPRs). PAPRs were worn by those healthcare professionals who possessed the highest risk of contracting SARS-CoV-2 due to having the most exposure to COVID-19 patients. In addition to the device design described below, the author set up an organizational structure whereby volunteer teams built hundreds of these components from home. Different members performed the different functions of supply preparation, supply transportation, assembly instruction, device fabrication, device validation, and delivery, all without coming in contact with one another.

Figure A.1: Powered Air Purifying Respirator (PAPR) in use. A scientist handing reconstructed 1918 Pandemic Influenza virus in 2005 wears a PAPR. Fresh air in this PAPR is supplied to the head and face area via a tube connected to a fan and filter at the wearer's back. Photograph from Centers for Disease Control and Prevention's Public Health Image Library, public domain.

A.1 Background

PAPRs protect the wearer from droplets and aerosols by creating a positive-pressure environment for the user's head and face while constantly providing fresh air filtered through a HEPA filter (see Fig. A.1). PAPRs were used extensively during the Ebola outbreak, which spread primarily by droplets[217]. HEPA filters remove at least 99.97% of particles 0.3 μm or smaller, while N95 respirators remove 95% of particles 5 μm or smaller. Owing to the superior filtering and integrated face covering, PAPRs

are much more protective than N95 masks[1] as long as correct donning and doffing procedures are followed[218]. However, PAPRs are generally associated with reduced mobility and communication ability for the wearer[219], likely due to obstruction of vision, fan noise, and general bulk, so they should only be worn in appropriate situations. For a more thorough comparison of N95 masks and PAPR systems, see a recent article on the topic[218].

A.2 Max-air PAPRs

Princeton Medical Center owned a stockpile of PAPRs that were manufactured by Syntech under the Max-Air brand (see Fig. A.2). This proprietary variation on the classic PAPR featurs a fan and filter contained within the helmet (to reduce bulk vs. PAPRs with hoses), and a thin, transparent face shield that securely attached to the helmet and wrapped around the wearer's head and under the wearer's chin (to reduce vision obstruction). The face cover snaps onto the helmet via attachment holes and includes an underside membrane that stretches under the chin to form an airtight seal around the wearer's face.

The necessary face cover component for this particular kind of PAPR is non-reusable. The stretchable membrane is the main culprit, as it becomes too loose after several wears to properly seal under the chin. Moreover, the materials in the stretchable membrane loses mechanical integrity when sterilized with methanol. During the worst months of the pandemic in the USA, replacement covers were unavailable for purchase. Princeton Medical Center only had two remaining PAPR covers at one point, and needed dozens more within days and hundreds within weeks. Several groups had attempted to make viable replacement PAPR face shields off-the-shelf, but several raw material challenges proved difficult:

[1]During the COVID-19 pandemic, health professionals oftern paired N95 masks with face shields (for which this author also led fabrication). However, face shields do not prevent complex airflows from directing droplets or aerosols to the wearer's face.

Figure A.2: MaxAir PAPR. Medical professional wearing the MaxAir PAPR with PAPR face shield made by Princeton volunteers. Face shield features a stretchable membrane (i) transparent face cover (ii) and attachment holes (iii).

- PET plastic commonly used for face shields was unavailable in most parts of the country
- Flexible membranes that can withstand repeat use and sterilization procedures are difficult to find
- Rubbers (for the membrane) are notoriously difficult to bond to plastics

A.3 Princeton PAPR face shield design

We designed an alternative face cover that can be made entirely using materials from Stockwell Elastomerics (Philadelphia, PA), a silicone supplier and silicone parts and adhesives manufacturer that supplies Daniel J. Cohen's lab's silicone for tissue patterning stencils. Our design includes (1) a transparent plastic window that attaches

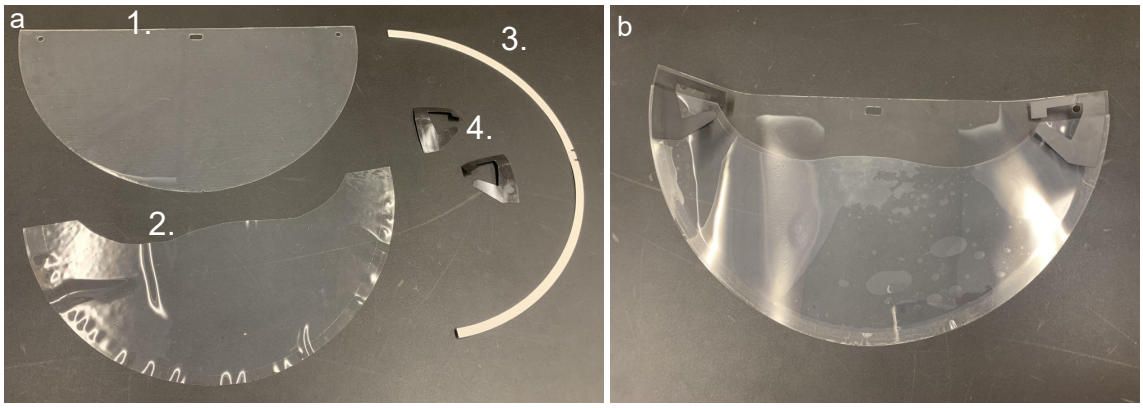

Figure A.3: Off-the-shelf face shield materials and assembly.

to the PAPR helmet, (2) a silicone rubber under-chin membrane, (3) adhesive tape to bond window to membrane, and (4) side adhesive winglets to reinforce membrane (see Fig. A.3). We will describe our particular design with notes for those without access to Stockwell's pre-cutting services (as was initially the case for us).

1 Transparent plastic window: Fortunately, Stockwell's silicone rubber is shipped with a plastic liner (of PET plastic or similar) that is normally discarded. The silicone rubber is sandwiched between an identical top and bottom liner. We simply retained one of these liners for use as the face shield. In our later rounds of producing PAPR covers, we purchased the silicone/plastic sandwich pre-cut in the configuration needed for the transparent window, including attachment holes (see drawing), so no further modifications were needed for the transparent window.

   If pre-cutting by the manufacturer is not possible, we found that a laser cutter, razor writer, or even scissors was sufficient for cutting the outer shape. Scissors surprisingly offered the highest throughput of the above options for us, but it is recommended to make a stencil or mold to use as a guide for cutting. For cutting attachment holes, those without access to a laser cutter or razor writer can use a standard hole punch, which happens to be precisely $\frac{1}{4}$in. hole size.

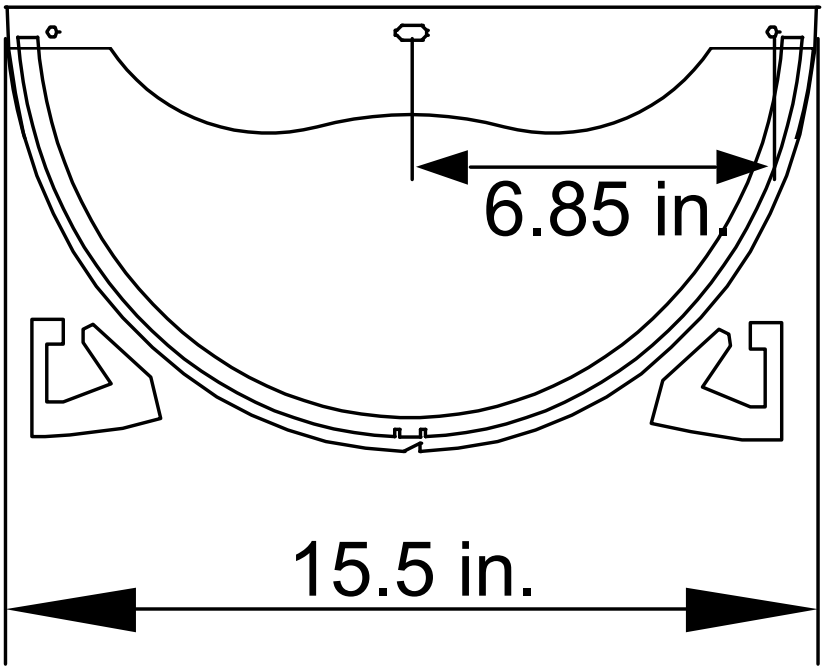

Figure A.4: PAPR cover assembly drawing. Produced by an Autodesk student version.

This crucial realization enabled us to "crowdsource" the assembly of these parts in the early days of the pandemic, where dozens of volunteers made these devices using standard office supplies.

2 Silicone rubber under-chin membrane: As opposed to the very thin material used for the under-chin membrane in disposable face covers, we found 0.01 in. thick silicone rubber to be an ideal combination of elasticity and durability. After removing the top liner (which is used as the plastic window), we left the bottom liner attached to the plastic for ease of handling. We then used a polypropylene stencil to trace the desired final silicone shape and cut along this line (see curved line in the drawing of all parts in Fig. A.4).

3 Adhesive tape: A stretchable material like silicone rubber must be used to fulfill the function of the stretchable under-chin membrane, but these materials are notoriously difficult to bond permanently to plastics. Care therefore must be

taken in choosing the proper glue or tape to bond the under-chin membrane to the over-face window. We recommend pressure-sensitive silicone-based tapes, specifically ARSealTM 90880 from Adhesives Research Inc (Glen Rock, PA) or SA-1060 from Stockwell Elastomerics. Pre-cutting by the manufacturer to final form is most desirable. During the early pandemic, we cut many tape pieces at once using a Silhouette cameo (Sillhouette America, USA).We included an optional fiducial marker in the center of the tape as well as the silicone/plastic material to facilitate aligning the tape, silicone, and transparent window (see Fig. A.4).

4 Side adhesive winglets: Reinforcing side winglets are optional but recommended as the final component of the face cover. We used polypropylene covered in SA-1060 from Stockwell Elastomerics so that they can be applied to the window/silicone membrane by simply sticking it on. Care must be taken when attaching the winglets to not obstruct the attachment holes. These pieces assist in the secure attachment of the under-chin membrane to the transparent window, keep the transparent window away from the wearer's face, and provide structural support where the membrane undergoes high stresses. The user should bend winglets to proper fit during donning.

A.4 Rapid design, fabrication, and organizational processes

During the initial device design process, we made prototypes using the vinyl cutters and laser cutters, testing mechanical integration with a broken PAPR system and rapidly iterating. We tested dozens of glues and attachment strategies before converging on the tapes mentioned in the previous section. At the time of the first successfully-tested prototype, over 20 PAPR face-covers were needed within 24 h.

This author and friend Thomas Schaffner worked faithfully to meet the immediate need while this author assembled volunteers and ordered supplies to meet the coming need for 1,000 devices.

Fabricating a single PAPR using prototyping devices and assembling them by hand was a ∼30 min process, so making 1,000 devices within 2 weeks would be nearly impossible. We assembled 35 volunteers to assist with construction from Princeton University and the community at large. However, these volunteers did not have access to prototyping devices at university labs. Therefore, we generalized the assembly processes to be able to be created with standard office supplies, cutting guide stencils for each assembler volunteer using the prototyping devices. These low-tech cutting and assembling techniques reduced fabrication time to ∼15 min per device. We then distributed supplies using the following strategy:

- Matthew collates supplies needed, dividing them into 30 self-contained kits with raw materials, assembly instructions (with associated video that can be found on YouTube), guide stencils, and all office supplies needed to assemble 35 PAPRs
- Volunteers are divided into distributors (5, those volunteers with cars) and assemblers (30). Distributors pick up supplies from Matthew's apartment and communicate any issues assemblers may have
- Assemblers construct the devices[2].
- Distributors deliver devices back to the hospital Matthew's residence (Fig. A.5).
- Matthew and Thomas Schaffner performed quality control, and the hospital picked up those devices that passed.

[2]Some assemblers decided to wait 48 hours for the supplies to "quarantine."

Figure A.5: Constructed PAPRs returned from assembly volunteers to Matthew's residence by distributor volunteers.

This approach succeeded in 14 day turnaround from raw material delivery from the supplier to finished devices picked up by the hospital, albeit with much organizational and rote effort.

Our approaches here may give insights to the types of organizational strategies and rapid design processes that may become necessary during a crisis.

A.5 Results

With a team of volunteers, we built and assembled over 1,000 devices, allowing the Princeton Medical Center to continue to use all of their available PAPRs. These devices were worn by dozens of medical workers with the most severe exposure to the SARS-CoV-2 virus, with no reported covid infections.

Figure A.6: Local nurses wearing Princeton PAPR devices.

Bibliography

[1] K. E. Kasza, A. C. Rowat, J. Liu, T. E. Angelini, C. P. Brangwynne, G. H. Koenderink, and D. A. Weitz, "The cell as a material," *Current Opinion in Cell Biology*, vol. 19, no. 1, pp. 101–107, 2007, ISSN: 09550674. DOI: 10.1016/j.ceb.2006.12.002.

[2] X. Trepat and J. J. Fredberg, "Plithotaxis and emergent dynamics in collective cellular migration," *Trends in Cell Biology*, vol. 21, no. 11, pp. 638–646, 2011, ISSN: 09628924. DOI: 10.1016/j.tcb.2011.06.006.

[3] E. Latorre, S. Kale, L. Casares, M. Gómez-González, M. Uroz, L. Valon, R. V. Nair, E. Garreta, N. Montserrat, A. del Campo, B. Ladoux, M. Arroyo, and X. Trepat, "Active superelasticity in three-dimensional epithelia of controlled shape," *Nature*, vol. 563, no. 7730, pp. 203–208, 2018, ISSN: 14764687. DOI: 10.1038/s41586-018-0671-4.

[4] C. F. Guimarães, L. Gasperini, A. P. Marques, and R. L. Reis, "The stiffness of living tissues and its implications for tissue engineering," *Nature Reviews Materials*, vol. 5, no. 5, pp. 351–370, 2020, ISSN: 20588437. DOI: 10.1038/s41578-019-0169-1.

[5] M. Poujade, E. Grasland-Mongrain, A. Hertzog, J. Jouanneau, P. Chavrier, B. Ladoux, A. Buguin, and P. Silberzan, "Collective migration of an epithelial monolayer in response to a model wound," *Proceedings of the National Academy of Sciences of the United States of America*, vol. 104, no. 41, pp. 15 988–15 993, 2007, ISSN: 00278424. DOI: 10.1073/pnas.0705062104.

[6] X. Bichat *et al.*, *A Treatise on the Membranes in General: And on Different Membranes in Particular*. Cummings and Hilliard, 1813.

[7] B. Alberts, *Molecular biology of the cell*, 2008.

[8] K. Duszyc, G. A. Gomez, K. Schroder, M. J. Sweet, and A. S. Yap, "In life there is death: How epithelial tissue barriers are preserved despite the challenge of apoptosis," *Tissue barriers*, vol. 5, no. 4, e1345353, 2017.

[9] E. Haigh, "The roots of the vitalism of xavier bichat," *Bulletin of the History of Medicine*, vol. 49, no. 1, pp. 72–86, 1975.

[10] J. B. Udgaonkar, "Entropy in biology," *Resonance*, vol. 6, no. 9, pp. 61–66, 2001.

[11] X. Bichat, *Physiological researches upon life and death*, 203. Smith & Maxwell, 1809.

[12] T. Schwann and F. Hünseler, *Mikroskopische Untersuchungen über die Uebereinstimmung in der Struktur und dem Wachstume der Tiere und Pflanzen*, 176. W. Engelmann, 1910.

[13] R. L. K. Virchow, "Cellular-Pathologie," *Archiv für pathologische Anatomie und Physiologie und für klinische Medizin*, vol. III, pp. 3–39, 1855.

[14] J. Byers 3rd, "Rudolf virchow–father of cellular pathology.," *American journal of clinical pathology*, vol. 92, no. 4 Suppl 1, S2–8, 1989.

[15] M. Abercrombie and J. E. M. Heaysman, "Observations on the social behaviour of cells in tissue culture. II. "Monolayering" of fibroblasts," *Experimental Cell Research*, vol. 6, no. 2, pp. 293–306, 1954, ISSN: 00144827. DOI: 10.1016/0014-4827(54)90176-7.

[16] M. Abercrombie and E. J. Ambrose, "Interference microscope studies of cell contacts in tissue culture," *Experimental Cell Research*, vol. 15, no. 2, pp. 332–345, 1958, ISSN: 00144827. DOI: 10.1016/0014-4827(58)90034-X.

[17] C. Carmona-Fontaine, H. K. Matthews, S. Kuriyama, M. Moreno, G. A. Dunn, M. Parsons, C. D. Stern, and R. Mayor, "Contact inhibition of locomotion in vivo controls neural crest directional migration," *Nature*, vol. 456, no. 7224, pp. 957–961, 2008, ISSN: 00280836. DOI: 10.1038/nature07441.

[18] B. Stramer and R. Mayor, "Mechanisms and in vivo functions of contact inhibition of locomotion," *Nat. Rev. Mol. Cell Biol.*, vol. 18, no. 1, pp. 43–55, 2017, ISSN: 14710080. DOI: 10.1038/nrm.2016.118.

[19] M. Vishwakarma, J. Di Russo, D. Probst, U. S. Schwarz, T. Das, and J. P. Spatz, "Mechanical interactions among followers determine the emergence of leaders in migrating epithelial cell collectives," *Nat. Commun.*, vol. 9, no. 1, 2018, ISSN: 20411723. DOI: 10.1038/s41467-018-05927-6.

[20] A. Puliafito, L. Hufnagel, P. Neveu, S. Streichan, A. Sigal, D. K. Fygenson, and B. I. Shraiman, "Collective and single cell behavior in epithelial contact inhibition," *Proceedings of the National Academy of Sciences of the United States of America*, vol. 109, no. 3, pp. 739–744, 2012, ISSN: 00278424. DOI: 10.1073/pnas.1007809109. arXiv: 1112.0465.

[21] S. J. Streichan, C. R. Hoerner, T. Schneidt, D. Holzer, and L. Hufnagel, "Spatial constraints control cell proliferation in tissues," *Proceedings of the National Academy of Sciences*, vol. 111, no. 15, pp. 5586–5591, 2014, ISSN: 0027-8424. DOI: 10.1073/pnas.1323016111.

[22] M. Uroz, S. Wistorf, X. Serra-Picamal, V. Conte, M. Sales-Pardo, P. Roca-Cusachs, R. Guimerà, and X. Trepat, "Regulation of cell cycle progression by cell-cell and cell-matrix forces," *Nature Cell Biology*, vol. 20, no. 6, pp. 646–654, 2018, ISSN: 14764679. DOI: 10.1038/s41556-018-0107-2.

[23] M. A. Heinrich, R. Alert, J. M. LaChance, T. J. Zajdel, A. Košmrlj, and D. J. Cohen, "Size-dependent patterns of cell proliferation and migration in freely-expanding epithelia," *eLife*, vol. 9, e58945, 2020, ISSN: 2050-084X. DOI: 10.7554/eLife.58945.

[24] A. J. Ewald, A. Brenot, M. Duong, B. S. Chan, and Z. Werb, "Collective Epithelial Migration and Cell Rearrangements Drive Mammary Branching Morphogenesis," *Dev. Cell*, vol. 14, no. 4, pp. 570–581, 2008, ISSN: 15345807. DOI: 10.1016/j.devcel.2008.03.003.

[25] J. A. Park, L. Atia, J. A. Mitchel, J. J. Fredberg, and J. P. Butler, "Collective migration and cell jamming in asthma, cancer and development," *J. Cell Sci.*, vol. 129, no. 18, pp. 3375–3383, 2016, ISSN: 14779137. DOI: 10.1242/jcs.187922.

[26] F. X. Yu, B. Zhao, and K. L. Guan, "Hippo Pathway in Organ Size Control, Tissue Homeostasis, and Cancer," *Cell*, vol. 163, no. 4, pp. 811–828, 2015, ISSN: 10974172. DOI: 10.1016/j.cell.2015.10.044.

[27] I. Conlon and M. Raff, "Size control in animal development," *Cell*, vol. 96, no. 2, pp. 235–244, 1999, ISSN: 00928674. DOI: 10.1016/S0092-8674(00)80563-2.

[28] C. P. Heisenberg and Y. Bellaïche, "Forces in tissue morphogenesis and patterning," *Cell*, vol. 153, no. 5, p. 948, 2013, ISSN: 10974172. DOI: 10.1016/j.cell.2013.05.008.

[29] P. Friedl, J. Locker, E. Sahai, and J. E. Segall, "Classifying collective cancer cell invasion," *Nat. Cell Biol.*, vol. 14, no. 8, pp. 777–783, 2012, ISSN: 14657392. DOI: 10.1038/ncb2548.

[30] A. W. Lambert, D. R. Pattabiraman, and R. A. Weinberg, "Emerging Biological Principles of Metastasis," *Cell*, vol. 168, no. 4, pp. 670–691, 2017, ISSN: 10974172. DOI: 10.1016/j.cell.2016.11.037.

[31] V. Maruthamuthu, B. Sabass, U. S. Schwarz, and M. L. Gardel, "Cell-ECM traction force modulates endogenous tension at cell-cell contacts," *Proceedings of the National Academy of Sciences of the United States of America*, vol. 108, no. 12, pp. 4708–4713, 2011, ISSN: 00278424. DOI: 10.1073/pnas.1011123108.

[32] X. Trepat, M. R. Wasserman, T. E. Angelini, E. Millet, D. A. Weitz, J. P. Butler, and J. J. Fredberg, "Physical forces during collective cell migration," *Nature Physics*, vol. 5, no. 6, pp. 426–430, 2009, ISSN: 17452481. DOI: 10.1038/nphys1269.

[33] D. Gonzalez-Rodriguez, S. Douezan, and F. Brochard-Wyart, "Soft Matter Models of Developing Tissues and Tumors," *Science*, vol. 82, no. November, pp. 910–917, 2012.

[34] A. K. Marel, M. Zorn, C. Klingner, R. Wedlich-Söldner, E. Frey, and J. O. Rädler, "Flow and diffusion in channel-guided cell migration," *Biophysical Journal*, vol. 107, no. 5, pp. 1054–1064, 2014, ISSN: 15420086. DOI: 10.1016/j.bpj.2014.07.017.

[35] C. G. Rolli, H. Nakayama, K. Yamaguchi, J. P. Spatz, R. Kemkemer, and J. Nakanishi, "Switchable adhesive substrates: Revealing geometry dependence in collective cell behavior," *Biomaterials*, vol. 33, no. 8, pp. 2409–2418, 2012, ISSN: 01429612. DOI: 10.1016/j.biomaterials.2011.12.012.

[36] S. Tlili, E. Gauquelin, B. Li, O. Cardoso, B. Ladoux, H. D. Ayari, and F. Graner, "Collective cell migration without proliferation: Density determines cell velocity and wave velocity," *Royal Society Open Science*, vol. 5, no. 5, p. 172 421, 2018, ISSN: 20545703. DOI: 10.1098/rsos.172421. arXiv: 1610.05420.

[37] C. M. Nelson, R. P. Jean, J. L. Tan, W. F. Liu, N. J. Sniadecki, A. A. Spector, and C. S. Chen, "Emergent patterns of growth controlled by multicellular form and mechanics," *Proceedings of the National Academy of Sciences of the United States of America*, vol. 102, no. 33, pp. 11 594–11 599, 2005, ISSN: 00278424. DOI: 10.1073/pnas.0502575102.

[38] M. J. Siedlik, S. Manivannan, I. G. Kevrekidis, and C. M. Nelson, "Cell Division Induces and Switches Coherent Angular Motion within Bounded Cellular Collectives," *Biophysical Journal*, vol. 112, no. 11, pp. 2419–2427, 2017, ISSN: 15420086. DOI: 10.1016/j.bpj.2017.05.001.

[39] S. R. K. Vedula, M. C. Leong, T. L. Lai, P. Hersen, A. J. Kabla, C. T. Lim, and B. Ladoux, "Emerging modes of collective cell migration induced by geometrical constraints," *Proceedings of the National Academy of Sciences of the United States of America*, vol. 109, no. 32, pp. 12 974–12 979, 2012, ISSN: 00278424. DOI: 10.1073/pnas.1119313109.

[40] S. Jain, V. M. Cachoux, G. H. Narayana, S. de Beco, J. D'Alessandro, V. Cellerin, T. Chen, M. L. Heuzé, P. Marcq, R. M. Mège, A. J. Kabla, C. T. Lim, and B. Ladoux, "The role of single-cell mechanical behaviour and polarity in driving collective cell migration," *Nature Physics*, vol. 16, no. 7, pp. 802–809, 2020, ISSN: 17452481. DOI: 10.1038/s41567-020-0875-z.

[41] P. Rodriguez-Franco, A. Brugués, A. Marin-Llaurado, V. Conte, G. Solanas, E. Batlle, J. J. Fredberg, P. Roca-Cusachs, R. Sunyer, and X. Trepat, "Long-lived force patterns and deformation waves at repulsive epithelial boundaries," *Nat. Mater.*, vol. 16, no. 10, pp. 1029–1036, 2017, ISSN: 14764660. DOI: 10.1038/NMAT4972.

[42] M. A. Heinrich, R. Alert, A. E. Wolf, A. Kosmrlj, and D. J. Cohen, "Self-assembly of tessellated tissue sheets by growth and collision," *bioRxiv*, 2021.

[43] L. Blanchoin, R. Boujemaa-Paterski, C. Sykes, and J. Plastino, "Actin dynamics, architecture, and mechanics in cell motility," *Physiological reviews*, vol. 94, no. 1, pp. 235–263, 2014.

[44] D. A. Fletcher and R. D. Mullins, "Cell mechanics and the cytoskeleton," *Nature*, vol. 463, no. 7280, pp. 485–492, 2010, ISSN: 00280836. DOI: 10.1038/nature08908.

[45] A. J. Ridley, "Life at the leading edge," *Cell*, vol. 145, no. 7, pp. 1012–1022, 2011, ISSN: 10974172. DOI: 10.1016/j.cell.2011.06.010.

[46] R. Farooqui and G. Fenteany, "Multiple rows of cells behind an epithelial wound edge extend cryptic lamellipodia to collectively drive cell-sheet movement," *Journal of Cell Science*, vol. 118, no. 1, pp. 51–63, 2005, ISSN: 00219533. DOI: 10.1242/jcs.01577.

[47] S. Kumar, I. Z. Maxwell, A. Heisterkamp, T. R. Polte, T. P. Lele, M. Salanga, E. Mazur, and D. E. Ingber, "Viscoelastic retraction of single living stress fibers and its impact on cell shape, cytoskeletal organization, and extracellular matrix mechanics," *Biophysical Journal*, vol. 90, no. 10, pp. 3762–3773, 2006, ISSN: 00063495. DOI: 10.1529/biophysj.105.071506.

[48] M. Murrell, P. W. Oakes, M. Lenz, and M. L. Gardel, "Forcing cells into shape: The mechanics of actomyosin contractility," *Nature Reviews Molecular Cell Biology*, vol. 16, no. 8, pp. 486–498, 2015, ISSN: 14710080. DOI: 10.1038/nrm4012.

[49] M. B. Omary, P. A. Coulombe, and W. I. McLean, "Intermediate Filament Proteins and Their Associated Diseases," *New England Journal of Medicine*, vol. 351, no. 20, pp. 2087–2100, 2004, ISSN: 0028-4793. DOI: 10.1056/nejmra040319.

[50] M. Van den Heuvel, M. De Graaff, and C Dekker, "Microtubule curvatures under perpendicular electric forces reveal a low persistence length," *Proceedings of the National Academy of Sciences*, vol. 105, no. 23, pp. 7941–7946, 2008.

[51] C. P. Brangwynne, F. C. MacKintosh, S. Kumar, N. A. Geisse, J. Talbot, L. Mahadevan, K. K. Parker, D. E. Ingber, and D. A. Weitz, "Microtubules can bear enhanced compressive loads in living cells because of lateral reinforcement," *Journal of Cell Biology*, vol. 173, no. 5, pp. 733–741, 2006, ISSN: 00219525. DOI: 10.1083/jcb.200601060.

[52] C. Garcin and A. Straube, "Microtubules in cell migration," *Essays in Biochemistry*, vol. 63, no. 5, pp. 509–520, 2019, ISSN: 00711365. DOI: 10.1042/EBC20190016.

[53] D. J. Sharp, G. C. Rogers, and J. M. Scholey, "Microtubule motors in mitosis," *Nature*, vol. 407, no. 6800, pp. 41–47, 2000, ISSN: 00280836. DOI: 10.1038/35024000.

[54] F. Van Roy and G. Berx, "The cell-cell adhesion molecule E-cadherin," *Cellular and Molecular Life Sciences*, vol. 65, no. 23, pp. 3756–3788, 2008, ISSN: 1420682X. DOI: 10.1007/s00018-008-8281-1.

[55] G. Charras and A. S. Yap, "Tensile Forces and Mechanotransduction at Cell–Cell Junctions," *Current Biology*, vol. 28, no. 8, R445–R457, 2018, ISSN: 09609822. DOI: 10.1016/j.cub.2018.02.003.

[56] S. Getsios, A. C. Huen, and K. J. Green, "Working out the strength and flexibility of desmosomes," *Nature Reviews Molecular Cell Biology*, vol. 5, no. 4, pp. 271–281, 2004, ISSN: 14710072. DOI: 10.1038/nrm1356.

[57] N. Khalilgharibi, J. Fouchard, N. Asadipour, R. Barrientos, M. Duda, A. Bonfanti, A. Yonis, A. Harris, P. Mosaffa, Y. Fujita, A. Kabla, Y. Mao, B. Baum, J. J. Muñoz, M. Miodownik, and G. Charras, "Stress relaxation in epithelial monolayers is controlled by the actomyosin cortex," *Nature Physics*, vol. 15, no. 8, pp. 839–847, 2019, ISSN: 17452481. DOI: 10.1038/s41567-019-0516-6.

[58] K. Duszyc, V. Viasnoff, *et al.*, "Mechanosensing and mechanotransduction at cell–cell junctions," *Cold Spring Harbor perspectives in biology*, vol. 10, no. 8, a028761, 2018.

[59] Q. Le Duc, Q. Shi, I. Blonk, A. Sonnenberg, N. Wang, D. Leckband, and J. De Rooij, "Vinculin potentiates e-cadherin mechanosensing and is recruited to actin-anchored sites within adherens junctions in a myosin ii–dependent manner," *Journal of Cell Biology*, vol. 189, no. 7, pp. 1107–1115, 2010.

[60] R. Seddiki, G. H. N. S. Narayana, P.-O. Strale, H. E. Balcioglu, G. Peyret, M. Yao, A. P. Le, C. Teck Lim, J. Yan, B. Ladoux, *et al.*, "Force-dependent binding of vinculin to α-catenin regulates cell–cell contact stability and collective cell behavior," *Molecular biology of the cell*, vol. 29, no. 4, pp. 380–388, 2018.

[61] M. Karsdal, *Biochemistry of collagens, laminins and elastin: structure, function and biomarkers*. Academic Press, 2019.

[62] M. A. Schwartz, "Super-resolution microscopy: A new dimension in focal adhesions," *Current Biology*, vol. 21, no. 3, R115–R116, 2011.

[63] C. A. Wilson, M. A. Tsuchida, G. M. Allen, E. L. Barnhart, K. T. Applegate, P. T. Yam, L. Ji, K. Keren, G. Danuser, and J. A. Theriot, "Myosin II contributes to cell-scale actin network treadmilling through network disassembly," *Nature*, vol. 465, no. 7296, pp. 373–377, 2010, ISSN: 14764687. DOI: 10.1038/nature08994.

[64] D. Barfuth, "Zur Regeration der Gewebe.," *Arch. mikr. Anat.*, vol. 37, p. 406, 1891.

[65] E. Uhlenhuth, "Cultivation of the skin epithelium of the adult frog, Rana pipiens," *The Journal of experimental medicine*, vol. 20, no. 6, pp. 614–634, 1914.

[66] P. P. Tam and R. R. Behringer, "Mouse gastrulation: The formation of a mammalian body plan," *Mechanisms of Development*, vol. 68, no. 1-2, pp. 3–25, 1997, ISSN: 09254773. DOI: 10.1016/S0925-4773(97)00123-8.

[67] R. B. Vaughan and J. P. Trinkaus, "Movements of epithelial cell sheets in vitro.," *Journal of Cell Science*, vol. 1, no. 4, pp. 407–413, 1966, ISSN: 00219533.

[68] C. Xu, S. Liu, H. Fu, S. Li, Y. Tie, J. Zhu, R. Xing, Y. Jin, Z. Sun, and X. Zheng, "MicroRNA-193b regulates proliferation, migration and invasion in human hepatocellular carcinoma cells," *European journal of cancer*, vol. 46, no. 15, pp. 2828–2836, 2010.

[69] H. Winstanley, M. Chapwanya, M. McGuinness, and A. C. Fowler, "A polymer–solvent model of biofilm growth," *Proceedings of the Royal Society A: Mathematical, Physical and Engineering Sciences*, vol. 467, no. 2129, pp. 1449–1467, 2011.

[70] C. Fei, S. Mao, J. Yan, R. Alert, H. A. Stone, B. L. Bassler, N. S. Wingreen, and A. Košmrlj, "Nonuniform growth and surface friction determine bacterial biofilm morphology on soft substrates," *Proceedings of the National Academy of Sciences*, vol. 117, no. 14, pp. 7622–7632, 2020.

[71] S. Begnaud, T. Chen, D. Delacour, R. M. Mège, and B. Ladoux, "Mechanics of epithelial tissues during gap closure," *Current Opinion in Cell Biology*, vol. 42, pp. 52–62, 2016, ISSN: 18790410. DOI: 10.1016/j.ceb.2016.04.006.

[72] G. P. Radice, "The spreading of epithelial cells during wound closure in Xenopus larvae," *Developmental Biology*, vol. 76, no. 1, pp. 26–46, 1980, ISSN: 00121606. DOI: 10.1016/0012-1606(80)90360-7.

[73] J. Leighton, Z. Brada, L. W. Estes, and G. Justh, "Secretory activity and oncogenicity of a cell line (mdck) derived from canine kidneyand," *Science*, vol. 163, no. 3866, pp. 472–473, 1969.

[74] J. D. Dukes, P. Whitley, and A. D. Chalmers, "The mdck variety pack: Choosing the right strain," *BMC cell biology*, vol. 12, no. 1, pp. 1–4, 2011.

[75] J. Y. Rho, R. B. Ashman, and C. H. Turner, "Young's modulus of trabecular and cortical bone material: ultrasonic and microtensile measurements," *Journal of biomechanics*, vol. 26, no. 2, pp. 111–119, 1993.

[76] J. P. Marinelli, D. L. Levin, R. Vassallo, R. E. Carter, R. D. Hubmayr, R. L. Ehman, and K. P. McGee, "Quantitative assessment of lung stiffness in patients with interstitial lung disease using MR elastography," *Journal of Magnetic Resonance Imaging*, vol. 46, no. 2, pp. 365–374, 2017, ISSN: 15222586. DOI: 10.1002/jmri.25579.

[77] T. Saxena, J. Gilbert, D. Stelzner, and J. Hasenwinkel, "Mechanical characterization of the injured spinal cord after lateral spinal hemisection injury in the rat," *Journal of Neurotrauma*, vol. 29, no. 9, pp. 1747–1757, 2012, ISSN: 08977151. DOI: 10.1089/neu.2011.1818.

[78] R. J. Oakland, R. M. Hall, R. K. Wilcox, and D. C. Barton, "The biomechanical response of spinal cord tissue to uniaxial loading," *Proceedings of the Institution of Mechanical Engineers, Part H: Journal of Engineering in Medicine*, vol. 220, no. 4, pp. 489–492, 2006, ISSN: 09544119. DOI: 10.1243/09544119JEIM135.

[79] A. R. Harris, L. Peter, J. Bellis, B. Baum, A. J. Kabla, and G. T. Charras, "Characterizing the mechanics of cultured cell monolayers," *Proc. Natl. Acad. Sci. U.S.A.*, vol. 109, no. 41, pp. 16 449–16 454, 2012, ISSN: 00278424. DOI: 10.1073/pnas.1213301109.

[80] J. Ranft, M. Basan, J. Elgeti, J. F. Joanny, J. Prost, and F. Jülicher, "Fluidization of tissues by cell division and apoptosis," *Proc. Natl. Acad. Sci. U.S.A.*, vol. 107, no. 49, pp. 20 863–20 868, 2010, ISSN: 00278424. DOI: 10.1073/pnas.1011086107.

[81] J. R. Mathias, B. J. Perrin, T.-X. Liu, J. Kanki, A. T. Look, and A. Huttenlocher, "Tissue cohesion and the mechanics of cell rearrangement," *Development*, vol. 141, no. 19, pp. 3672–3682, 2014, ISSN: 0741-5400. DOI: https://doi.org/10.1242/dev.104315.

[82] M. L. Manning, R. A. Foty, M. S. Steinberg, and E.-M. Schoetz, "Coaction of intercellular adhesion and cortical tension specifies tissue surface tension," *Proceedings of the National Academy of Sciences*, vol. 107, no. 28, pp. 12 517–12 522, 2010.

[83] C. Blanch-Mercader, R. Vincent, E. Bazellières, X. Serra-Picamal, X. Trepat, and J. Casademunt, "Effective viscosity and dynamics of spreading epithelia: a solvable model," *Soft Matter*, vol. 13, no. 6, pp. 1235–1243, 2017, ISSN: 1744-683X. DOI: 10.1039/C6SM02188C.

[84] S. J. McDonald, P. C. Dooley, A. C. McDonald, J. A. Schuijers, A. R. Ward, and B. L. Grills, "Early fracture callus displays smooth muscle-like viscoelastic properties ex vivo: Implications for fracture healing," *Journal of Orthopaedic Research*, vol. 27, no. 11, pp. 1508–1513, 2009, ISSN: 07360266. DOI: 10.1002/jor.20923.

[85] S. Garcia, E. Hannezo, J. Elgeti, J. F. Joanny, P. Silberzan, and N. S. Gov, "Physics of active jamming during collective cellular motion in a monolayer," *Proceedings of the National Academy of Sciences of the United States of America*, vol. 112, no. 50, pp. 15 314–15 319, 2015, ISSN: 10916490. DOI: 10.1073/pnas.1510973112.

[86] A. Mongera, P. Rowghanian, H. J. Gustafson, E. Shelton, D. A. Kealhofer, E. K. Carn, F. Serwane, A. A. Lucio, J. Giammona, and O. Campàs, "A fluid-to-solid jamming transition underlies vertebrate body axis elongation," *Nature*, vol. 561, no. 7723, pp. 401–405, 2018, ISSN: 14764687. DOI: 10.1038/s41586-018-0479-2.

[87] F. Serwane, A. Mongera, P. Rowghanian, D. A. Kealhofer, A. A. Lucio, Z. M. Hockenbery, and O. Campàs, "In vivo quantification of spatially varying mechanical properties in developing tissues," *Nature Methods*, vol. 14, no. 2, pp. 181–186, 2017, ISSN: 15487105. DOI: 10.1038/nmeth.4101.

[88] J. Zimmermann, B. A. Camley, W. J. Rappel, and H. Levine, "Contact inhibition of locomotion determines cell-cell and cell-Substrate forces in tissues," *Proceedings of the National Academy of Sciences of the United States of America*, vol. 113, no. 10, pp. 2660–2665, 2016, ISSN: 10916490. DOI: 10.1073/pnas.1522330113.

[89] D. Bi, J. H. Lopez, J. M. Schwarz, and M. L. Manning, "A density-independent rigidity transition in biological tissues," *Nature Physics*, vol. 11, no. 12, pp. 1074–1079, 2015, ISSN: 17452481. DOI: 10.1038/nphys3471. arXiv: 1409.0593.

[90] J. A. Park, J. H. Kim, D. Bi, J. A. Mitchel, N. T. Qazvini, K. Tantisira, C. Y. Park, M. McGill, S. H. Kim, B. Gweon, J. Notbohm, R. Steward, S. Burger, S. H. Randell, A. T. Kho, D. T. Tambe, C. Hardin, S. A. Shore, E. Israel, D. A. Weitz, D. J. Tschumperlin, E. P. Henske, S. T. Weiss, M. L. Manning, J. P. Butler, J. M. Drazen, and J. J. Fredberg, "Unjamming and cell shape in the asthmatic airway epithelium," *Nature Materials*, vol. 14, no. 10, pp. 1040–1048, 2015, ISSN: 14764660. DOI: 10.1038/nmat4357.

[91] D. Bi, X. Yang, M. C. Marchetti, and M. L. Manning, "Motility-driven glass and jamming transitions in biological tissues," *Physical Review X*, vol. 6, no. 2, p. 021 011, 2016, ISSN: 21603308. DOI: 10.1103/PhysRevX.6.021011. arXiv: 1509.06578.

[92] D. W. Thompson and Others, "On growth and form.," *On growth and form.*, 1942.

[93] C. H. Turner and F. M. Pavalko, "Mechanotransduction and functional response of the skeleton to physical stress: The mechanisms and mechanics of bone adaptation*," *Journal of Orthopaedic Science*, vol. 3, no. 6, pp. 346–355, 1998, ISSN: 0949-2658. DOI: https://doi.org/10.1007/s007760050064.

[94] G. K. Owens, "Role of mechanical strain in regulation of differentiation of vascular smooth muscle cells," *Circulation research*, vol. 79, no. 5, pp. 1054–1055, 1996.

[95] X. Trepat, L. Deng, S. S. An, D. Navajas, D. J. Tschumperlin, W. T. Gerthoffer, J. P. Butler, and J. J. Fredberg, "Universal physical responses to stretch in the living cell," *Nature*, vol. 447, no. 7144, pp. 592–595, 2007, ISSN: 14764687. DOI: 10.1038/nature05824.

[96] B. W. Benham-Pyle, B. L. Pruitt, and W. J. Nelson, "Mechanical strain induces E-cadherin-dependent Yap1 and β-catenin activation to drive cell cycle entry," *Science*, vol. 348, no. 6238, pp. 1024–1027, 2015, ISSN: 10959203. DOI: 10.1126/science.aaa4559.

[97] K. C. Hart, J. Tan, K. A. Siemers, J. Y. Sim, B. L. Pruitt, W. J. Nelson, and M. Gloerich, "E-cadherin and LGN align epithelial cell divisions with tissue tension independently of cell shape," *Proceedings of the National Academy of Sciences of the United States of America*, vol. 114, no. 29, E5845–E5853, 2017, ISSN: 10916490. DOI: 10.1073/pnas.1701703114.

[98] G. F. Weber, M. A. Bjerke, and D. W. DeSimone, "A Mechanoresponsive Cadherin-Keratin Complex Directs Polarized Protrusive Behavior and Collective Cell Migration," *Developmental Cell*, vol. 22, no. 1, pp. 104–115, 2012, ISSN: 15345807. DOI: 10.1016/j.devcel.2011.10.013.

[99] P. Roca-Cusachs, V. Conte, and X. Trepat, "Quantifying forces in cell biology," *Nature Cell Biology*, vol. 19, no. 7, pp. 742–751, 2017, ISSN: 14764679. DOI: 10.1038/ncb3564.

[100] M. Zhao, T. Pan, G. Zhang, J. Wu, A. Mogilner, Z. Xu, S. Liao, G. Xu, Y. Zhang, F. Lin, W. Losert, Z. Zhu, Y. Sun, and R. M. Lee, "Collective cell migration has distinct directionality and speed dynamics," *Cellular and Molecular Life Sciences*, vol. 74, no. 20, pp. 3841–3850, 2017, ISSN: 1420-682X. DOI: 10.1007/s00018-017-2553-6.

[101] N. L. Nerurkar, C. H. Lee, L. Mahadevan, and C. J. Tabin, "Molecular control of macroscopic forces drives formation of the vertebrate hindgut," *Nature*, vol. 565, no. 7740, pp. 480–484, 2019, ISSN: 14764687. DOI: 10.1038/s41586-018-0865-9.

[102] P. Friedl and D. Gilmour, "Collective cell migration in morphogenesis, regeneration and cancer," *Nature Reviews Molecular Cell Biology*, vol. 10, no. 7, pp. 445–457, 2009, ISSN: 14710072. DOI: 10.1038/nrm2720.

[103] D. E. Discher, P. Janmey, and Y. L. Wang, "Tissue cells feel and respond to the stiffness of their substrate," *Science*, vol. 310, no. 5751, pp. 1139–1143, 2005, ISSN: 00368075. DOI: 10.1126/science.1116995.

[104] T. Yeung, P. C. Georges, L. A. Flanagan, B. Marg, M. Ortiz, M. Funaki, N. Zahir, W. Ming, V. Weaver, and P. A. Janmey, "Effects of substrate stiffness on cell morphology, cytoskeletal structure, and adhesion," *Cell Motility and the Cytoskeleton*, vol. 60, no. 1, pp. 24–34, 2005, ISSN: 08861544. DOI: 10.1002/cm.20041.

[105] K. Ye, X. Wang, L. Cao, S. Li, Z. Li, L. Yu, and J. Ding, "Matrix Stiffness and Nanoscale Spatial Organization of Cell-Adhesive Ligands Direct Stem Cell Fate," *Nano Letters*, vol. 15, no. 7, pp. 4720–4729, 2015, ISSN: 15306992. DOI: 10.1021/acs.nanolett.5b01619.

[106] C. Yang, M. W. Tibbitt, L. Basta, and K. S. Anseth, "Mechanical memory and dosing influence stem cell fate," *Nature Materials*, vol. 13, no. 6, pp. 645–652, 2014, ISSN: 14764660. DOI: 10.1038/nmat3889.

[107] S. Nasrollahi, C. Walter, A. J. Loza, G. V. Schimizzi, G. D. Longmore, and A. Pathak, "Past matrix stiffness primes epithelial cells and regulates their future collective migration through a mechanical memory," *Biomaterials*, vol. 146, pp. 146–155, 2017, ISSN: 18785905. DOI: 10.1016/j.biomaterials.2017.09.012.

[108] V. C. Shukla, N Higuita-Castro, P Nana-Sinkam, and S. N. Ghadiali, "Substrate stiffness modulates lung cancer cell migration but not epithelial to mesenchymal transition," *Journal of Biomedical Materials Research Part A*, vol. 104, no. 5, pp. 1182–1193, 2016.

[109] B. Ladoux and R. M. Mège, "Mechanobiology of collective cell behaviours," *Nature Reviews Molecular Cell Biology*, vol. 18, no. 12, pp. 743–757, 2017, ISSN: 14710080. DOI: 10.1038/nrm.2017.98.

[110] H. Haga, C. Irahara, R. Kobayashi, T. Nakagaki, and K. Kawabata, "Collective movement of epithelial cells on a collagen gel substrate," *Biophysical Journal*, vol. 88, no. 3, pp. 2250–2256, 2005, ISSN: 00063495. DOI: 10.1529/biophysj.104.047654.

[111] L. Petitjean, M. Reffay, E. Grasland-Mongrain, M. Poujade, B. Ladoux, A. Buguin, and P. Silberzan, "Velocity fields in a collectively migrating epithelium," *Biophysical Journal*, vol. 98, no. 9, pp. 1790–1800, 2010, ISSN: 15420086. DOI: 10.1016/j.bpj.2010.01.030.

[112] S. A. Gudipaty, J. Lindblom, P. D. Loftus, M. J. Redd, K. Edes, C. F. Davey, V. Krishnegowda, and J. Rosenblatt, "Mechanical stretch triggers rapid epithelial cell division through Piezo1," *Nature*, vol. 543, no. 7643, pp. 118–121, 2017, ISSN: 14764687. DOI: 10.1038/nature21407.

[113] T. M. Finegan, D. Na, C. Cammarota, A. V. Skeeters, T. J. Nádasi, N. S. Dawney, A. G. Fletcher, P. W. Oakes, and D. T. Bergstralh, " Tissue tension and not interphase cell shape determines cell division orientation in the Drosophila follicular epithelium," *The EMBO Journal*, vol. 38, no. 3, pp. 1–18, 2019, ISSN: 0261-4189. DOI: 10.15252/embj.2018100072.

[114] D. Shook and R. Keller, "Mechanisms, mechanics and function of epithelial-mesenchymal transitions in early development," *Mechanisms of Development*, vol. 120, no. 11, pp. 1351–1383, 2003, ISSN: 09254773. DOI: 10.1016/j.mod.2003.06.005.

[115] A. Jacinto, A. Martinez-Arias, and P. Martin, "Mechanisms of epithelial fusion and repair," *Nature Cell Biology*, vol. 3, no. 5, pp. 117–123, 2001, ISSN: 14657392. DOI: 10.1038/35074643.

[116] S. Wallis, S. Lloyd, I. Wise, G. Ireland, T. P. Fleming, and D. Garrod, "The α isoform of protein kinase C is involved in signaling the response of desmosomes to wounding in cultured epithelial cells," *Molecular Biology of the Cell*, vol. 11, no. 3, pp. 1077–1092, 2000, ISSN: 10591524. DOI: 10.1091/mbc.11.3.1077.

[117] D. L. Nikolić, A. N. Boettiger, D. Bar-Sagi, J. D. Carbeck, and S. Y. Shvartsman, "Role of boundary conditions in an experimental model of epithelial wound healing," *American Journal of Physiology - Cell Physiology*, vol. 291, no. 1, pp. 68–75, 2006, ISSN: 03636143. DOI: 10.1152/ajpcell.00411.2005.

[118] A. Ravasio, I. Cheddadi, T. Chen, T. Pereira, H. T. Ong, C. Bertocchi, A. Brugues, A. Jacinto, A. J. Kabla, Y. Toyama, X. Trepat, N. Gov, L. Neves De Almeida, and B. Ladoux, "Gap geometry dictates epithelial closure efficiency," *Nature Communications*, vol. 6, no. July, p. 7683, 2015, ISSN: 20411723. DOI: 10.1038/ncomms8683.

[119] S. Rausch, T. Das, J. R. Soiné, T. W. Hofmann, C. H. Boehm, U. S. Schwarz, H. Boehm, and J. P. Spatz, "Polarizing cytoskeletal tension to induce leader cell formation during collective cell migration," *Biointerphases*, vol. 8, no. 1, 2013, ISSN: 15594106. DOI: 10.1186/1559-4106-8-32.

[120] N. Yamaguchi, T. Mizutani, K. Kawabata, and H. Haga, "Leader cells regulate collective cell migration via Rac activation in the downstream signaling of integrin β1 and PI3K," *Scientific Reports*, vol. 5, pp. 1–8, 2015, ISSN: 20452322. DOI: 10.1038/srep07656.

[121] V. E. Klepeis, A. Cornell-Bell, and V. Trinkaus-Randall, "Growth factors but not gap junctions play a role in injury-induced Ca2+ waves in epithelial cells," *Journal of Cell Science*, vol. 114, no. 23, pp. 4185–4195, 2001, ISSN: 00219533.

[122] Y. Matsubayashi, M. Ebisuya, S. Honjoh, and E. Nishida, "ERK Activation Propagates in Epithelial Cell Sheets and Regulates Their Migration during Wound Healing," *Current Biology*, vol. 14, no. 8, pp. 731–735, 2004, ISSN: 09609822. DOI: 10.1016/j.cub.2004.03.060.

[123] Y. Matsubayashi, W. Razzell, and P. Martin, "'White wave' analysis of epithelial scratch wound healing reveals how cells mobilise back from the leading edge in a myosin-II-dependent fashion," *Journal of Cell Science*, vol. 124, no. 7, pp. 1017–1021, 2011, ISSN: 00219533. DOI: 10.1242/jcs.080853.

[124] X. Serra-Picamal, V. Conte, R. Vincent, E. Anon, D. T. Tambe, E. Bazellieres, J. P. Butler, J. J. Fredberg, and X. Trepat, "Mechanical waves during tissue expansion," *Nature Physics*, vol. 8, no. 8, pp. 628–634, 2012, ISSN: 1745-2473. DOI: 10.1038/nphys2355.

[125] S. Banerjee, K. J. C. Utuje, and M. C. Marchetti, "Propagating Stress Waves during Epithelial Expansion," *Physical Review Letters*, vol. 114, no. 22, pp. 1–5, 2015, ISSN: 10797114. DOI: 10.1103/PhysRevLett.114.228101. arXiv: 1411.2258.

[126] C. S. Chen, M. Mrksich, S. Huang, G. M. Whitesides, and D. E. Ingber, "Geometric control of cell life and death," *Science*, vol. 276, no. 5317, pp. 1425–1428, 1997, ISSN: 00368075. DOI: 10.1126/science.276.5317.1425.

[127] S. R. K. Vedula, G. Peyret, I. Cheddadi, T. Chen, A. Brugués, H. Hirata, H. Lopez-Menendez, Y. Toyama, L. Neves De Almeida, X. Trepat, C. T. Lim, and B. Ladoux, "Mechanics of epithelial closure over non-adherent environments," *Nature Communications*, vol. 6, pp. 1–10, 2015, ISSN: 20411723. DOI: 10.1038/ncomms7111.

[128] K. Doxzen, S. R. K. Vedula, M. C. Leong, H. Hirata, N. S. Gov, A. J. Kabla, B. Ladoux, and C. T. Lim, "Guidance of collective cell migration by substrate geometry," *Integrative Biology (United Kingdom)*, vol. 5, no. 8, pp. 1026–1035, 2013, ISSN: 17579708. DOI: 10.1039/c3ib40054a.

[129] M. Cetera, G. R. Ramirez-San Juan, P. W. Oakes, L. Lewellyn, M. J. Fairchild, G. Tanentzapf, M. L. Gardel, and S. Horne-Badovinac, "Epithelial rotation promotes the global alignment of contractile actin bundles during Drosophila egg chamber elongation," *Nature Communications*, vol. 5, 2014, ISSN: 20411723. DOI: 10.1038/ncomms6511.

[130] S. L. Haigo and D Bilder, "Global Tissue Revolutions in a Morphogenetic Movement Controlling Elongation," *Science*, no. February, pp. 1071–1074, 2011.

[131] K. Tanner, H. Mori, R. Mroue, A. Bruni-Cardoso, and M. J. Bissell, "Coherent angular motion in the establishment of multicellular architecture of glandular tissues," *Proceedings of the National Academy of Sciences of the United States of America*, vol. 109, no. 6, pp. 1973–1978, 2012, ISSN: 00278424. DOI: 10.1073/pnas.1119578109.

[132] N. S. Rossen, J. M. Tarp, J. Mathiesen, M. H. Jensen, and L. B. Oddershede, "Long-range ordered vorticity patterns in living tissue induced by cell division," *Nature Communications*, vol. 5, no. May, pp. 1–7, 2014, ISSN: 20411723. DOI: 10.1038/ncomms6720.

[133] K. H. Nam, P. Kim, D. K. Wood, S. Kwon, P. P. Provenzano, and D. H. Kim, "Multiscale Cues Drive Collective Cell Migration," *Scientific Reports*, vol. 6, no. July, pp. 1–13, 2016, ISSN: 20452322. DOI: 10.1038/srep29749.

[134] B. Erdogan, M. Ao, L. M. White, A. L. Means, B. M. Brewer, L. Yang, M. K. Washington, C. Shi, O. E. Franco, A. M. Weaver, S. W. Hayward, D. Li, and D. J. Webb, "Cancer-associated fibroblasts promote directional cancer cell migration by aligning fibronectin," *Journal of Cell Biology*, vol. 216, no. 11, pp. 3799–3816, 2017, ISSN: 15408140. DOI: 10.1083/jcb.201704053.

[135] W. Xi, S. Sonam, T. Beng Saw, B. Ladoux, and C. Teck Lim, "Emergent patterns of collective cell migration under tubular confinement," *Nature Communications*, vol. 8, no. 1, 2017, ISSN: 20411723. DOI: 10.1038/s41467-017-01390-x.

[136] H. G. Yevick, G. Duclos, I. Bonnet, and P. Silberzan, "Architecture and migration of an epithelium on a cylindrical wire," *Proceedings of the National Academy of Sciences of the United States of America*, vol. 112, no. 19, pp. 5944–5949, 2015, ISSN: 10916490. DOI: 10.1073/pnas.1418857112.

[137] D. J. Cohen, M. Gloerich, and W. J. Nelson, "Epithelial self-healing is recapitulated by a 3D biomimetic E-cadherin junction," *Proceedings of the National Academy of Sciences of the United States of America*, vol. 113, no. 51, pp. 14 698–14 703, 2016, ISSN: 10916490. DOI: 10.1073/pnas.1612208113.

[138] R. Alert and X. Trepat, "Physical Models of Collective Cell Migration," *Annual Review of Condensed Matter Physics*, vol. 11, no. 1, pp. 77–101, 2020, ISSN: 1947-5454. DOI: 10.1146/annurev-conmatphys-031218-013516. arXiv: 1905.07675.

[139] V. Hakim and P. Silberzan, "Collective cell migration: A physics perspective," *Reports on Progress in Physics*, vol. 80, no. 7, p. 076 601, 2017, ISSN: 00344885. DOI: 10.1088/1361-6633/aa65ef.

[140] M. S. Steinberg, "Differential adhesion in morphogenesis: a modern view," *Current Opinion in Genetics and Development*, vol. 17, no. 4, pp. 281–286, 2007, ISSN: 0959437X. DOI: 10.1016/j.gde.2007.05.002.

[141] C. Dahmann, A. C. Oates, and M. Brand, "Boundary formation and maintenance in tissue development," *Nature Reviews Genetics*, vol. 12, no. 1, pp. 43–55, 2011, ISSN: 14710056. DOI: 10.1038/nrg2902.

[142] M. Deforet, V. Hakim, H. G. Yevick, G. Duclos, and P. Silberzan, "Emergence of collective modes and tri-dimensional structures from epithelial confinement," *Nature Communications*, vol. 5, no. May, p. 3747, 2014, ISSN: 20411723. DOI: 10.1038/ncomms4747.

[143] J. Notbohm, S. Banerjee, K. J. C. Utuje, B. Gweon, H. Jang, Y. Park, J. Shin, J. P. Butler, J. J. Fredberg, and M. C. Marchetti, "Cellular Contraction and Polarization Drive Collective Cellular Motion," *Biophysical Journal*, vol. 110, no. 12, pp. 2729–2738, 2016, ISSN: 15420086. DOI: 10.1016/j.bpj.2016.05.019.

[144] C. Pérez-González, R. Alert, C. Blanch-Mercader, M. Gómez-González, T. Kolodziej, E. Bazellieres, J. Casademunt, and X. Trepat, "Active wetting of epithelial tissues," *Nature Physics*, vol. 15, no. 1, pp. 79–88, 2019, ISSN: 17452481. DOI: 10.1038/s41567-018-0279-5. arXiv: 1902.08871.

[145] G. Peyret, R. Mueller, J. D'Alessandro, S. Begnaud, P. Marcq, R. M. Mège, J. M. Yeomans, A. Doostmohammadi, and B. Ladoux, "Sustained Oscillations of Epithelial Cell Sheets," *Biophysical Journal*, vol. 117, no. 3, pp. 464–478, 2019, ISSN: 15420086. DOI: 10.1016/j.bpj.2019.06.013.

[146] V. Petrolli, M. Le Goff, M. Tadrous, K. Martens, C. Allier, O. Mandula, L. Hervé, S. Henkes, R. Sknepnek, T. Boudou, G. Cappello, and M. Balland, "Confinement-Induced Transition between Wavelike Collective Cell Migration Modes," *Physical Review Letters*, vol. 122, no. 16, p. 168 101, 2019, ISSN: 10797114. DOI: 10.1103/PhysRevLett.122.168101.

[147] T. Lecuit and P. F. Lenne, "Cell surface mechanics and the control of cell shape, tissue patterns and morphogenesis," *Nature Reviews Molecular Cell Biology*, vol. 8, no. 8, pp. 633–644, 2007, ISSN: 14710072. DOI: 10.1038/nrm2222.

[148] M. Reffay, L. Petitjean, S. Coscoy, E. Grasland-Mongrain, F. Amblard, A. Buguin, and P. Silberzan, "Orientation and polarity in collectively migrating cell structures: Statics and dynamics," *Biophysical Journal*, vol. 100, no. 11, pp. 2566–2575, 2011, ISSN: 15420086. DOI: 10.1016/j.bpj.2011.04.047.

[149] K. D. Nnetu, M. Knorr, D. Strehle, M. Zink, and J. A. Käs, "Directed persistent motion maintains sheet integrity during multi-cellular spreading and migration," *Soft Matter*, vol. 8, no. 26, pp. 6913–6921, 2012, ISSN: 1744683X. DOI: 10.1039/c2sm07208d.

[150] H. Jang, J. Notbohm, B. Gweon, Y. Cho, C. Y. Park, S. H. Kee, J. J. Fredberg, J. H. Shin, and Y. Park, "Homogenizing cellular tension by hepatocyte growth factor in expanding epithelial monolayer," *Scientific Reports*, vol. 8, no. April, p. 45 844, 2017, ISSN: 20452322. DOI: 10.1038/srep45844.

[151] D. J. Cohen, W. J. Nelson, and M. M. Maharbiz, "Galvanotactic control of collective cell migration in epithelial monolayers," *Nature Materials*, vol. 13, no. 4, pp. 409–417, 2014, ISSN: 14764660. DOI: 10.1038/nmat3891.

[152] M. A. Huergo, M. A. Pasquale, P. H. González, A. E. Bolzán, and A. J. Arvia, "Dynamics and morphology characteristics of cell colonies with radially spreading growth fronts," *Physical Review E - Statistical, Nonlinear, and Soft Matter Physics*, vol. 84, no. 2, pp. 1–11, 2011, ISSN: 15393755. DOI: 10.1103/PhysRevE.84.021917.

[153] R. M. Lee, D. H. Kelley, K. N. Nordstrom, N. T. Ouellette, and W. Losert, "Quantifying stretching and rearrangement in epithelial sheet migration," *New Journal of Physics*, vol. 15, no. 2, p. 025 036, 2013, ISSN: 13672630. DOI: 10.1088/1367-2630/15/2/025036.

[154] G. Beaune, T. V. Stirbat, N. Khalifat, O. Cochet-Escartin, S. Garcia, V. V. Gurchenkov, M. P. Murrell, S. Dufour, D. Cuvelier, and F. Brochard-Wyart, "How cells flow in the spreading of cellular aggregates," *Proceedings of the National Academy of Sciences of the United States of America*, vol. 111, no. 22, pp. 8055–8060, 2014, ISSN: 10916490. DOI: 10.1073/pnas.1323788111.

[155] M. J. Simpson, K. K. Treloar, B. J. Binder, P. Haridas, K. J. Manton, D. I. Leavesley, D. L. McElwain, and R. E. Baker, "Quantifying the roles of cell motility and cell proliferation in a circular barrier assay," *Journal of the Royal Society Interface*, vol. 10, no. 82, 2013, ISSN: 17425662. DOI: 10.1098/rsif.2013.0007.

[156] J. LaChance and D. J. Cohen, "Practical Fluorescence Reconstruction Microscopy for High-Content Imaging," *bioRxiv*, p. 2020.03.05.979419, 2020. DOI: 10.1101/2020.03.05.979419.

[157] W. Thielicke and E. Stamhuis, "PIVlab–towards user-friendly, affordable and accurate digital particle image velocimetry in MATLAB," *Journal of Open Research Software*, vol. 2, no. 1, e30, 2014. DOI: http://doi.org/10.5334/jors.bl.

[158] R. Eymard, T. Gallouet, and R. Herbin, "Finite Volume Methods," in *Handbook of Numerical Analysis, Volume 7*, 2000, pp. 713–1020.

[159] A. Sakaue-Sawano, H. Kurokawa, T. Morimura, A. Hanyu, H. Hama, H. Osawa, S. Kashiwagi, K. Fukami, T. Miyata, H. Miyoshi, T. Imamura, M. Ogawa, H. Masai, and A. Miyawaki, "Visualizing Spatiotemporal Dynamics of Multicellular Cell-Cycle Progression," *Cell*, vol. 132, no. 3, pp. 487–498, 2008, ISSN: 00928674. DOI: 10.1016/j.cell.2007.12.033.

[160] B. W. Benham-Pyle, J. Y. Sim, K. C. Hart, B. L. Pruitt, and W. J. Nelson, "Increasing β-catenin/Wnt3A activity levels drive mechanical strain-induced cell cycle progression through mitosis," *eLife*, vol. 5, no. OCTOBER2016, pp. 1–28, 2016, ISSN: 2050084X. DOI: 10.7554/eLife.19799.

[161] R. Alert, C. Blanch-Mercader, and J. Casademunt, "Active fingering instability in tissue spreading," *Physical Review Letters*, vol. 122, no. 8, p. 088 104, 2019, ISSN: 10797114. DOI: 10.1103/PhysRevLett.122.088104.

[162] T. E. Angelini, E. Hannezo, X. Trepat, J. J. Fredberg, and D. A. Weitz, "Cell migration driven by cooperative substrate deformation patterns," *Physical Review Letters*, vol. 104, no. 16, p. 168 104, 2010, ISSN: 00319007. DOI: 10.1103/PhysRevLett.104.168104.

[163] K. Aoki, Y. Kondo, H. Naoki, T. Hiratsuka, R. E. Itoh, and M. Matsuda, "Propagating Wave of ERK Activation Orients Collective Cell Migration," *Developmental Cell*, vol. 43, no. 3, 305–317.e5, 2017, ISSN: 18781551. DOI: 10.1016/j.devcel.2017.10.016.

[164] J. Y. Tinevez, N. Perry, J. Schindelin, G. M. Hoopes, G. D. Reynolds, E. Laplantine, S. Y. Bednarek, S. L. Shorte, and K. W. Eliceiri, "TrackMate: An open and extensible platform for single-particle tracking," *Methods*, vol. 115, pp. 80–90, 2017, ISSN: 10959130. DOI: 10.1016/j.ymeth.2016.09.016.

[165] Z. Püspöki, M. Storath, D. Sage, and M. Unser, "Transforms and operators for directional bioimage analysis: a survey," *Focus on Bio-Image Informatics*, pp. 69–93, 2016. DOI: 10.1007/978-3-319-28549-8.

[166] T. Brotto, J.-B. Caussin, E. Lauga, and D. Bartolo, "Hydrodynamics of Confined Active Fluids," *Phys. Rev. Lett.*, vol. 110, no. 3, p. 038 101, 2013. DOI: 10.1103/PhysRevLett.110.038101.

[167] N. Kumar, H. Soni, S. Ramaswamy, and A. K. Sood, "Flocking at a distance in active granular matter," en, *Nat. Commun.*, vol. 5, p. 4688, 2014, ISSN: 2041-1723. DOI: 10.1038/ncomms5688.

[168] D. Oriola, R. Alert, and J. Casademunt, "Fluidization and Active Thinning by Molecular Kinetics in Active Gels," *Phys. Rev. Lett.*, vol. 118, no. 8, p. 088 002, 2017, ISSN: 0031-9007. DOI: 10.1103/PhysRevLett.118.088002.

[169] A. Maitra, P. Srivastava, M. C. Marchetti, S. Ramaswamy, and M. Lenz, "Swimmer Suspensions on Substrates: Anomalous Stability and Long-Range Order," *Phys. Rev. Lett.*, vol. 124, no. 2, p. 028 002, 2020. DOI: 10.1103/PhysRevLett.124.028002.

[170] B. Szabó, G. Szöllösi, B. Gönci, Z. Jurányi, D. Selmeczi, and T. Vicsek, "Phase transition in the collective migration of tissue cells: Experiment and model," *Phys. Rev. E*, vol. 74, no. 6, p. 061 908, 2006, ISSN: 1539-3755. DOI: 10.1103/PhysRevE.74.061908.

[171] S. Henkes, Y. Fily, and M. C. Marchetti, "Active jamming: Self-propelled soft particles at high density," *Phys. Rev. E*, vol. 84, no. 4, p. 040 301, 2011, ISSN: 1539-3755. DOI: 10.1103/PhysRevE.84.040301.

[172] M. Basan, J. Elgeti, E. Hannezo, W.-J. Rappel, and H. Levine, "Alignment of cellular motility forces with tissue flow as a mechanism for efficient wound healing," *Proc. Natl. Acad. Sci. U. S. A.*, vol. 110, no. 7, pp. 2452–2459, 2013, ISSN: 1091-6490. DOI: 10.1073/pnas.1219937110.

[173] C. Malinverno, S. Corallino, F. Giavazzi, M. Bergert, Q. Li, M. Leoni, A. Disanza, E. Frittoli, A. Oldani, E. Martini, T. Lendenmann, G. Deflorian, G. V. Beznoussenko, D. Poulikakos, K. H. Ong, M. Uroz, X. Trepat, D. Parazzoli, P. Maiuri, W. Yu, A. Ferrari, R. Cerbino, and G. Scita, "Endocytic reawakening of motility in jammed epithelia," *Nat. Mater.*, vol. 16, no. April, pp. 587–596, 2017, ISSN: 1476-1122. DOI: 10.1038/nmat4848.

[174] F. Giavazzi, M. Paoluzzi, M. Macchi, D. Bi, G. Scita, M. L. Manning, R. Cerbino, and M. C. Marchetti, "Flocking transitions in confluent tissues," *Soft Matter*, vol. 14, no. 18, pp. 3471–3477, 2018, ISSN: 1744-683X. DOI: 10.1039/C8SM00126J. arXiv: 1706.01113.

[175] W.-J. Rappel, A. Nicol, A. Sarkissian, H. Levine, and W. F. Loomis, "Self-organized Vortex State in Two-Dimensional Dictyostelium Dynamics," *Phys. Rev. Lett.*, vol. 83, no. 6, pp. 1247–1250, 1999. DOI: 10.1103/PhysRevLett.83.1247.

[176] B. A. Camley, Y. Zhang, Y. Zhao, B. Li, E. Ben-Jacob, H. Levine, and W.-J. Rappel, "Polarity mechanisms such as contact inhibition of locomotion regulate persistent rotational motion of mammalian cells on micropatterns," *Proc. Natl. Acad. Sci. U. S. A.*, vol. 111, no. 41, pp. 14 770–14 775, 2014, ISSN: 0027-8424. DOI: 10.1073/pnas.1414498111.

[177] B. Li and S. X. Sun, "Coherent Motions in Confluent Cell Monolayer Sheets," English, *Biophys. J.*, vol. 107, no. 7, pp. 1532–1541, 2014, ISSN: 1542-0086. DOI: 10.1016/j.bpj.2014.08.006.

[178] F. J. Segerer, F. Thüroff, A. Piera Alberola, E. Frey, and J. O. Rädler, "Emergence and Persistence of Collective Cell Migration on Small Circular Micropatterns," *Phys. Rev. Lett.*, vol. 114, no. 22, p. 228 102, 2015, ISSN: 0031-9007. DOI: 10.1103/PhysRevLett.114.228102.

[179] D. L. Barton, S. Henkes, C. J. Weijer, and R. Sknepnek, "Active Vertex Model for cell-resolution description of epithelial tissue mechanics," *PLOS Comput. Biol.*, vol. 13, no. 6, S. Shvartsman, Ed., e1005569, 2017. DOI: 10.1371/journal.pcbi.1005569.

[180] S.-Z. Lin, S. Ye, G.-K. Xu, B. Li, and X.-Q. Feng, "Dynamic Migration Modes of Collective Cells," *Biophys. J.*, vol. 115, no. 9, pp. 1826–1835, 2018, ISSN: 00063495. DOI: 10.1016/j.bpj.2018.09.010.

[181] R. Alert, J.-F. Joanny, and J. Casademunt, "Universal scaling of active nematic turbulence," *Nat. Phys.*, vol. 16, no. 6, pp. 682–688, 2020, ISSN: 1745-2473. DOI: 10.1038/s41567-020-0854-4.

[182] S. K. Schnyder, J. J. Molina, and R. Yamamoto, "Control of cell colony growth by contact inhibition," *Scientific Reports*, p. 6713, 2020. DOI: 10.1038/s41598-020-62913-z. arXiv: 1810.00546.

[183] T. E. Angelini, E. Hannezo, X. Trepat, M. Marquez, J. J. Fredberg, and D. A. Weitz, "Glass-like dynamics of collective cell migration," *Proceedings of the National Academy of Sciences*, vol. 108, no. 12, pp. 4714–4719, 2011, ISSN: 0027-8424. DOI: 10.1073/pnas.1010059108.

[184] B. Monier, A. Pélissier-Monier, A. H. Brand, and B. Sanson, "An actomyosin-based barrier inhibits cell mixing at compartmental boundaries in Drosophila embryos," *Nat. Cell Biol.*, vol. 12, no. 1, pp. 60–65, 2010, ISSN: 14764679. DOI: 10.1038/ncb2005.

[185] E. Batlle and D. G. Wilkinson, "Molecular mechanisms of cell segregation and boundary formation in development and tumorigenesis," *CSH Perspect. Biol.*, vol. 4, no. 1, pp. 1–14, 2012, ISSN: 19430264. DOI: 10.1101/cshperspect.a008227.

[186] K. Anselme, L. Ploux, and A. Ponche, "Cell/material interfaces: Influence of surface chemistry and surface topography on cell adhesion," *J. Adhes. Sci. Technol.*, vol. 24, no. 5, pp. 831–852, 2010, ISSN: 01694243. DOI: 10.1163/016942409X12598231568186.

[187] B. D. Cosgrove, K. L. Mui, T. P. Driscoll, S. R. Caliari, K. D. Mehta, R. K. Assoian, J. A. Burdick, and R. L. Mauck, "N-cadherin adhesive interactions modulate matrix mechanosensing and fate commitment of mesenchymal stem cells," *Nat. Mater.*, vol. 15, no. 12, pp. 1297–1306, 2016, ISSN: 14764660. DOI: 10.1038/nmat4725.

[188] K. Vig, A. Chaudhari, S. Tripathi, S. Dixit, R. Sahu, S. Pillai, V. A. Dennis, and S. R. Singh, "Advances in skin regeneration using tissue engineering," *Int. J. Mol. Sci.*, vol. 18, no. 4, 2017, ISSN: 14220067. DOI: 10.3390/ijms18040789.

[189] H. Takahashi and T. Okano, "Thermally-triggered fabrication of cell sheets for tissue engineering and regenerative medicine," *Adv. Drug Deliv. Rev.*, vol. 138, pp. 276–292, 2019, ISSN: 18728294. DOI: 10.1016/j.addr.2019.01.004.

[190] A. C. Daly, M. D. Davidson, and J. A. Burdick, "3D bioprinting of high cell-density heterogeneous tissue models through spheroid fusion within self-healing hydrogels," *Nat. Commun.*, vol. 12, no. 1, pp. 1–13, 2021, ISSN: 20411723. DOI: 10.1038/s41467-021-21029-2.

[191] N. W. Gale, S. J. Holland, D. M. Valenzuela, A. Flenniken, L. Pan, T. E. Ryan, M. Henkemeyer, K. Strebhardt, H. Hirai, D. G. Wilkinson, T. Pawson, and S. Davis, "Eph Receptors and Ligands Comprise Two Major Specificity Subclasses and Are Reciprocally Compartmentalized during Embryogenesis known family of RTKs with at least 13 distinct members family display dynamic and spatially restricted expres," *Neuron*, vol. 17, pp. 9–19, 1996.

[192] J. W. Astin, J. Batson, S. Kadir, J. Charlet, R. A. Persad, D. Gillatt, J. D. Oxley, and C. D. Nobes, "Competition amongst Eph receptors regulates contact inhibition of locomotion and invasiveness in prostate cancer cells," *Nat. Cell Biol.*, vol. 12, no. 12, pp. 1194–1204, 2010, ISSN: 14657392. DOI: 10.1038/ncb2122.

[193] S. Porazinski, J. de Navascués, Y. Yako, W. Hill, M. R. Jones, R. Maddison, Y. Fujita, and C. Hogan, "EphA2 Drives the Segregation of Ras-Transformed Epithelial Cells from Normal Neighbors," *Curr. Biol.*, vol. 26, no. 23, pp. 3220–3229, 2016, ISSN: 09609822. DOI: 10.1016/j.cub.2016.09.037.

[194] H. B. Taylor, A. Khuong, Z. Wu, Q. Xu, R. Morley, L. Gregory, A. Poliakov, W. R. Taylor, and D. G. Wilkinson, "Cell segregation and border sharpening by Eph receptor-ephrin-mediated heterotypic repulsion," *J. R. Soc. Interface*, vol. 14, no. 132, 2017, ISSN: 17425662. DOI: 10.1098/rsif.2017.0338.

[195] J. Cayuso, Q. Xu, M. Addison, and D. G. Wilkinson, "Actomyosin regulation by eph receptor signaling couples boundary cell formation to border sharpness," *eLife*, vol. 8, e49696, 2019, ISSN: 2050084X. DOI: 10.7554/eLife.49696.

[196] C. Hogan, S. Dupré-Crochet, M. Norman, M. Kajita, C. Zimmermann, A. E. Pelling, E. Piddini, L. A. Baena-López, J. P. Vincent, Y. Itoh, H. Hosoya, F. Pichaud, and Y. Fujita, "Characterization of the interface between normal and transformed epithelial cells," *Nat. Cell Biol.*, vol. 11, no. 4, pp. 460–467, 2009, ISSN: 14657392. DOI: 10.1038/ncb1853.

[197] S. Moitrier, C. Blanch-Mercader, S. Garcia, K. Sliogeryte, T. Martin, J. Camonis, P. Marcq, P. Silberzan, and I. Bonnet, "Collective stresses drive competition between monolayers of normal and Ras-transformed cells," *Soft Matter*, vol. 15, no. 4, pp. 537–545, 2019, ISSN: 17446848. DOI: 10.1039/c8sm01523f.

[198] D. Wright, B. Rajalingam, S. Selvarasah, M. R. Dokmeci, and A. Khademhosseini, "Generation of static and dynamic patterned co-cultures using microfabricated parylene-C stencils," *Lab Chip*, vol. 7, no. 10, pp. 1272–1279, 2007, ISSN: 14730189. DOI: 10.1039/b706081e.

[199] I. Elloumi Hannachi, K. Itoga, Y. Kumashiro, J. Kobayashi, M. Yamato, and T. Okano, "Fabrication of transferable micropatterned-co-cultured cell sheets with microcontact printing," *Biomaterials*, vol. 30, no. 29, pp. 5427–5432, 2009, ISSN: 01429612. DOI: 10.1016/j.biomaterials.2009.06.033.

[200] M. Basan, T. Risler, J.-F. Joanny, X. Sastre-Garau, and J. Prost, "Homeostatic competition drives tumor growth and metastasis nucleation," *HFSP J.*, vol. 3, no. 4, pp. 265–272, 2009, ISSN: 1955-205X. DOI: 10.2976/1.3086732.

[201] J. Ranft, M. Aliee, J. Prost, F. Jülicher, and J. F. Joanny, "Mechanically driven interface propagation in biological tissues," *New J. Phys.*, vol. 16, p. 035 002, 2014, ISSN: 13672630. DOI: 10.1088/1367-2630/16/3/035002.

[202] N. Podewitz, F. Jülicher, G. Gompper, and J. Elgeti, "Interface dynamics of competing tissues," *New J. Phys.*, vol. 18, no. 8, p. 083 020, 2016, ISSN: 13672630. DOI: 10.1088/1367-2630/18/8/083020.

[203] J. J. Williamson and G. Salbreux, "Stability and Roughness of Interfaces in Mechanically Regulated Tissues," *Phys. Rev. Lett.*, vol. 121, no. 23, p. 238 102, 2018, ISSN: 10797114. DOI: 10.1103/PhysRevLett.121.238102.

[204] N. Ganai, T. Büscher, G. Gompper, and J. Elgeti, "Mechanics of tissue competition: Interfaces stabilize coexistence," *New J. Phys.*, vol. 21, p. 063 017, 2019, ISSN: 23318422.

[205] O. Cochet-Escartin, J. Ranft, P. Silberzan, and P. Marcq, "Border forces and friction control epithelial closure dynamics," *Biophys. J.*, vol. 106, no. 1, pp. 65–73, 2014, ISSN: 00063495. DOI: 10.1016/j.bpj.2013.11.015.

[206] P. Recho, J. Ranft, and P. Marcq, "One-dimensional collective migration of a proliferating cell monolayer," *Soft Matter*, vol. 12, no. 8, pp. 2381–2391, 2016, ISSN: 17446848. DOI: 10.1039/c5sm02857d.

[207] R. Vincent, E. Bazellières, C. Pérez-González, M. Uroz, X. Serra-Picamal, and X. Trepat, "Active Tensile Modulus of an Epithelial Monolayer," *Phys. Rev. Lett.*, vol. 115, no. 24, p. 248 103, 2015, ISSN: 10797114. DOI: 10.1103/PhysRevLett.115.248103.

[208] K. Yuki, Y. Yoshida, R. Inagaki, H. Hiai, and M. Noda, "E-cadherin-downregulation and RECK-upregulation are coupled in the non-malignant epithelial cell line MCF10A but not in multiple carcinoma-derived cell lines," *Sci. Rep.*, vol. 4, p. 4568, 2014, ISSN: 20452322. DOI: 10.1038/srep04568.

[209] B. P. Fox and R. P. Kandpal, "Invasiveness of breast carcinoma cells and transcript profile: Eph receptors and ephrin ligands as molecular markers of potential diagnostic and prognostic application," *Biochem. Bioph. Res. Co.*, vol. 318, no. 4, pp. 882–892, 2004, ISSN: 0006291X. DOI: 10.1016/j.bbrc.2004.04.102.

[210] R. A. Foty and M. S. Steinberg, "The differential adhesion hypothesis: A direct evaluation," *Dev. Biol.*, vol. 278, no. 1, pp. 255–263, 2005, ISSN: 00121606. DOI: 10.1016/j.ydbio.2004.11.012.

[211] R. J. Murphy, P. R. Buenzli, R. E. Baker, and M. J. Simpson, "Mechanical Cell Competition in Heterogeneous Epithelial Tissues," *Bull. Math. Biol.*, vol. 82, no. 10, p. 130, 2020, ISSN: 0092-8240. DOI: 10.1007/s11538-020-00807-x.

[212] D. Gradeci, A. Bove, G. Vallardi, A. R. Lowe, S. Banerjee, and G. Charras, "Cell-scale biophysical determinants of cell competition in epithelia," *bioRxiv*, p. 729 731, 2021. DOI: 10.1101/729731.

[213] B. I. Shraiman, "Mechanical feedback as a possible regulator of tissue growth," *Proc. Natl. Acad. Sci. U.S.A.*, vol. 102, no. 9, pp. 3318–23, 2005, ISSN: 0027-8424. DOI: 10.1073/pnas.0404782102.

[214] K. D. Irvine and B. I. Shraiman, "Mechanical control of growth: ideas, facts and challenges," *Development*, vol. 144, no. 23, pp. 4238–4248, 2017, ISSN: 0950-1991. DOI: 10.1242/DEV.151902.

[215] G. T. Eisenhoffer and J. Rosenblatt, "Bringing balance by force: live cell extrusion controls epithelial cell numbers," English, *Trends Cell Biol.*, vol. 23, no. 4, pp. 185–192, 2013, ISSN: 09628924. DOI: 10.1016/j.tcb.2012.11.006.

[216] W. Sun, B. Starly, A. C. Daly, J. A. Burdick, J. Groll, G. Skeldon, W. Shu, Y. Sakai, M. Shinohara, M. Nishikawa, *et al.*, "The bioprinting roadmap," *Biofabrication*, vol. 12, no. 2, p. 022 002, 2020.

[217] W. A. Fischer II, D. J. Weber, and D. A. Wohl, "Personal protective equipment: Protecting health care providers in an ebola outbreak," *Clinical therapeutics*, vol. 37, no. 11, pp. 2402–2410, 2015.

[218] V. Roberts, "To papr or not to papr?" *Canadian journal of respiratory therapy: CJRT= Revue canadienne de la therapie respiratoire: RCTR*, vol. 50, no. 3, p. 87, 2014.

[219] A. Licina, A. Silvers, and R. L. Stuart, "Use of powered air-purifying respirator (papr) by healthcare workers for preventing highly infectious viral diseases—a systematic review of evidence," *Systematic reviews*, vol. 9, no. 1, pp. 1–13, 2020.